Theoretical analysis of injection-driven bubble pinch-off in capillary flows

Megan Kate Richards

EPSRC Centre for Doctoral Training in Future Fluid Dynamics

University of Leeds

Submitted in accordance with the requirements for the degree of

Doctor of Philosophy

November 2025

Declaration of Authorship

I confirm that the work submitted is my own, except where work which has formed part of jointly authored publications has been included. My contribution and the other authors to this work has been explicitly indicated below. I confirm that appropriate credit has been given within the thesis where reference has been made to the work of others.

Chapter 3 contains work from jointly authored 'Theory of Taylor bubble pinch-off in planar coflow'. Authors: Megan K. Richards and Dr. Samuel S. Pegler. Journal of Fluid Mechanics, submitted.

Development of the mathematical models, asymptotic theories and numerical solvers is attributable to Megan K. Richards. The research was supervised by Dr. Samuel S. Pegler, who provided guidance on research directions and methodologies, and assisted with manuscript revision.

Acknowledgements

This thesis marks the culmination of three years of learning, growth, and hard work - a journey that would not have been possible without the help and guidance of many people. Firstly, I would like to thank my supervisor Sam Pegler for his continuous support and unwavering enthusiasm throughout this process. I am extremely grateful for all your advice and direction.

I would also like to thank the Centre for Doctoral Training in Future Fluid Dynamics for providing me with a support network, and the Engineering and Physical Sciences Research Council (EPSRC) for funding my research.

On a personal note, I would like to thank my family for their endless encouragement. To my parents - I am forever grateful for your ongoing support, unconditional love, and limitless belief in me. Finally, to my partner Dan, thank you for keeping things in perspective and for being my perpetual rubber duck.

Abstract

A key challenge in the development of microfluidic devices is the control of the size and frequency of bubble formation. In a coflow geometry, the continuous phase flows through the channel and the gas phase is injected in parallel to the direction of the flow. Injection of both the gas and liquid phases at low flow rates results in bubbles that almost entirely fill the channel, with only a thin liquid film separating the bubble from the wall. These elongated (Taylor) bubbles have a large gas-liquid surface area which can increase the efficiency of chemical reactors involving heat or mass transfer.

The bubble formation process in the Taylor flow regime is controlled by the dynamics in the vicinity of the input channel, where the outer fluid squeezes the gaseous thread to produce a thinning neck. In this work, we give the first theoretical explanation of experimentally observed scaling laws for bubble length in microfluidic devices. We begin with an asymptotic analysis of Taylor bubble pinch-off in a planar geometry based on lubrication approximations, and explore the oscillatory pinch-off dynamics associated with the production of Taylor bubbles at a regular frequency. Numerical solutions are presented over a range of flow conditions, demonstrating an assortment of bubble characteristics, and compared to existing results where possible. We then progress to the analysis of Taylor bubble pinch-off in an axisymmetric capillary, which differs fundamentally from the planar analogue due to azimuthal curvature contributions. From our mathematical analysis, we provide the first theoretical explanation for the well-established experimentally observed scaling law, which states that the key control of bubble pinch off time t_* is the input flux of the liquid phase q_c as $t_* \sim 1/q_c$.

Contents

List of Figures

Chapter 1

Introduction

Microfluidic devices are designed to bring together two or more immiscible fluid streams in such a way as to generate droplets and bubbles of very small diameters (Anna, 2016). Microbubbles, typically defined as gas-filled bubbles which have diameters in the range 0.5-10 μm, have been recognised as an area of potential for the development of cancer treatment methods (Sirsi & Borden, 2009). Microfluidic "lab-on-a-chip" devices show a promising capacity to revolutionise the field by providing a new and improved method for microbubble production. In particular, microfluidics gives greater control over the size and frequency of bubbles produced, meaning the bubbles are quickly becoming a viable option for targeted drug delivery (Vladisavljević *et al.*, 2013).

There are two main methods for bubble formation in microfluidic devices: active and passive. In the active method, external forces are used to manipulate the droplet formation, for example by application of a magnetic or an electric field. For the passive approach, bubbles are formed when the gaseous phase is introduced into a flowing, immiscible fluid. Syringe pumps are used to supply the fluids at a constant flow rate. The flow parameters and the geometry of the device control the characteristics of the bubbles produced. There are three categories of microfluidic geometries: coflow geometries in which the two phases are injected in parallel, cross-flow geometries (e.g. the T-junction) in which the two phases meet at an angle, and flow-focusing configurations in which there is a geometric constriction that accelerates the fluids and causes the inner thread to narrow (Anna, 2016). Figure 1.1 shows an example schematic of each configuration.

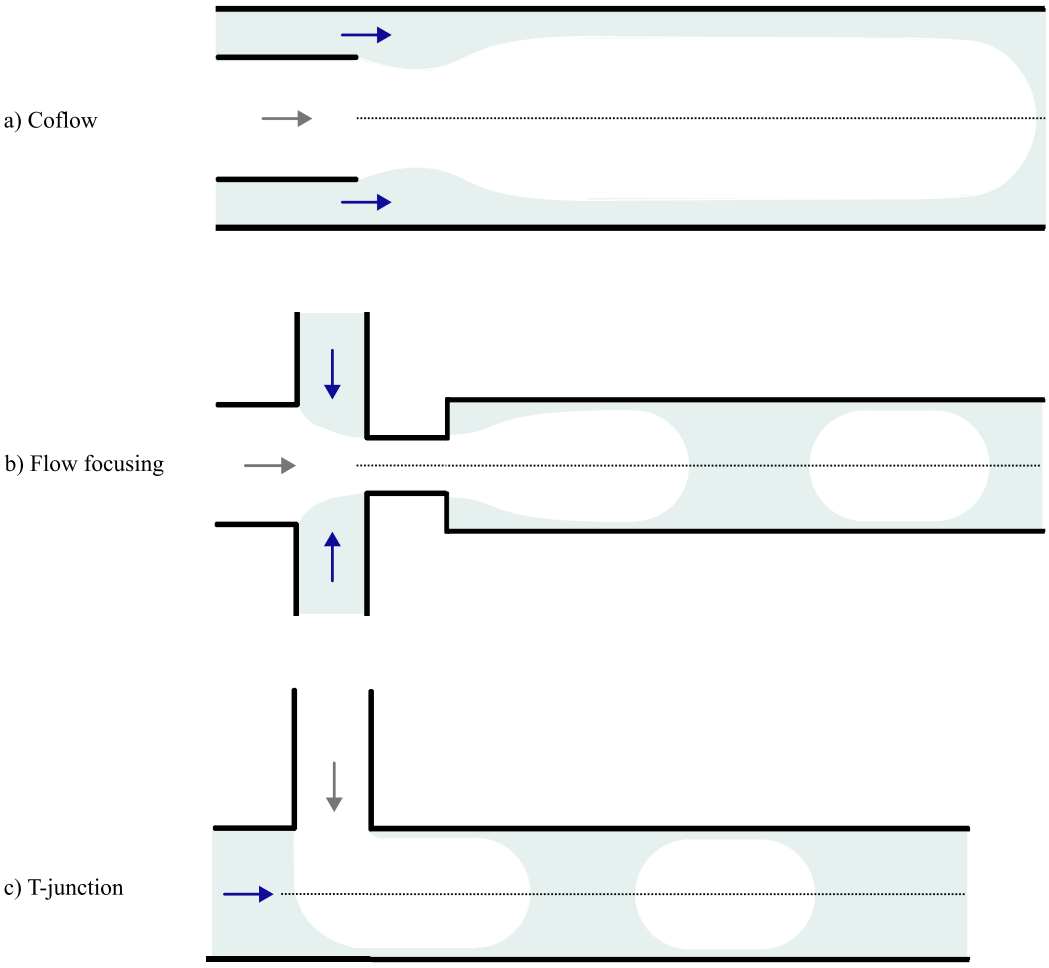

Figure 1.1: A schematic to show the three main categories of microfluidic device geometry: a) coflow, b) flow focusing and c) cross flow, e.g. T-junction. The arrows represent the direction of the flow for the dispersed phase (white) and the continuous phase (blue).

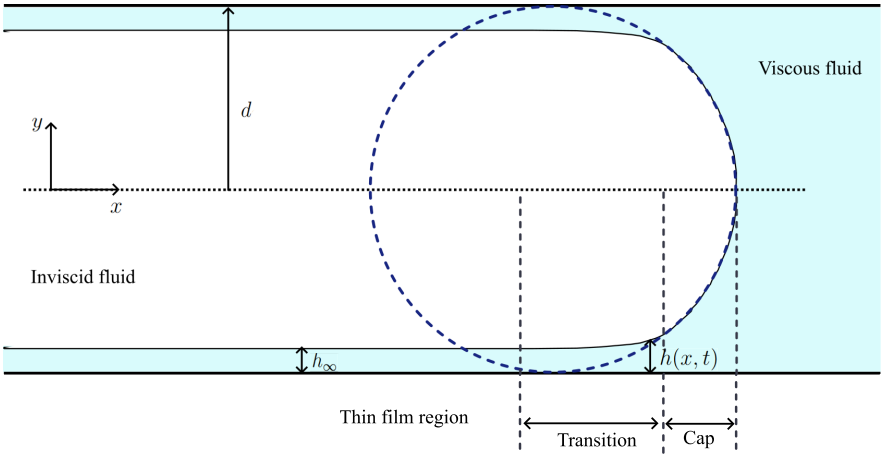

Figure 1.2: A schematic of the semi-infinite bubble formed by injection of gaseous fluid into a planar channel of width $2d$ filled with viscous fluid. In the thin film region, the bubble is surrounded by a film of uniform thickness h_∞. The lubrication approximation holds in the transition region that connects the thin film region to the spherical cap, since the film height $h(x,t)$ is much smaller than the channel ($h \ll d$).

At the small scale associated with microfluidic devices, gravity is negligible and the flow behaviour is governed by surface tension and interfacial phenomena. Two-phase capillary flows are fundamental to understanding the bubble formation process and have been the subject of many fundamental papers. In particular, it is common to consider a finger of inviscid fluid being forced through a circular tube filled with a different fluid of dynamic viscosity μ, resulting in a semi-infinite bubble propagating at a steady speed U (e.g. Bretherton, 1961; Cox, 1962; Reinelt & Saffman, 1985; Taylor, 1961). As the bubble passes through the tube, a thin film of viscous fluid of thickness h_∞ is deposited on the interior of the tube, as shown in figure 1.2. The fundamental parameter of the system is the capillary number, defined as $C = \mu U/\gamma$ where γ is the interfacial coefficient of surface tension, which is a dimensionless number representing the ratio of viscous forces to surface tension. The experiments of Fairbrother & Stubbs (1935) and Taylor (1961) began the study of gas-liquid displacement in capillary tubes. Both works obtained experimental measurements for the amount of viscous fluid left on the walls of a tube as a long air bubble is blown through. Fairbrother & Stubbs (1935)

obtain an empirical relationship for the amount of fluid left lining the tube wall in terms of capillary number, valid only for small capillary numbers $C \lessapprox 0.014$. They suggested that the film thickness is proportional to $C^{1/2}$, and this empirical relationship was confirmed by the experiments of Taylor (1961) for fluids of high viscosity up to $C \approx 0.1$.

The work of Bretherton (1961) provides a theoretical study on the steady motion of a long bubble under pressure-driven flow in a circular tube of radius d. Bretherton considers the movement of an inviscid bubble at low speeds, and assumes a constant interfacial tension. In this small-capillary number limit, viscous forces dominate and inertial forces are negligible such that the steadily moving interface between the bubble and the incompressible fluid that fills the channel is described by the Stokes equations. The bubble has a static shape represented by a near-spherical meniscus at its front joined to a long section of uniform thickness through a region in which lubrication theory is applied. Bretherton matches the curvature in the uniform film region to the curvature of the spherical cap to derive an expression for the thickness of the thin fluid film h_∞ that surrounds the bubble as

$$\frac{h_\infty}{d} = 1.3375\, C^{2/3}. \tag{1.1}$$

This prediction does not agree with the formula derived empirically by Fairbrother & Stubbs (1935), but many subsequent experimental investigations into the thickness of the thin film surrounding an elongated bubble have confirmed the Bretherton scaling in the small capillary number limit (e.g. Ratulowski & Chang, 1989; Reinelt & Saffman, 1985; Taylor, 1961). The Bretherton scaling is both asymptotically self-consistent in its region of validity (small capillary numbers), and has been confirmed by numerous experimental papers; for these reasons, the Bretherton scaling is widely accepted in place of the outdated empirical scaling $C^{1/2}$ predicted by Fairbrother & Stubbs (1935).

To build upon the propagation of a semi-infinite air finger and move closer to an understanding of bubble pinch-off, we can introduce injection of the continuous phase as well as the dispersed phase. In this thesis, we will consider a coflow geometry, where both the inner gaseous phase and the outer viscous fluid are injected in a concentric alignment, which creates injection-driven pinch-off

of monodisperse bubbles at regular intervals. The size of the bubbles produced depends on the flow parameters and geometry of the system. Elongated bubbles with a capsular shape are formed at small capillary numbers in the squeezing regime. The regime is governed by the confined breakup mechanism whereby the gaseous thread grows to fill the channel and obstruct the liquid phase. Consequently, the increased pressure in the upstream liquid phase causes the liquid to squeeze the gaseous thread until it breaks (Garstecki *et al.*, 2005; van Steijn *et al.*, 2009). The bubbles formed in the squeezing regime, which are much wider than the channel diameter such that they almost entirely fill the channel with at most a thin liquid film separating the bubble and the channel wall, are known as Taylor bubbles. Taylor bubbles are characterised by an approximately hemispherical front connected to a cylindrical region of uniform thickness that is several times longer than the bubble diameter. The shape of the rear of the bubble is determined by the flow conditions, fluid properties and geometric constraints of the tube. The formation is governed by a localised necking process: the bulk liquid away from the interface remains comparatively quiescent whereas the necking region exhibits strong extensional flow and rapid curvature variation that ultimately determines the characteristics of the resultant bubble. The size of the bubble is determined by the flow parameters and the geometric confinement of the channel (which suppresses radial breakup). The capillary number regulates the stability of the necking region and the thickness of the surrounding liquid film, with low to moderate values favouring the formation of Taylor bubbles. The gas-to-liquid flux ratio controls whether the gas supply is sufficient to sustain an elongated structure. If the gas flux is too small compared to the liquid flux, the neck thins rapidly such that smaller, non-Taylor bubbles are formed.

The configuration examined by Bretherton (1961) considers a semi-infinite Taylor bubble. Taylor flow is present across a wide range of parameter settings in microchannels, making it a very common two-phase flow pattern, and offers the advantage of a large gas-liquid contact area which is beneficial in industrial processes such as the capture of carbon dioxide (Sun *et al.*, 2025; Zhang *et al.*, 2022). The smaller bubbles required for use as drug delivery vehicles are generated at higher capillary numbers. These small bubbles are formed in a dripping regime that is characterised by the detachment of the bubble at the injection nozzle in

a periodic manner. The gaseous thread narrows until the viscous forces of the outer fluid exceed the surface tension force that holds the bubble at the nozzle, resulting in bubble detachment.

Due to the complex geometry of microfluidic devices, most of the existing literature is based on experimental observations (e.g Cubaud *et al.*, 2005; Garstecki *et al.*, 2005; Salman *et al.*, 2006; van Steijn *et al.*, 2007; Xiong *et al.*, 2007). Cubaud *et al.* (2005) studied a flow-focusing configuration consisting of square microchannels joined perpendicularly to each other. From experimental observations, it was suggested that the bubble length is proportional to the ratio of the volumetric gas and liquid flow rates. Garstecki *et al.* (2005) studied the breakup of an inviscid fluid at low capillary numbers in a flow-focusing configuration. They suggested that the neck of the gaseous thread evolves as a series of quasi-static equilibria of minimal surface energy and that the collapsing rate of the neck is proportional to the flow rate of the liquid phase q_c. The linear decrease of the radius with time was confirmed by the experiments of van Steijn *et al.* (2007, 2009), where a micro-Particle Image Velocimetry (μ-PIV) system was used to measure the flow field in the continuous phase during bubble formation. At a point in time defined by the configuration of the system, the narrowing neck of the thread starts to collapse rapidly (Garstecki *et al.*, 2006). The process occurs so quickly that this final stage of collapse has a negligible contribution to the size of the bubble. To date, the experimentally observed scaling laws are unexplained theoretically and present a salient open research problem.

In this work, we study the formation of bubbles under coflow configuration in both a planar two-dimensional channel, and in an axisymmetric capillary tube of circular cross-section. The fundamental differences in pinch-off phenomena for axisymmetric and planar geometries can be attributed to the differences in interfacial curvature which inherently affect the capillary pressure that drives pinch-off through the Young-Laplace equation. In an axisymmetric tube of radius R described by a cylindrical coordinate system (r, θ, z), the interface possesses both axial and azimuthal curvature contributions

$$\kappa = \underbrace{\frac{h_{zz}}{(1+h_z^2)^{3/2}}}_{\text{axial}} + \underbrace{\frac{1}{(R-h)(1+h_z^2)^{1/2}}}_{\text{azimuthal}},$$

whereas the curvature expression in the planar geometry, considered in a two-dimensional (x, y) Cartesian coordinate system, includes only the axial term

$$\kappa = \frac{h_{xx}}{(1 + h_x^2)^{3/2}}. \tag{1.2}$$

This thesis provides three primary contributions to understanding bubble pinch-off in a coflow configuration. We begin by formulating a simple lubrication framework with downstream matching to a Taylor bubble to capture the dynamics of the fluid-fluid interface as a Taylor bubble is generated in a planar coflow geometry. Under the assumption of slowly varying interface $|h_x| \ll 1$, the lubrication approximation simplifies the Stokes flow model

$$\mu u_{yy} = p_x, \qquad p_y = 0, \tag{1.3}$$

and reduces the curvature expression

$$\kappa = \frac{h_{xx}}{(1 + h_x^2)} \approx h_{xx} \left(1 - \frac{3}{2} h_x^2 + \dots\right), \tag{1.4}$$

resulting in the linearised leading order approximation $\kappa \approx h_{xx}$. The evolution of the bubble neck forms a quasi-static asymptotic state, which we resolve with use of an asymptotic matching to an inner region near the front of the parabola, similarly to classical theories describing the capillary-driven spread of a droplet over a horizontal substrate. This modelling approach results in a novel analytical prediction for bubble pinch-off times in the planar coflow geometry.

However, the model presented is limited to the formation of a singular bubble and cannot capture periodic bubble formation. Hence, we progress to a more generalised time-dependent lubrication framework to capture the entire bubble interface beyond the necking zone. By retaining the exact nonlinear expression for the curvature (1.2), we are able to model larger interfacial gradients and can consequently generate periodic bubble trains at regular intervals.

To conclude, we expand our mathematical analysis of Taylor bubble pinch-off to an axisymmetric configuration. We find that the additional azimuthal contributions to curvature result in quasi-static solution shapes that are consequently more complex and can no longer be described entirely by parabolic solutions. In contrast to the planar geometry, the solution states evolve towards a point

at which quasi-static solutions no longer exist. We explore the breakdown of quasi-static solutions and the relationship to bubble pinch-off by conducting a full regime analysis for the quasi-static solution states which culminates in the first theoretical explanation of the experimentally observed scaling law for bubble pinch-off time $t_* \sim 1/q_c$.

Chapter 2

Background

2.1 Two-phase capillary flows

Consider the concurrent injection of two immiscible fluids in parallel with one another, creating a two-fluid system. The fluids are introduced through microchannels or cylindrical capillary tubes that are arranged concentrically. A continuous (liquid) phase flows through the outer channel/tube, and a dispersed (gaseous) phase is introduced through an inner channel/tube. The problem of fluid displacement within a confined geometry upon injection of another fluid has been subjected to a great deal of study. The two-phase flow patterns exhibited by multiphase gas-liquid flows are characterised by the way in which the phases are arranged within the confining geometry (Triplett *et al.*, 1999). The flow patterns of gas-liquid flow in microchannels can be generally divided into Taylor flow (characterised by elongated bubbles), bubbly flow (distinct, non-spherical bubbles that are small compared to the channel radius), annular flow (indicated by a liquid film that lines the channel walls) and churn flow (chaotic, irregular bubbles). The particular flow pattern depends on the shape of the channel or pipe, as well as fluid properties and geometrical and fluid mechanical parameters. The regimes are often classified based on non-dimensional parameters of the system; exploration over variables such as gas and liquid velocities allows for the construction of flow maps that divide the parameter space into regions based on the observed fluid flow regimes. It is difficult to construct the phase

boundaries exactly, and each map is limited to a particular geometry and range of flow parameters (Colombo & Fairweather, 2025).

If only the inner fluid is injected, a semi-infinite finger is formed that propagates through the tube at a constant speed and deposits a fluid film on the interior of the tube (figure 1.2). Upstream of the bubble front, there is a region over which the bubble, and therefore the surrounding film, has uniform thickness. The film thickness was first measured in the experiments of Fairbrother & Stubbs (1935). The investigation was limited to small capillary numbers, and was later extended by the experiments of Taylor (1961) to $C \approx 0.1$. Bretherton (1961) built upon these experimental investigations by theoretically deriving a relationship between film thickness and capillary number that is accurate to within 5% error if $C < 0.003$. His approach will be discussed in detail in section 2.1.2.

If both fluids are injected then the inner fluid can pinch-off, resulting in the formation of finite bubbles, the size of which is controlled by the flow parameters of the system. When the flux of the gas phase is sufficiently large compared with the flux of the liquid, elongated capsular bubbles are formed which are surrounded by a very thin film that coats the interior of the tube, similar to as in the semi-infinite bubble configuration. This flow pattern is referred to as the Taylor bubble regime and is the most common flow pattern observed in multiphase microreactors, persisting over a wide range of operating conditions (Chen *et al.*, 2009; Salman *et al.*, 2006; Triplett *et al.*, 1999). The elongated bubbles possess favourable characteristics such as stable flow patterns and large surface to volume ratios for more efficient heat transfer, making the production mechanisms of Taylor bubbles an important area of research (e.g. Asadolahi *et al.*, 2012; Sattari-Najafabadi *et al.*, 2018; Shen *et al.*, 2024).

2.1.1 Experiments on gas fingers

The experiments of Fairbrother & Stubbs (1935), Taylor (1961) and Cox (1962) began the study of gas-liquid displacement in capillary tubes by providing measurements for the viscous fluid left on the walls as a gas bubble passes through. They considered the injection of air into one end of a tube containing a viscous

fluid, which causes a bubble to form, surrounded by a fraction of mass of liquid left as a film along the channel wall. A common focus of all three papers was to find empirical relationships for the uniform thickness of the fluid film left lining the tube, h_∞. Fairbrother & Stubbs (1935) provided the first empirical relationship for the dimensionless film thickness $B \equiv h_\infty/r$ as

$$B = 0.5\, C^{1/2}, \qquad (C < 0.0014), \tag{2.1}$$

for bubbles with length larger than three times the radius r of the capillary. Taylor (1961) extended the results to larger capillary numbers by considering more viscous fluids, verifying (2.1) as a good approximation for $C \lessapprox 0.1$. As capillary number was increased beyond this range, Taylor concluded that (2.1) overestimates the value of B and noted instead that the value of B tends to an asymptotic value around 0.44. This number was later refined by Cox (1962) to 0.40.

2.1.2 Modelling of thin films

Of the most notable papers on the steady motion of elongated bubble in a tube is that of Bretherton (1961), which derives a theoretical model to describe the steady motion of an inviscid fluid under pressure-driven flow through a circular tube filled with viscous fluid. Bretherton used the Stokes equations with surface tension to describe the steadily moving interface between the bubble and the incompressible fluid of viscosity μ which fills the channel. It is assumed that the interfacial tension γ is constant, and the radius of the capillary tube is small enough such that gravitational effects are negligible.

Since the bubble is long, its static shape can be represented by spherical menisci at its front and rear, joined by a region of some constant radius at a large enough distance from the bubble tip (figure 1.2). The long region of constant film thickness h_∞ is connected to the spherical cap by a 'transition region'. Since the thickness of this film is much smaller than the length of the bubble, Bretherton applies the lubrication approximation with a linearised curvature here.

The lubrication approach used by Bretherton applies to flows in fluids separated by almost parallel boundaries, where the distance between these boundaries

is much smaller than a typical length scale of the flow. As an example, consider a flow with horizontal speed U along a flat plate at $y = 0$. We assume the height of the fluid $y = h(x, t)$ is small such that $h \ll L$, where L is a typical horizontal length scale of the flow. As a result, the pressure in the direction normal to the wall is constant to leading order and the horizontal force balance is dominated by shear stresses such that the Stokes equations are simplified to the two equations

$$\frac{\partial p}{\partial x} = \mu \frac{\partial^2 u}{\partial y^2}, \qquad \frac{\partial p}{\partial y} = 0. \tag{2.2}$$

The second equation implies that pressure is a function of the axial coordinate x only, and is therefore uniform across the film thickness.

In reviewing here the same geometry as Bretherton (1961) (figure 1.2), we apply the no-slip boundary condition on the channel wall $y = d$ and the condition of zero tangential stress at the bubble interface $y = d - h(x, t)$ given by

$$u(x, d, t) = 0, \qquad \text{and} \qquad u_y(x, d - h, t) = 0, \tag{2.3a-b}$$

respectively. Integrating the first equation in (2.2) twice, we obtain

$$u = \frac{1}{2\mu} \frac{\partial p}{\partial x} (y - d)\,(y - d + 2h)\,. \tag{2.4}$$

The relationship between the pressure p, the surface tension γ and the bubble thickness is described by the Young-Laplace equation as

$$p = -\gamma \kappa, \tag{2.5}$$

where κ is the interfacial curvature, and γ the coefficient of surface tension. In the transition region, where the gradient of the interface is sufficiently small for the lubrication theory to hold, curvature can be approximated to leading order as $\kappa \approx h_{xx}$. We can evaluate the volume flux (per unit width) of the flow using (2.4) as

$$q(x, t) = \int_{d-h(x,t)}^{d} u \, \mathrm{d}y = \frac{\gamma}{3\mu} h^3 h_{xxx}. \tag{2.6}$$

Substituting the expression for flux (2.6) into the continuity equation of the fluid film, $h_t = -q_x$, we obtain the governing nonlinear hyperdiffusion equation

$$h_t = \frac{\gamma}{3\mu} \left(h^3 h_{xxx}\right)_x. \tag{2.7}$$

This classical equation, often known as the capillary-driven thin film equation, governs the deposition of a thin film along a solid (e.g. Bretherton, 1961; Hammond, 1983; Oron *et al.*, 1997).

Since the front of the bubble is assumed to advance at a constant speed U, we can move into the frame of the bubble and search for a travelling-wave solution of the form $h(x,t) = h(x-Ut)$. Seeking a steady state in the moving frame, (2.7) yields the travelling-wave equation

$$Uh_x = \frac{\gamma}{3\mu}\left(h^3 h_{xxx}\right)_x. \tag{2.8}$$

Far upstream of the nose, the film is assumed to approach a constant value

$$\lim_{x\to-\infty} h = h_\infty, \tag{2.9}$$

where h_∞ is the as-yet-undetermined *interior thickness* of the fluid film surrounding the bubble. Hence, integrating (2.8) once, we obtain an expression for the interface profile in the transition region as

$$U(h-h_\infty) = \frac{\gamma}{3\mu} h_{xxx} h^3, \tag{2.10}$$

where the integration constant is determined by (2.9). The expression for the interface (2.10) is a third-order ordinary differential equation (ODE) dependent on the film thickness $h(x,t)$ only. By introducing the scalings

$$h = h_\infty \eta, \qquad x = h_\infty (3C)^{-1/3}\xi, \tag{2.11}$$

to (2.10), where $C = \mu U/\gamma$ is a capillary number, Bretherton arrives at the Landau-Levich equation for the liquid film in the transition region

$$\frac{\partial^3 \eta}{\partial \xi^3} = \frac{\eta - 1}{\eta^3}. \tag{2.12}$$

This expression was first derived to describe the thickness of a thin film left on a plate as it is withdrawn from a liquid (Landau & Levich, 1988).

Whilst the Landau-Levich equation does not have an analytical solution, it satisfies the uniform asymptotic solution $\eta \to 1$ for $\xi \to -\infty$, corresponding to the dimensional solution $h = h_\infty$ in the region of constant film thickness. To find

the solution in the transition region, Bretherton considered the region closer to the thin film ($\eta \to 1$) separately to the region closer to the bubble front ($\eta \gg 1$). The equation (2.12) can be integrated numerically, starting at the asymptotic condition $\eta(-\infty) = 1$. The uniform film region must be matched smoothly to the circular cap of the bubble through a transition region. In the transition zone, the circular front appears parabolic to leading order when viewed at the lubrication scale

$$\eta = \tfrac{1}{2}P\xi^2 + Q\xi + R, \tag{2.13}$$

where P, Q and R are a set of constants defining a unique solution subject to the specified origin, and $P = 0.643$. The position of the origin of ξ is physically irrelevant since a change of origin corresponds to an equivalent bubble shape under a horizontal translation. Therefore, Bretherton chose to find a solution with vanishing Q coefficient.

In dimensional coordinates, the parabola (2.13) corresponds to

$$h = \tfrac{1}{2}P(3C)^{2/3}\left(\frac{x^2}{h_\infty}\right) + R/h_\infty, \tag{2.14}$$

which forms a leading order approximation of a circle of radius $h_\infty/(P(3C)^{2/3})$. Hence, Bretherton matched the curvature in the parabolic region

$$h_{xx} = (3C)^{2/3}\left(\frac{P}{h_\infty}\right) + \frac{1}{d}. \tag{2.15}$$

to the (approximately) circular bubble front $2/d$, to obtain the following expression for the thin film thickness h_∞

$$\frac{h_\infty}{d} = (3C)^{2/3}P \approx 1.3375\, C^{2/3}. \tag{2.16}$$

The Bretherton expression for film thickness (2.16) is valid for the small capillary number limit, $C < 0.003$.

Reinelt & Saffman (1985) studied the penetration of an air finger into a two-dimensional channel and a circular tube filled with viscous fluid. Numerical solutions to the Stokes equations, found using finite difference methods and plotted in figure 2.1, exhibit excellent agreement with the experiments of Taylor (1961) in the axisymmetric configuration. The asymptotic analysis performed by Bretherton gives a good approximation for the film thickness in the low capillary number

limit (accurate to within 5% for values of C up to 0.003). The scaling analysis used by Aussillous & Quéré (2000) aimed to identify the role of different parameters in the amount of viscous liquid left on the wall of a channel as air is blown through. This work extended the results of Taylor (1961) by considering wetting liquids of lower viscosity displaced by higher velocities of gas. The new experimental data exhibited good agreement with the experiments of Taylor for $C \leq 2$, and the following empirical form of the deposition scaling law was found to approximately describe the data:

$$B(C) = \frac{P(3C)^{2/3}}{1 + PQ(3C)^{2/3}}, \tag{2.17}$$

where the coefficient P was derived by Bretherton, and the coefficient $Q = 2.5$ is empirical.

More recently, works by Klaseboer *et al.* (2014) and Cherukumudi *et al.* (2015) have made attempts to solidify a theoretical extension of the Bretherton model to larger capillary numbers. The approach of Klaseboer *et al.* (2014) follows that of Bretherton, distinguishing between the flat film and transition regions to analytically obtain a value for the film thickness around the bubble. However, it differs in that the analysis is done in terms of pressure buildup in the transition region under the added constraint that the bubble and film combined must fit inside the tube (not used by Bretherton). Under these modifications, an expression for film thickness is derived that is very similar to the "empirical model" of Aussillous & Quéré (2000). Cherukumudi *et al.* (2015) derived analytical expressions for the pressure jump at the front and back of a finite Taylor bubble, allowing for the calculation of the total pressure drop due to the presence of the bubble. Furthermore, a boundary value approach is used to find the bubble shape with boundary conditions specified by the vanishing thickness of the bubble at its front and rear. This method allows for the shape of both the front and rear of the bubble to be solved simultaneously, rather than integrating in one direction at a time as in Bretherton (1961), as long as the bubble is of a sufficient length to ensure the front and back are independent.

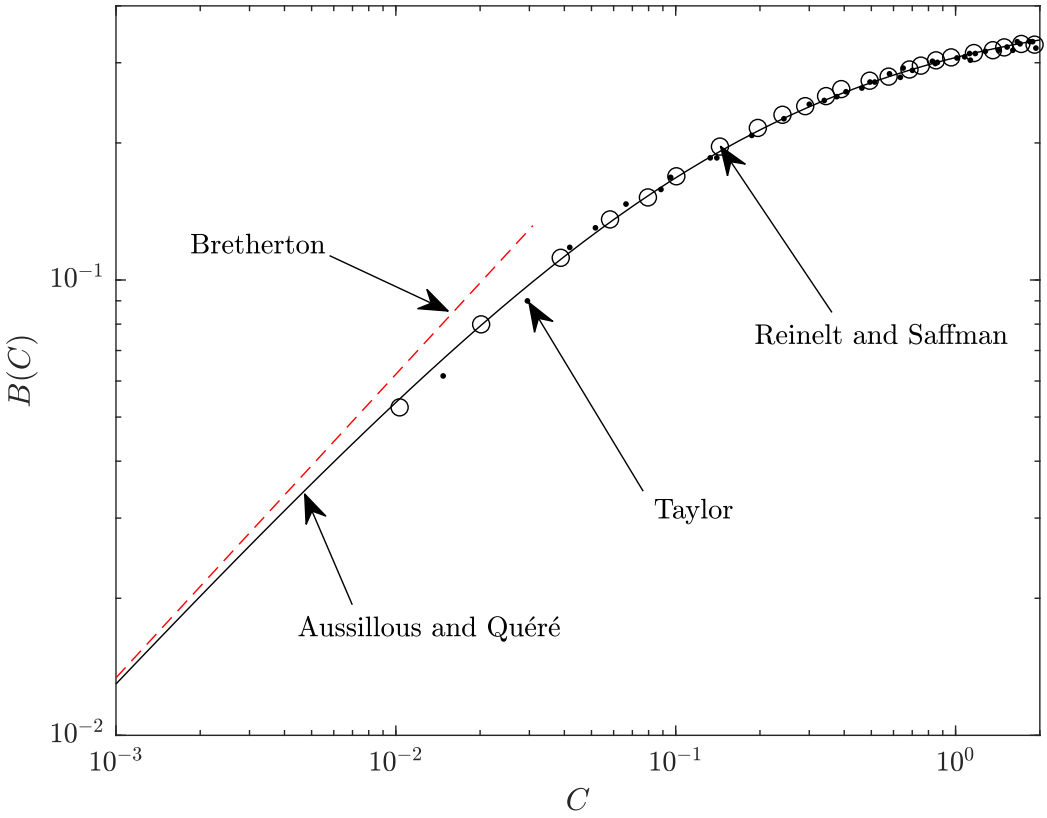

Figure 2.1: Plot of the uniform film thickness in an axisymmetric geometry computed numerically by Reinelt & Saffman (1985), compared with the experimental results of Taylor (1961) and Bretherton's asymptotic result for the low capillary number limit. The empirical fit (2.17) found by Aussillous & Quéré (2000) is overlayed as a solid line.

2.1.3 Nonlinear curvature models

Maintaining the full form of the curvature, rather than simplifying to the linearised form $\kappa \approx h_{xx}$, is necessary when resolving interfaces with finite gradients (Snoeijer, 2006). Ratulowski & Chang (1989) solved the lubrication equations in an arc-length-angle coordinate system, incorporating nonlinear curvature into their description of a steady, isolated, elongated bubble. Rather than assuming a hemi-spherical front as in Bretherton, they derive a travelling wave formulation of the lubrication model that retains nonlinear curvature of the interface at the bubble front. The model is shown to follow the Bretherton prediction of wet-

ting film thickness in the small capillary number limit, as well as exhibiting good agreement with numerical solutions of Reinelt & Saffman (1985) for capillary numbers up to $C \approx 0.1$. The framework focuses on the steady state and does not allow for time-dependent phenomena such as bubble pinch-off.

Lu *et al.* (2023) retained the full nonlinear expression for interface curvature in their study of bubble generation in a tapered capillary, similar to Ratulowski & Chang (1989) who considered the nonlinear curvature lubrication framework in the context of an isolated bubble. Lu *et al.* (2023) briefly consider a one-dimensional time-dependent equation for the bubble interface within a lubrication framework. The numerical solutions to the unsteady lubrication equation visually depict the progression of the bubble towards a state of pinch-off, predicting a bubble diameter that exhibits good agreement with experimentally obtained results. Since the experimental results suggest a slow-moving bubble front, the authors choose to fix the front of the bubble so as to avoid solving for this moving boundary, and also terminate the interface early to avoid the infinite slope near the nose.

2.2 Pinch-off dynamics and bubble formation

The growth and subsequent pinch-off of a bubble from an orifice or needle into a stagnant liquid pool has been widely investigated due to its simplicity (e.g. Davidson, 1960; Marmur & Rubin, 1976; Oguz & Prosperetti, 1993). However, the bubbles produced are not small enough for many engineering applications. To reduce the size of the bubbles produced, the gas stream can be injected within a co-flowing immiscible fluid, as is commonly employed in microfluidic devices. There is a variety of different geometries of microfluidic device (see figure 1.1). However, it is common to choose either a co-flow or flow-focusing geometry allowing the production of microbubbles within a narrow distribution of the desired size (Martín-Banderas *et al.*, 2005). In a coflow configuration, the gas phase is injected in parallel into a coaxially aligned capillary tube containing the continuous liquid phase such that an interface is formed upstream of the orifice. A flow-focusing device builds upon this geometry with a focusing orifice that is

placed downstream of the gaseous outlet. Another common geometry used in microfluidic devices is the T-junction where the two phases meet at the intersection of two perpendicular channels.

2.2.1 Jet break up and capillary instabilities

A fluid film coating the interior of a capillary tube is unstable due to surface tension effects whereby the film deforms to minimise its surface energy. The phenomenon is classified in the family of instabilities referred to as the Rayleigh-Plateau instability (Plateau, 1873; Rayleigh, 1878, 1879). The same Rayleigh-Plateau instability drives the breakup of a fluid jet into droplets. While the governing equations of jet dynamics differ fundamentally from those considered within this thesis, we draw conceptual similarities between the modelling approaches employed, particularly with respect to nonlinear curvature models.

When modelling jets, it is common to employ the slender-jet (or long-wave) approximation, whereby the variations in the axial coordinate are much slower than in the direction of the jet radius. Hence, the Navier-Stokes equations reduce to one-dimensional models known as the slender jet equations (Bechtel *et al.*, 1992; Eggers & Dupont, 1994; Papageorgiou, 1995). These differ from the equations of lubrication theory which describe a shear dominated model. In order to model the dynamics of a jet up until the point of pinch-off, the full nonlinear curvature must be retained to account for larger interfacial gradients at the neck. Whilst the nonlinear curvature model is inconsistent with the long-wave approximation, it is shown to increase the accuracy of one-dimensional analyses (Ambravaneswaran *et al.*, 2002; Brenner *et al.*, 1997; Eggers, 1997).

In an axisymmetric geometry, it is well known that quiescent fluid threads are unstable and break into droplets due to the surface-tension-driven Rayleigh-Plateau instability. This phenomenon is commonly observed in industrial processes and can be exploited to generate uniform droplets with industrial applications such as inkjet printing and microfluidics (e.g. Derby, 2010; Eggersdorfer *et al.*, 2018; Maîtrejean *et al.*, 2024). A cylindrical jet of fluid is also unstable to perturbations, and any perturbations of wavelength larger than the jet radius will exhibit exponential growth. The Rayleigh-Plateau instability causes the jet to

thin until its radius locally goes to zero. If the jet is formed of a viscous fluid, the thinning of the jet is slow enough that inertia remains unimportant and the break up occurs in finite time. However, in the case of an inviscid jet surrounded by viscous outer fluid governed by Stokes flow, there is a singularity in the equations of motion and the thickness of the jet asymptotically approaches zero, as opposed to reaching zero in finite time (Eggers, 2000). In the limit of vanishing viscosity, the model develops a singularity such that the gradients of the local radius and the velocity at a finite thread radius diverge to infinity. Explicitly, as the neck thins towards zero thickness, the radius of curvature approaches zero and the small amount of fluid left in the pinch region of the jet is driven by increasingly stronger forces, causing the velocity to become infinite (Eggers, 1997, 2000).

2.2.2 The effect of confinement on instability

The same instabilities associated with cylindrical liquid interfaces that are observed in jets also affect liquid films deposited on the inner wall of a tube (Duclaux *et al.*, 2006). In microfluidics, the capillary instability of viscous films in tubes can be exploited to generate bubbles. In planar geometries, ribbons of fluid are stable and do not form droplets in the same way; instead, an imposed flow can be applied to initiate breakup (section 2.2.3).

Driven by the same Rayleigh-Plateau instability as for jets, films on the interior of the cylinder can grow to form an occlusive plug (Everett & Haynes, 1972). Hammond (1983) studied the evolution of an initially uniform thin film lining a straight axisymmetric capillary in a lubrication framework, under the assumption that the film is sufficiently thin. The analysis was limited to a thin film approximation only, and was not able to predict the break up of the film to form liquid lenses. Gauglitz & Radke (1988) extended the work to consider thicker films and derived a small-slope evolution equation containing an improved approximation for the interfacial curvature. As a result, the upgraded framework was able to model the formation of a liquid bridge, a feature that could not be predicted by Hammond's thin film model.

In coflow microfluidic geometries, the dispersed phase is injected through a central tube, while the immiscible continuous phase flows around it in an outer

coaxial tube. At large flow rates, the dispersed phase forms a continuous jet that undergoes breakup downstream of the input nozzle, driven by the Rayleigh-Plateau instability (Utada *et al.*, 2007). The breakup mechanism, referred to as the jetting regime, is essentially the same instability mechanism as was considered by Hammond (1983) and Gauglitz & Radke (1988) in the context of interior coatings of cylinders, but the fluids are now injected. For sufficiently long jets, axisymmetric perturbations cause localised thinning resulting in an increased curvature and a resultant increase in the pressure difference at the interface between the inside and the outside of the jet (Guerrero *et al.*, 2020). The higher pressure inside the jet drives fluid along the jet axis out of these regions, causing it to thin progressively and ultimately break up into droplets. The detachment is caused by a local balance between surface tension drawing fluid away, and the viscous drag of fluid opposing change.

Many works have used linear stability analysis to understand how perturbations result in jet breakup (e.g Gordillo *et al.*, 2001; Plateau, 1873; Rayleigh, 1878). When a jet is injected into a second moving fluid, the motion of both the outer fluid and the fluid in the jet will affect breakup. The breakup of a fluid thread in the jetting regime happens when the capillary number is large, or when the ratio of the dispersed phase flow rate to the continuous phase flow rate q_d/q_c is high. In the jetting regime, viscous forces sustain the jet against immediate breakup at the input nozzle and the breakup can become irregular, leading to the formation of polydisperse droplets. As such, formation of bubbles in the dripping and squeezing regime (figure 2.2) is often preferred in microfluidics, as will be discussed in the next subsection. Both the flow parameters and the geometry of the system determine the mechanism for bubble formation. Utada *et al.* (2007) experimentally investigated the transition from dripping to jetting in coflow streams and proposed criterion of transition based on competition between interfacial tension, viscous forces and inertia forces. Additionally, confinement raises the volume threshold or suppresses the instability entirely, shifting the breakup mechanism to dripping/squeezing. Humphry *et al.* (2009) studies the effect of geometric confinement on the stability of the inner fluid thread formed by coflowing liquids in a microfluidic channel. In particular, their experimental analysis shows that only threads with widths considerably less than the channel

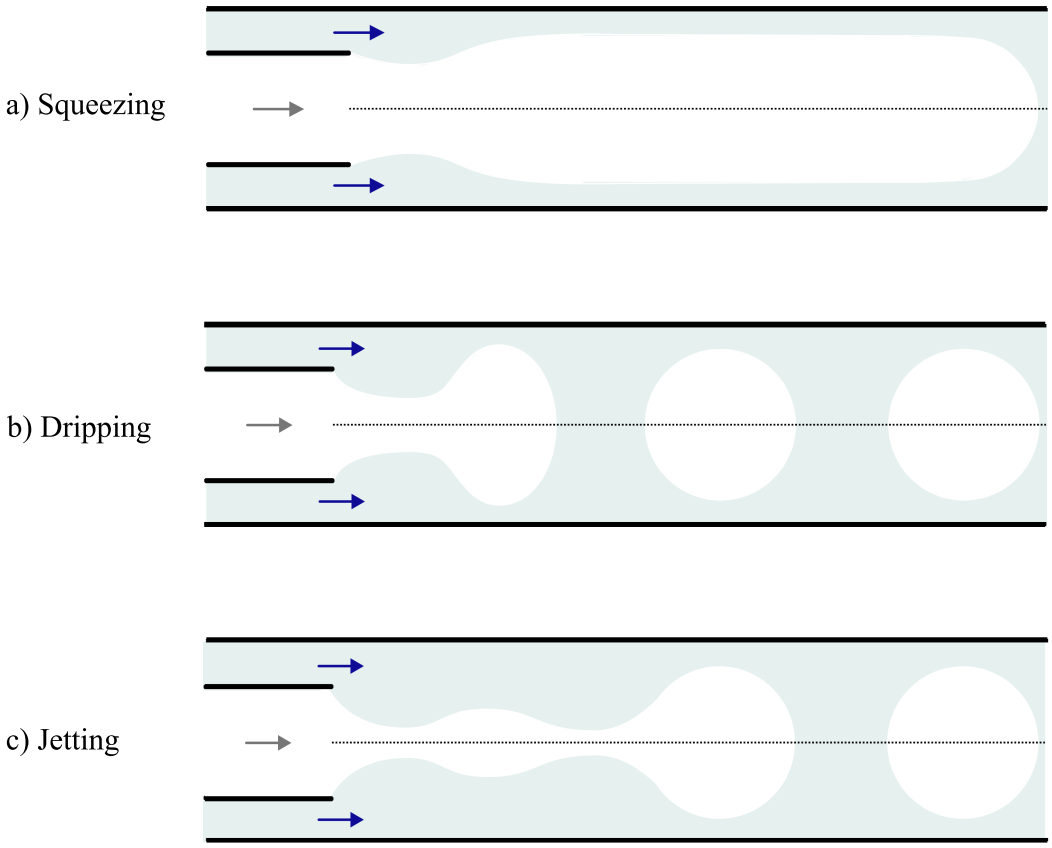

Figure 2.2: The squeezing mechanism for bubble formation forms long, elongated Taylor bubbles, whereas the dripping mechanism forms smaller, more circular bubbles at higher frequency. In the jetting regime, a deformed thread breaks up into bubbles downstream of the nozzle.

height can break into droplets, either in a dripping or jetting regime. If the width of the inner fluid is comparable to or larger than the channel height, hydrodynamic instabilities are suppressed and the stable inner fluid thread does not break into drops.

2.2.3 Bubble formation in the coflow geometry

In order to produce monodisperse bubbles within a specified range for volume and frequency, formation of droplets in the squeezing or dripping regimes is preferred in microfluidic devices. The squeezing regime occurs at low capillary numbers where interfacial forces that hold the bubble at the nozzle dominate (Garstecki *et al.*, 2005). The dispersed phase grows until it blocks the pipe or channel, causing a build up in pressure as the continuous phase squeezes the interface until a droplet is pinched off. The resultant droplet tends to have a plug-like shape and its length is mainly dependent on the flow rate ratio rather than on fluid properties such as surface tension or viscosity (Garstecki *et al.*, 2006). At more moderate capillary number, the formation mechanism transitions to the dripping regime (Fu *et al.*, 2010). The viscous stresses from the continuous phase cause the dispersed phase to thin and form a neck at the orifice. The neck continues to thin until the continuous phase shears off the emerging bubble, causing pinch-off at the orifice before the emergent droplet can fill the channel entirely. Many works have considered both experimental and numerical approaches to determining the critical capillary number at which the transition from squeezing to dripping occurs in a range of microfluidic geometries (e.g. Arias & Montlaur, 2020; Christopher *et al.*, 2008; De Menech *et al.*, 2008; Fu *et al.*, 2010; Garstecki *et al.*, 2006; Xu *et al.*, 2008; Zhang *et al.*, 2021).

Due to the complexity of microfluidic geometries, much of the progress in the design and optimisation of such devices is directed by experimental observations. Theoretical analysis and numerical simulations are needed to access flow parameters that cannot be measured in experiments. However, the moving boundaries of the flow are difficult to model as resolving interfacial motion is prone to numerically instability, even at low Reynolds numbers (Wörner, 2012).

The dimensionless parameters that control the rate of microbubble production include capillary number, the flow rate ratio and the viscosity ratio of the two fluids. Cubaud *et al.* (2005) presented numerical and experimental results describing the formation of Taylor bubbles in a square microchannel (of width and height w). The authors proposed a simple empirical scaling law for the length of the gas bubble generated in a cross-flow geometry, whereby the liquid phase is injected perpendicular to the gas phase:

$$\frac{L}{w} = \frac{q_c + q_d}{q_c}. \tag{2.18}$$

The flow rates of the dispersed and continuous phases are represented by q_d and q_c, respectively. The scaling is independent of the material parameters of the fluid. Since the squeezing of the dispersed phase occurs at a rate proportional to the flow rate of the continuous phase q_c, this sets the time for the growth of the bubble, which also proceeds at a rate proportional to the flow rate of the dispersed phase q_d. Combining these effects gives the scaling (2.18).

The squeezing regime is typical of low-capillary number flows, when interfacial forces dominate over shear stresses. As capillary number is increased beyond a critical value (around $C \sim 10^{-2}$), the shear stresses contribute to the break up and the system moves towards a dripping regime (De Menech *et al.*, 2008; Garstecki *et al.*, 2006). The scaling law derived by Cubaud *et al.* (2005) has been confirmed experimentally in both a co-flow geometry with square cross-section (Xiong *et al.*, 2007), and a T-junction geometry formed of microchannels with large aspect ratio (Garstecki *et al.*, 2006). To date, there has been no theoretical explanation for a law of this kind, either for idealised two-dimensional or axisymmetric coflow geometries, nor more complex flow-focusing or T-junctions such as those considered by Jensen *et al.* (2006) and Garstecki *et al.* (2004, 2005, 2006).

2.2.4 Lubrication theories for bubble pinch-off

A key theme in this thesis is the mathematical analysis of bubble pinch-off in a confined geometry. This section serves as a review of existing literature that has used lubrication models to explore bubble pinch-off in a confined geometry.

Zhao *et al.* (2018) uses a lubrication framework with linearised curvature to model the fluid-fluid interface when a viscous fluid is displaced from a circular capillary tube by a less viscous fluid in the partial wetting regime. Experiments were carried out in a glass capillary tube (750 μm in diameter) that is initially filled entirely with glycerol. One end of the capillary tube is open to the atmosphere and the other is connected to a syringe pump allowing for withdrawal of glycerol and subsequent displacement by air at atmospheric pressure. At large displacement rates, an air finger forms that progresses through the tube surrounded by a film of viscous fluid. The deposited film is unstable and dewets from the wall, leading to a dynamic contact line and a pinch-off instability in finite time. The experimental results are compared with numerical solutions of the theoretical model, which is based on the long-wave approximation and describes the dewetting of the entrained film. The downstream boundary condition of the model is specified by the film thickness of the entrained liquid film, the value of which is given by the empirical function found by Aussillous & Quéré (2000) to fit the experimental data of Taylor (1961) (recall section 2.1.2). Whilst only the expression for linearised curvature (the same small-slope approximation as was used by Gauglitz & Radke (1988), $\kappa = 1/(1-h) + h_{xx}$) is used in the theoretical model, the solutions are shown to capture the growth of the interface in the necking zone well, exhibiting good agreement with experimental results for the interface evolution. The agreement between solutions calculated by the lubrication model in the necking zone and the experimental observations of the interface provides evidence that the lubrication framework is a valid method of modelling bubble pinch-off in capillary tubes.

2.3 Droplet spreading and thin films

A theme of this thesis will be to form a connection between droplet theory and pinch-off dynamics in two-phase capillary flows. In this section, we will review the fundamental theory relating to surface-tension-driven droplet spreading as a precursory to later analysis. Only the relevant ideas that are key to understanding later concepts will be considered. In particular, this includes the precursor film regularisation of the moving contact line at the front of the droplet, and

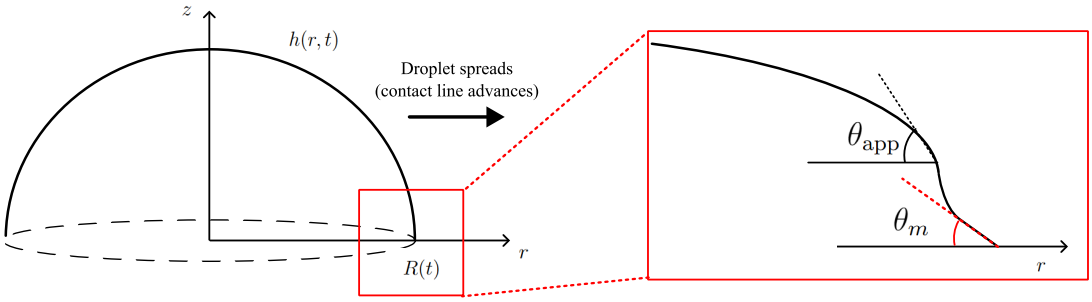

Figure 2.3: A schematic showing surface-tension-driven spreading of an axisymmetric droplet. The interface becomes highly curved near to the contact line so that the apparent contact angle θ_{app} seen on the macroscale is larger than the microscopic angle θ_m.

the asymptotic matching technique commonly employed to model the advancing droplet interface.

The spreading of a thin film is a fundamental problem observed in a range of applications including coatings on the internal sides of airways (Halpern & Grotberg, 1992), and industrial coating processes (e.g. Fraysse & Homsy, 1994; Howell *et al.*, 2013; Wilson, 1982). When gravitational effects are negligible, recall that the height of a surface-tension-driven thin film, $h \geq 0$, is commonly described by the equation (e.g. Myers, 1998)

$$\frac{\partial h}{\partial t} = -\frac{\gamma}{3\mu}\frac{\partial}{\partial x}\left(h^3\frac{\partial^3 h}{\partial x^3}\right) \equiv -q_x, \tag{2.19}$$

where q is the fluid flux. This is a fourth-order nonlinear diffusion equation, that is degenerate since the coefficient of the highest derivative tends to zero as $h \to 0$.

A particularly well-documented situation of a surface-tension-driven thin film is the spreading of a droplet of fluid over a solid substrate. If the droplet is small enough such that the capillary length ($\ell_c = \sqrt{\gamma/\rho g}$, with ρ the fluid density and g the acceleration due to gravity) is larger than drop radius, gravity is negligible and the spread of the droplet is controlled by surface tension, or driven by injection of fluid. The surface-tension-driven spreading of a fixed volume of fluid is a classical problem that has been studied in detail (e.g. Cox, 1986; Hocking & Rivers, 1982; King & Bowen, 2001; Lacey, 1982; Voinov, 1976). A three-phase

contact line is formed at the point where the liquid (droplet) phase, the surrounding gaseous phase, and the solid phase meet. Modelling the moving contact line is challenging due to the associated well-known stress singularity. The singularity arises due to a discontinuity in the boundary conditions at the contact line. Two common approaches are the Navier slip regularisation (which allows for finite slip at the contact line), and a precursor film regularisation (which eliminates the contact line by assuming that there exists a very thin film extending ahead of the droplet front). For an in-depth discussion of contact lines in the context of liquid spreading across solid substrates, the reader is directed to Dussan (1979).

In this section, we focus on the capillary spreading of a thin droplet over a horizontal substrate (figure 2.3). Due to its multiscale nature, asymptotic matching techniques are commonly used to model the evolution of the droplet front. The region near to the contact line is commonly referred to as the "inner" region where viscous and capillary forces are balanced. On a macroscopic scale, the "outer" region describes the bulk of the droplet away from the droplet front.

2.3.1 The contact line

A contact line exists at the interface of two immiscible fluids and a solid, such as at the front of a fluid droplet as it spreads over a solid substrate. The free surface at the front of the droplet gives rise to a moving contact line as the droplet fluid displaces the surrounding fluid. A well-known stress singularity occurs at the moving contact line in the spreading of thin films (Huh & Scriven, 1971). The singularity arises due to a discontinuity in the boundary conditions at the contact line: the interfacial motion of the droplet front suggests that the fluid at the contact line should move with some velocity, whereas the no-slip condition indicates that the fluid should be stationary at this point. Different approaches are available to resolve the singularity, and each relies on the relaxation of one of the incompatible boundary conditions.

To regularise the singularity, one can introduce a precursor film in front of the droplet that smooths the interface at the contact line and results in a well-posed problem (figure 2.4). The precursor layer is assumed to have a very small but finite thickness that prewets the substrate and alters the boundary conditions

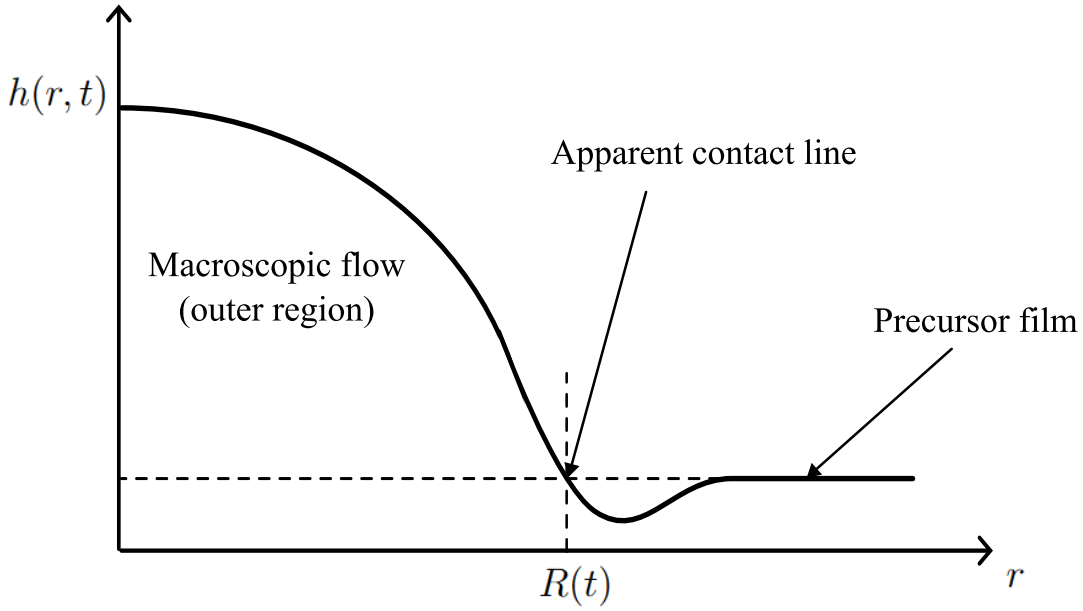

Figure 2.4: A schematic to show the regularisation of the moving contact line and the corresponding outer, transition and precursor-layer regions, as well as the position of the apparent contact line (not to scale).

of the problem such that the height of the film no longer reaches zero. Under a precursor film regularisation, there exists a "transition region" whereby the droplet thickness adjusts to the precursor film thickness. The contact line of the droplet is replaced by an "apparent" contact line at which the profile must match to the precursor film. Whilst the contact line is allowed to be defined as any point in the transition region, it is commonly defined as the first point at which the droplet thickness is equal to the precursor film thickness (Kiradjiev *et al.*, 2019). The spreading of a thin droplet regularised by a precursor film, as shown in figure 2.4, is the configuration we shall focus on reviewing here.

As the precursor film is thin, there is a separation of length scales between the macroscopic droplet and the microscopic precursor film. On a macroscopic scale, the spreading of the droplet is slow enough that the droplet is effectively in equilibrium. We can divide the droplet into an outer region (where the film thickness is approximated by sphere with uniform curvature) and an inner region near the contact line (governed by the Landau-Levich equation (2.12)). In the

case of a spreading isolated droplet, moving boundary theories for the contact line can be implemented alongside an asymptotic approximation of quasi-static flow. Under the quasi-static approximation, the dynamics of the film is simplified substantially and the shape of the droplet can be taken as a simple paraboloidal profile which is matched to a linear profile at the contact line (Cox, 1986; Voinov, 1976).

2.3.2 Asymptotic matching

As an illustrative example of the asymptotic matching technique, we review Bonn *et al.* (2009) and consider the case of an axisymmetric droplet spreading on a surface which it wets completely. The system is defined in terms of polar coordinates (r, θ) due to the radial symmetry of the droplet.

We consider the static shape of a droplet in equilibrium at a particular point in time. The pressure jump across the interface is constant due to the Young-Laplace equation

$$\Delta p = \gamma \left(\frac{1}{R_1} + \frac{1}{R_2} \right). \tag{2.20}$$

For an axisymmetric droplet, the two principal radii of curvature correspond to the curvature in the plane of symmetry, and the curvature in the azimuthal direction (around the axis). Hence, the mean curvature of the axisymmetric surface $z = h(r)$ is

$$\frac{1}{R_1} + \frac{1}{R_2} = \frac{h_{rr}}{(1 + {h_r}^2)^{3/2}} + \frac{h_r}{r\sqrt{1 + {h_r}^2}}, \tag{2.21}$$

as derived from the geometry of a surface of revolution (e.g. Batchelor, 2000; De Gennes *et al.*, 2003) and the Young-Laplace equation becomes

$$\frac{1}{r}\frac{\mathrm{d}}{\mathrm{d}r}\left(\frac{r h_r}{\sqrt{1 + {h_r}^2}} \right) = \frac{\Delta p}{\gamma}. \tag{2.22}$$

If the droplet is assumed to be sufficiently flat ($h_r \ll 1$), $\sqrt{1 + {h_r}^2} \approx 1 + \frac{1}{2}{h_r}^2$, and the expression simplifies to leading order as

$$\frac{1}{r}\frac{\mathrm{d}}{\mathrm{d}r}\left(r h_r \right) = \frac{\Delta p}{\gamma} = \text{constant}. \tag{2.23}$$

Integrating (2.23) twice, and using that the gradient of the droplet is finite at $r = 0$, the interface can be shown to approximate a paraboloid with zero height at the radius of the droplet R

$$h(r) = h_0 \left(1 - \frac{r^2}{R^2}\right). \tag{2.24}$$

To determine the height of the droplet at its centre h_0, we impose the boundary conditions

$$h(R) = 0, \qquad h_r(0) = 0, \qquad \int_0^{2\pi} \int_0^R h(r)\, \mathrm{d}r\, \mathrm{d}\theta = V. \tag{2.25}$$

The resulting expression for the droplet interface is

$$h(r) = \frac{2V}{\pi R^2} \left(1 - \left(\frac{r}{R}\right)^2\right). \tag{2.26}$$

The contact line $R(t)$ is time-dependent, but the shape of the droplet interface (2.26) is instantaneous such that, at each time t, the droplet remains a paraboloid.

Near to the contact line, $r \to R$, the outer solution can be expanded, to leading order, as

$$h_{\text{outer}} \sim -\frac{4V}{\pi R^3}(r - R) \qquad (r \to R), \tag{2.27}$$

giving a linear approximation for the droplet interface near to its rim. For thin droplets, we can apply the small angle approximation at the edge of the droplet as $-h_r(R) = \tan(\theta_{\text{app}}) \approx \theta_{\text{app}}$ such that (2.27) simplifies as

$$\theta_{\text{app}} = \frac{4V}{\pi R^3}, \tag{2.28}$$

and the apparent contact angle tends to zero as the droplet spreads and becomes increasingly thin.

The generalised form of the interface profile for intermediate scales can be written in terms of the outer variables as the Cox-Voinov equation (Cox, 1986; Voinov, 1976)

$$\theta_{\text{app}}^3 - \theta_m^3 = 9\, C \log(L/\lambda), \tag{2.29}$$

where the typical scale of the outer solution L and the microscopic scale λ are well separated, and the rate at which the contact line changes over time $\dot{R}$ is

equivalent to the speed of the droplet front so that $C = \mu\dot{R}/\gamma$ is the capillary number. The characteristic length defined by the microscopic cut-off λ, which is the only specific feature of the contact line, enters only logarithmically. The expression (2.29) was first derived by Voinov (1976) to describe the behaviour of the intermediate region in the asymptotic limit as it matches to the macroscopic problem. The same expression was found by Cox (1986), who implemented the three-region matching procedure to describe general contact-line motion in the full Stokes regime. It was later shown by Eggers (2005a) in the lubrication framework, and Sibley *et al.* (2015) in a more general Stokes flow case, that the cube of the interface slope between inner and outer regions can be directly matched, removing the requirement for an intermediate region.

In order to match the outer droplet shape to the inner solution near to the contact line, we require the value of the slope near the droplet rim. In the transition region, (2.19) can be integrated once to find a third order ordinary differential equation for the shape of interface, represented by the Landau-Levich equation as derived in the different context of matching to a spherical bubble cap in section 2.1.2,

$$\frac{\partial^3 \eta}{\partial \xi^3} = \frac{\eta - 1}{\eta^3}. \tag{2.30}$$

The intermediate ordinary differential equation (2.30) is universal for contact line problems with precursor film regularisation, and the far-field boundary condition is derived from matching to the precursor film thickness as

$$\eta \to 1, \qquad (\xi \to \infty). \tag{2.31}$$

The equation (2.30) was originally derived in the context of dip coating to describe the thickness of the fluid film left on a moving plate as it is withdrawn from a fluid, but was subsequently used by Bretherton (1961) to describe the wetting layer that surrounds a bubble flowing through a capillary tube (as was discussed in section 2.1.2). Such third order differential equations are common when describing the viscocapillary balance in the inner region of thin fluid film, such as in spin coating flows (e.g. Emslie *et al.*, 1958; Melo *et al.*, 1989; Wang *et al.*, 2025). The specific governing equation of the system depends on the boundary conditions and the geometry of the problem (Tuck & Schwartz, 1990).

In the context of droplet spreading, the Landau-Levich equation (2.30) describes the region close to the contact line. The boundary conditions required to solve the steady third-order equation come from specifying the value of the solution and its gradient near to the contact line. We require the upstream solution of the inner system in order to establish a matching condition linking to the outer solution. To determine the analytical form of the asymptote of the inner solution as $\xi \to -\infty$, we note that, since $\eta \to \infty$ in this limit, the equation simplifies asymptotically to $\eta_{\xi\xi\xi} \sim 1/\eta^2$. This equation describes the balance between the capillary and the viscous stresses in a thin film in the absence of gravity and its exact solution involving Airy functions is given in Duffy & Wilson (1997). The asymptotic solution is

$$\eta \sim -\xi[9\log(-\xi)]^{1/3} \qquad (\xi \to -\infty). \tag{2.32}$$

The exact profile $\eta(\xi)$ is dependent on the regularisation used, but the asymptotic limit that is required to match to the outer solution is universal. Transforming the inner matching condition (2.32) into outer variables gives the exact version of the Cox-Voinov law (2.29) required for the particular problem. The expression can be differentiated and used to match to a quasi-static outer region; there is a substantial amount of literature that follows this method.

In droplet spreading, the length scale L is often specified by the droplet radius $L \sim R$, while the inner length depends on the regularisation used (either a precursor film thickness, or a slip length). If the system is regularised by a precursor film, then the microscopic contact angle is fixed as $\theta_m = 0$ since the surface where the interface meets the precursor film is smooth in a microscopic sense, meaning there is no geometric corner. However, the macroscopic contact angle, which arises over a larger scale where the interface increases from the precursor film thickness to the droplet height h, is finite. In this case, substitution of (2.28) into (2.29) gives an ordinary differential equation

$$\left(\frac{4V}{\pi R^3}\right)^3 = \frac{9\mu\dot{R}}{\gamma}\log\left(\frac{R}{h_\infty}\right). \tag{2.33}$$

The ordinary differential equations derived for two-dimensional droplet in the context of surface-tension-driven spreading (King & Bowen, 2001) or injection-driven spreading (Kiradjiev *et al.*, 2019) differs from (2.33) in the power of R.

Explicitly, due to the difference in volume constraints, the denominator contains a power R^6 in the case of two-dimensional droplet spreading, as opposed to R^9 in the axisymmetric analogue.

Integrating the ordinary differential equation (2.33), we recover a version of Tanner's law (Tanner, 1979)

$$R(t) \sim \left[\left(\frac{4V}{\pi} \right)^3 \frac{10\gamma t}{9 \log(R/h_\infty)\mu} \right]^{1/10} . \tag{2.34}$$

The logarithmic factor varies slowly and is often treated a constant $\log(L/\lambda) \equiv \mathcal{L}$ such that Tanner's law is robust to the choice of regularisation (Bonn *et al.*, 2009). The spreading law (2.34) is a particular form of Tanner's law (Tanner, 1979), generally written as

$$R(t) = K \left(\frac{\gamma V^3}{\mu} t \right)^{1/10} , \tag{2.35}$$

where K is a constant coefficient determined by the contact line and the geometry of the problem. The experimental results of Tanner (1979) highlight the robustness of the spreading law as the prefactor remained order unity for all fluid-substrate combinations considered. The power law $R \propto t^{1/10}$ has been observed experimentally for many studies on the spreading of thin droplets (e.g. Cazabat & Stuart, 1986; Levinson *et al.*, 1988; Ogarev *et al.*, 1974). The scaling exponent α in the spreading law for the droplet radius $R \sim t^\alpha$ depends on the driving forces and the configuration considered. For example, the exponent in the spreading of a two-dimensional droplet $\alpha = 1/7$ (King & Bowen, 2001; McHale *et al.*, 1995; Tanner, 1979) differs from the three-dimensional case considered above.

There is a large body of research that builds on classical surface-tension-driven spreading problems, for example by considering different driving forces such as gravity (Hocking, 1983), or contributions to the macroscopic behaviour of the spreading drop due to the presence of surfactants (Jensen & Naire, 2006). King & Bowen (2001) use a lubrication framework to describe the surface-tension-driven spreading of a droplet along a horizontal surface that is prewetted with a thin film. The method was extended by Kiradjiev *et al.* (2019) to account for the injection of liquid into a droplet, and it was found that, at late times, the apparent contact line moved much faster in the case of constant injection ($\sim t^{4/7}$)

compared with the spreading of a fixed volume ($\sim t^{1/7}$). The outer, macroscopic shape of the droplet is a parabolic profile in each study. In our analysis of bubble pinch-off in a coflow geometry, we shall notice that the fluid-fluid interface in the necking zone region behaves similarly to the growth of a droplet that is fed by constant injection of fluid. In particular, the shape of the interface in the necking zone is concluded to be approximately parabolic with a front that spreads as $t^{4/7}$.

2.4 Research questions

The injection of a gas into a flowing liquid stream to form bubbles has been successfully employed in the context of microfluidics. Many advancements in the field are driven by experimental findings which are limited to the specific operating conditions and fluid parameters considered in the experiments. As highlighted by Fu & Ma (2015), theoretical developments are required to fully understand small-scale bubble formation mechanisms, as well as develop scaling laws for coflow devices. In particular, the scaling law for the length of a Taylor bubble produced by a cross-flow device of square cross-section presented by Cubaud *et al.* (2005) has been confirmed across a variety of microchannel geometries, but to-date no theoretical explanation exists.

This thesis aims to provide a detailed mathematical analysis of bubble pinch-off in a general context for the coflow system by deriving expressions for pinch-off frequency (and therefore bubble volume) that hold in the Taylor flow regime, which is observed across a range of operating conditions. As well as asymptotic models, we aim to provide a generalised lubrication framework for the periodic formation of bubbles at regular intervals. We hope that this thesis acts as a step towards a more rigorous understanding of the bubble formation mechanisms in coflowing devices. The primary contributions of this work can be summarised into three specific research questions, which form the basis of the subsequent chapters of this thesis.

1. Taylor bubble pinch-off in a planar channel.

We begin by considering the planar geometry as a necessary foundation for the more complicated axisymmetric geometry. By considering a lubrication theory for the necking film between the bubble injection nozzle and the film thickness surrounding the extending Taylor bubble, we conduct a mathematical study of the growth and pinch-off dynamics of two-dimensional Taylor bubbles, yielding analytical insight into the necking dynamics of the film and the parametric control of pinch-off frequency. We draw a novel theoretical connection between the growth of the viscous fluid film in the necking zone, and the quasi-static injection-driven dynamics of spreading two-dimensional droplets. Our asymptotic analysis derives the first theoretical law for bubble pinch-off time t_* as $t_* \sim 1/q_c^{4/3}$, where q_c is the input flux of the liquid phase.

The model framework is limited to the formation of a singular bubble as the model framework is unable to resolve the infinite gradients required at the rear of the newly formed bubble, and the front of the subsequent bubble. In order to examine the full oscillatory bubble pinch-off cycle, nonlinear curvature terms are necessary to resolve the large interfacial gradients.

2. A nonlinear curvature framework for periodic bubble formation.

In order to examine the entire, periodic pinch-off cycle, we present a lubrication model that retains the nonlinear expression for curvature to describe the entire bubble shape, including the larger interfacial gradient associated with the front and rear of the bubble. We extend the nonlinear curvature lubrication framework considered by Ratulowski & Chang (1989) in the context of steady, isolated, elongated bubble to also allow for time-dependent phenomena such as bubble pinch-off. The model is developed in a coflow geometry, and we are able to integrate beyond the point of pinch-off to produce a train of bubbles at regular intervals and confirm the previously derived 4/3 power law for bubble pinch-off time. The model limitations are discussed, and we conclude that the main advantages of the framework are the ease of implementation, and the versatility in describing dynamic phenomena.

3. Taylor bubble pinch-off in an axisymmetric capillary tube.

Outside of providing theoretical inroads into the study of more complex geometries, we recognise that analysis of the planar configuration is limited since, in practice, an axisymmetric geometry is more representative of microfluidic devices.

Next, we consider the formation of bubbles upon the injection of an inviscid fluid into a viscous flow in an axisymmetric capillary tube. We demonstrate significant differences between the bubble pinch-off dynamics in planar and axisymmetric geometries. The axisymmetric pinch-off dynamics is controlled by a quasi-static regime of interfacial shapes up until a critical time at which quasi-static solutions spontaneously cease to exist, differing significantly from the planar geometry where the interfacial shape of the necking disturbance could be described by quasi-static solutions all the way up until pinch-off. Beyond this point, a rapid acceleration in the rate of necking occurs, resulting in pinch-off almost immediately thereafter. Hence, the pinch-off dynamics of the axisymmetric geometry is entirely different to the planar case, and involves more complex considerations relating to the existence of quasi-static solutions. Asymptotic analysis of the quasi-static evolutions, combined with the association between a loss of a quasi-static solution and pinch-off yields a theoretical law that directly aligns with the experimentally observed scaling law proposed by Cubaud *et al.* (2005) as $t_* \sim 1/q_c$. The result delivers a key theoretical development in providing the first mathematically derived scaling law, which is subsequently validated using existing experimental results.

Chapter 3

Theory of Taylor bubble pinch-off in planar coflow

The dynamics of two-fluid capillary flows in channels and pipes underlies numerous applications in biophysics, microfluidics and other industrial processes. Examples include cooling systems and heat exchangers (e.g. Redo *et al.*, 2019; Suwankamnerd & Wongwises, 2015), aeration within food processing (e.g. Zúñiga & Aguilera, 2008), biological flows in capillaries (e.g. Kim *et al.*, 1986; Ponalagusamy & Tamil Selvi, 2015), and two-phase flow in porous media (e.g. Wong *et al.*, 1995). Another key application is microfluidic devices designed to generate bubbles, which are used commonly as a contrast agent for ultrasound imaging, and as delivery vehicles in the targeted destruction of tumorous tissues (e.g. Lee *et al.*, 2017; Raisinghani & DeMaria, 2002; Tsutsui *et al.*, 2004; Vladisavljević *et al.*, 2013). A key aspect of these applications is the control of both the size and frequency of bubbles produced. The most common approach when studying bubble production is experimental investigation (see, for example, review articles by Fu & Ma (2015) and Khan *et al.* (2025) and references therein). The analysis presented herein includes, to our knowledge, the first detailed mathematical analysis of bubble pinch-off in the coflow system. The study yields explicit theoretical results that could be used as a basis for testing numerical models, and a basis for understanding flow regimes of injection-driven pinch-off phenomena in capillary systems. A key result of the analysis is to establish a physical and mathematical link connecting pinch-off dynamics in capillaries with quasi-static modelling and

matching to dynamic contact lines, of the kind used widely in modelling droplet spreading (Hocking, 1982).

Microfluidic devices typically comprise narrow channels of rectangular cross-section designed to control the motion, stability and pinch-off of bubbles (e.g. Garstecki *et al.*, 2006). Their geometries can be tuned in order to produce bubbles of specified size and frequency (e.g. Ma *et al.*, 2024). Owing to the complexities of many microfluidic geometries and the challenge of modelling the deformable fluid-fluid interface, advancements in the field are often driven by experimental observations, with scaling laws inferred empirically. While there is a variety of microfluidic geometries leading to bubble production, of the most fundamental is coflow, comprising a parallel-walled capillary containing a flowing continuous phase (often a viscous liquid) into which is injected the dispersing (bubble) phase via a nozzle placed centrally to the capillary (e.g. Castro-Hernández *et al.*, 2011; Haase, 2017; Salman *et al.*, 2006; Utada *et al.*, 2007; Van Hoeve *et al.*, 2011; Wang *et al.*, 2013; Zhang *et al.*, 2014).

When the injection flux of the bubble is sufficiently larger than that of the liquid phase, elongated capsular bubbles are formed that either completely fill the channel, or have at most a thin fluid film surrounding them (Triplett *et al.*, 1999). This regime persists over a wide range of operating conditions and is the most common flow pattern observed for low liquid-to-gas flux ratios (Chen *et al.*, 2009). The regime of long bubbles, known as *Taylor bubbles*, possess favourable characteristics such as stable flow patterns and large surface to volume ratios for more efficient heat transfer, thus making the production mechanisms of Taylor bubbles a key research problem. In the context of cross-sectional channels of order-unity aspect ratio within a T-junction system, the length of a Taylor bubble is observed to be linearly related to the ratio of the fluxes of the continuous phase and the bubble injection flux (Garstecki *et al.*, 2006). Assuming the Taylor bubble has an approximately cylindrical shape, the scaling law proposed by Garstecki *et al.* (2006) is equivalent to a linear correspondence between bubble pinch-off time and the inverse of the input flux for the outer viscous fluid. The scaling has been confirmed with use of numeric simulations in a similar flow-focusing geometry by Jensen *et al.* (2006), and experimentally in both a coflow geometry in a rectangular channel (Xiong *et al.*, 2007), and a cross-flow geometry

of square cross-section (Cubaud *et al.*, 2005). To date, there has been no theoretical explanation of a law of this kind, either for idealized two-dimensional or axisymmetric coflow geometries, nor for more complex cross-flow or T-junction configurations (Cubaud *et al.*, 2005; Garstecki *et al.*, 2006).

A pinch-off phenomenon in capillaries that has received particular theoretical attention to date is that which arises from the Rayleigh-Plateau instability of fluid films coating the interior of an axisymmetric capillary tube (e.g. Camassa & Ogrosky, 2015; Everett & Haynes, 1972; Frenkel *et al.*, 1987; Gauglitz & Radke, 1988; Goren, 1962; Hammond, 1983; Kerchman, 1995). A film of fluid covering the interior of a tube is unstable due to surface tension effects whereby the film deforms to minimise its surface energy. The azimuthal (hoop) curvature of the coating film generates a positive feedback whereby the driving surface tension increases as the azimuthal radius of curvature narrows, creating regular periodic patterns between crests and troughs, which grow and ultimately lead to pinch-off. A linear stability analysis of a liquid-lined tube was performed by Hammond (1983) using lubrication theory. The interface was described by the thin-film approximation of the Young-Laplace equation, but the analysis was not able to predict the break up of the film to form liquid lenses. Gauglitz & Radke (1988) extended the analysis beyond thin films, instead using the small-slope approximation as a more accurate estimate of the curvature. By adjusting the curvature expression to account for the azimuthal curvature effects, they were able to predict the break-up of the fluid film if its thickness was above a critical threshold. A related problem was considered by Zhao *et al.* (2018) and Pahlavan *et al.* (2019) in which Taylor bubbles of air are formed by the withdrawal of glycerol, and subsequent displacement by air, in a capillary tube. It was shown that the pinch-off time was influenced by both the wettability and flow rate, with glycerol being only partially wetting and therefore forming droplets of finite contact angle rather than a uniform wetting film, being the key controls of pinch-off time. Pahlavan *et al.* (2019) derived a similarity solution to describe the bubble dynamics just prior to pinch-off in an axisymmetric capillary tube. Their analysis is not applicable to the planar geometry, where pinch-off is attributed to the meeting of two interfaces along the centreline of the channel.

Lu *et al.* (2023) derive a one-dimensional time-dependent equation for the bubble interface within a lubrication framework which is used to provide a verification of the possibility of spontaneous bubble pinch-off observed within a tapered experimental capillary. They present solutions to the unsteady lubrication equation and include the exact nonlinear expression for curvature to show the evolution of the fluid-fluid interface until the point of pinch-off. The results are consistent with the results of Zhao *et al.* (2018) when the taper angle is zero. Since the experimental results suggest a slow-moving bubble front, the authors choose to fix the front of the bubble so as to avoid solving for this moving boundary, and also terminate the interface early to avoid the infinite slope near the nose. Despite the simplifying assumptions of the model, numerical solutions show good agreement between the bubble diameters predicted by the lubrication model and experimental findings.

Most previous literature on Taylor bubble pinch-off focuses on the form of the solution in the final stages prior to pinch-off, or its inception in the context of Rayleigh-Plateau induced necking. Whilst there exists literature on the final stages of pinch-off, the initial, primary necking phase that is a key component in injection-driven pinch-off, as defined microfluidic bubble generation, has received no detailed theoretical attention. This chapter presents novel mathematical analysis of the interface dynamics in the dominant stage of necking leading into pinch-off. To date, there exists no detailed theoretical analysis to explain the experimentally observed scaling laws for Taylor bubble pinch-off in small channels. As an initial theoretical inroad for the exploration of bubble formation in a capillary tube, we consider a simple coflow geometry whereby both fluids are injected simultaneously and in parallel with one another.

By formulating a lubrication framework for the dynamics of the bubble in the necking region and matching to a downstream thickness prescribed by the Taylor bubble, we derive the first theoretical prediction for the time to pinch-off. We conduct a detailed asymptotic study resulting in novel predictions of bubble pinch-off time. The analysis is motivated particularly by the need to explain scaling laws of the kind proposed by Garstecki *et al.* (2006), where Taylor bubbles are formed by the necking of a surrounding liquid phase. We begin here with the idealised problem of a two-dimensional coflow geometry, as would apply to a

two-phase concurrent flow through a narrow slot. This problem is of interest in its own right, as perhaps the simplest model configuration of a capillary flow in which injection-driven pinch-off can occur, and as a first step towards addressing more complex axisymmetric and three-dimensional situations with order-unity cross-sectional aspect ratios that typify many microfluidic configurations. The axisymmetric configuration, in particular, introduces fundamental new complexities due to azimuthal curvature, and thus the two-dimensional geometry provides an idealised first step. A key development is to introduce the asymptotic framework of quasi-static modelling, commonly used in the analysis of droplet spreading (e.g. Hocking, 1982; Kiradjiev *et al.*, 2019) to capillary pinch-off, wherein approximately static interfacial dynamics are coupled to an apparent contact line.

In §3.1, we derive the model for two-dimensional bubble pinch-off based on matching a lubrication model of the necking disturbance to a downstream extending Taylor bubble. Illustrative solutions to the lubrication model are shown in §3.2, demonstrating the pinch-off as the bubble thickness thins to zero in the necking region, and exploring the general dependence of the pinch-off time on key dimensionless parameters. We formulate a quasi-static theory for necking dynamics and, in turn, use it to develop predictions for the time to bubble pinch-off, based on coupling a near-static outer region of the necking film with an apparent contact line, an approach similar to those used in droplet spreading. Asymptotic analysis of the quasi-static model yields explicit analytical predictions for the pinch-off time for the limit of small capillary number. In §3.3, we summarise the results, present dimensional predictions for bubble generation time, discuss limitations of the present study and subsequent directions, and draw comparisons with the results of experimental studies.

3.1 Theoretical development

We consider a two-dimensional capillary comprised of parallel rigid boundaries along $y = \pm d$, where d is the half-width of the capillary, assumed constant (figure 3.1). The capillary is filled with a viscous fluid of dynamic viscosity μ, which flows at a prescribed volumetric flux per unit width q_c. Interior to the capillary, an inviscid fluid is injected at a constant volumetric flux per unit width q_d via

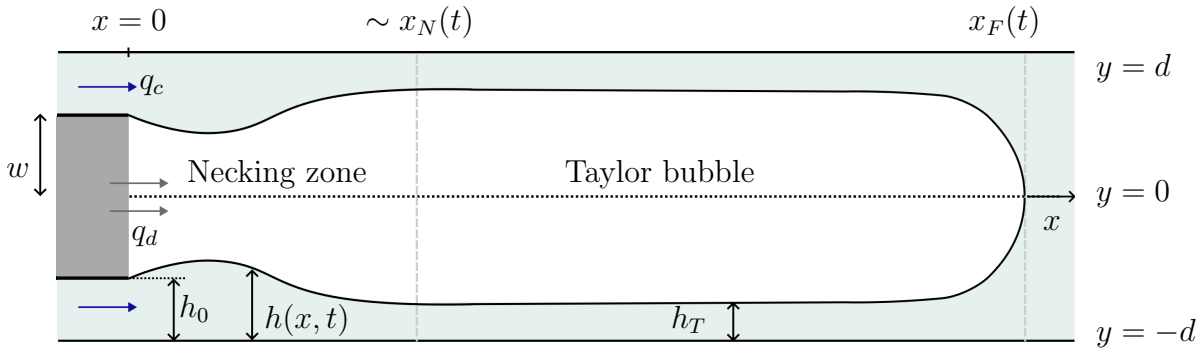

Figure 3.1: A schematic representing the asymptotic structure of a Taylor bubble formed by injection via a nozzle. The flow structure can be divided into two regions: i) the necking region where the fluid film thickens locally in the vicinity of the input nozzle, and ii) the Taylor bubble region comprising an approximately circular front connected to a region of near uniform film thickness.

an injection nozzle of half-width w. The thickness of the fluid film around the bubble is $h(x,t)$. The conditions on the film are

$$h(0,t) = h_0, \qquad q(0,t) = q_c, \tag{3.1}$$

where $h_0 = d - w$, such that the interface $h(x,t)$ is fixed at the nozzle. The set-up forms the configuration of coflow, a system that induces periodic pinch-off of the injected inviscid fluid phase (e.g. Ma *et al.*, 2024).

The development of Taylor bubbles is a dominant flow pattern and has been studied experimentally in a range of geometries including circular capillaries (e.g. Salman *et al.*, 2006; Zhao *et al.*, 2018), slit microchannels (e.g. Garstecki *et al.*, 2006) and microchannels of square cross-section (e.g. Cubaud *et al.*, 2005; Huang & Yao, 2022; Lu *et al.*, 2016; Sun *et al.*, 2025). In this regime, elongated capsular bubbles form separated by liquid slugs. A region of localised thinning forms a neck connecting the bubble to the orifice which eventually breaks at the point of pinch-off, thereby forming a train of Taylor bubbles.

Motivated by this observed flow structure, we consider the configuration in two regions: a necking zone, residing in $0 \leq x \lesssim x_N(t)$, where $x_N(t)$ is the characteristic scale of the developing necking disturbance at time t; and the extending Taylor bubble, lying in the region $x_N(t) \ll x \leq x_F(t)$, where $x_F(t)$ is the position

of the bubble cap (figure 3.1). The characteristic size of the necking disturbance, $x_N(t)$, is not known *a priori* and will, in general, grow with time. The development of a long (Taylor) bubble assumed in this asymptotic structure (as opposed to smaller bubbles, as is more characteristic when the film flux is larger than the bubble flux (Triplett *et al.*, 1999)) requires the bubble cap to lie sufficiently far ahead of the length-scale of the necking disturbance:

$$x_N(t) \ll x_F(t). \tag{3.2}$$

If the condition above applies, then the front of the bubble extends well beyond the necking disturbance, a structure also indicated both experimentally and by numerical simulations (e.g. Chen *et al.*, 2009; Cubaud *et al.*, 2005; Dang *et al.*, 2015; Garstecki *et al.*, 2006; Mei *et al.*, 2022; Salman *et al.*, 2006; Xiong *et al.*, 2007; Zhao *et al.*, 2018). Thus, the necking disturbance propagates into the uniform-thickness interior of the Taylor bubble. The self-consistency of the condition (3.2) will be evaluated *a posteriori*, with the finding that it is indeed directly based on the flux ratio q_d/q_c (section 3.2.3). In developing our model for the necking film, we consider the Taylor-bubble and necking zone, in turn, before matching the two regions.

3.1.1 The Taylor bubble

The Taylor bubble in general comprises a capsular structure with a round cap connected to a region of approximately uniform thickness in its interior (figure 3.1). The control of the film thickness in the uniform region, h_T, has received significant attention since it was first considered by Taylor (1961) and Bretherton (1961). Bretherton (1961) shows that the relative size of h_T depends crucially on the magnitude of the capillary number

$$C = \frac{\mu q_d}{\gamma d}, \tag{3.3}$$

representing the ratio of the size of viscous stresses to the size of capillary stresses on the scale of the capillary width d. For small C, Bretherton (1961) demonstrates an asymptotic structure defined by a frontal cap with a leading-order circular cross-section dominated by surface tension, that is matched to the long interior

of the bubble through a region in which lubrication theory is applied. Analysis of this structure in the context of steady travelling-wave states yields the analytical expression for the film thickness

$$h_T \sim 1.3375 \left(\frac{\mu q_d}{\gamma d}\right)^{2/3} d \equiv 1.3375\, C^{2/3} d \qquad (C \to 0), \tag{3.4}$$

implying that it is controlled by a combination of viscous, capillary and geometric parameters.

For moderate to large C, viscous stresses play an important role at the bubble cap, and a full-Stokes resolution is necessary. In general, the Taylor-bubble film thickness satisfies

$$h_T = B(C) d, \tag{3.5}$$

where $B(C)$ is a dimensionless function of C only (figure 3.2), with the property that $B(C) \sim 1.3375\, C^{2/3}$ as $C \to 0$ in conformity with (3.4). Full-Stokes numerical solutions of Reinelt & Saffman (1985) for two-dimensional Taylor bubbles determined $B(C)$ over a broad range of C for $C \gtrsim 10^{-2}$ (circular markers). For sufficiently large C, capillary stresses ultimately become negligible compared to viscous stresses, and the interior thickness saturates towards a factor multiple of the capillary width, $h_T \sim 0.45\, d$. We note that the function

$$B(C) \approx \frac{1.3375}{2.95 + C^{-2/3}}, \tag{3.6}$$

determined by an empirical fit to the data, provides a good representation (black, solid curve in figure 3.2) that captures both the small-C limiting result of Bretherton (3.4) (red, dashed) and the moderate- to large-C values determined numerically by Reinelt & Saffman (1985) in the two-dimensional case.

Mass conservation in the travelling-wave state implies that the constant translation speed of the bubble cap is given by (Bretherton, 1961)

$$U = \frac{q_d}{(1 - B)d}. \tag{3.7}$$

With t representing the time since the injection is initiated, the leading-order position of the bubble nose can be characterised by

$$x_F(t) \sim Ut = \frac{q_d t}{(1 - B)d}, \tag{3.8}$$

or simply $x_F \sim (q_d/d)t$ in the limit of $B \to 0$ arising for $C \to 0$.

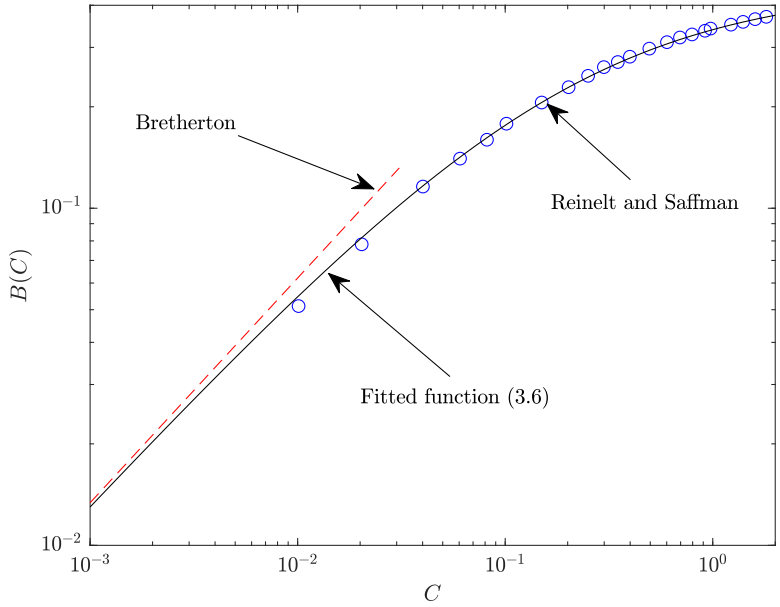

Figure 3.2: The empirical expression for the universal function $B(C)$ defining the size of the interior thickness of the Taylor bubble h_T to the capillary width, defined by (3.5). The numerical results of Reinelt & Saffman (1985) are shown as blue circular markers. The small-C result of Bretherton (1961) is shown as a red dashed line. The fitted analytical function (3.6) is shown as a solid black curve.

3.1.2 The necking zone

We define the necking zone as lying between the injection nozzle and the interior of the Taylor bubble (figure 3.1), $0 \leq x \lesssim x_N(t)$, where $x_N(t)$ is a time-dependent characteristic scale of the developing necking disturbance to be predicted. Within the necking zone, the viscous film squeezes the Taylor bubble, instigating pinch-off.

In modelling the interface evolution in the necking zone, we apply lubrication theory, based formally on the requirement that the interfacial gradient in this region is small:

$$h_x \ll 1. \tag{3.9}$$

Satisfaction of lubrication theory in the necking zone is not obvious *a priori* because the magnitude of the interfacial gradient h_x is dependent on the relative longitudinal and transverse length scales of the resulting solution, as characterised

by the aspect ratio $\sim h_m(t)/x_N(t)$, where $h_m(t)$ is the maximal film thickness:

$$h_m(t) = \max_x \left(h(x,t)\right). \tag{3.10}$$

We follow the asymptotic heuristic of adopting lubrication theory and assess the self-consistency of its predictions in maintaining $h_x \ll 1$ within the necking zone *a posteriori*.

Lubrication theory is used extensively in modelling capillary flows. Examples include liquid film breakup in capillary tubes driven by the Rayleigh-Plateau instability (e.g. Gauglitz & Radke, 1988; Hammond, 1983; Rykner *et al.*, 2024), two-phase fluid displacement in capillaries (e.g. Bretherton, 1961; Lu *et al.*, 2023; Zhao *et al.*, 2018), coating problems (e.g. Eggers, 2004, 2005b; Gao *et al.*, 2016; Landau & Levich, 1988; Snoeijer *et al.*, 2007), and capillary-driven droplets (e.g. Hocking, 1983; King & Bowen, 2001; Kiradjiev *et al.*, 2019; Savva & Kalliadasis, 2009). The governing equations of lubrication theory are

$$\mu u_{yy} = p_x, \qquad p_y = 0, \tag{3.11a-b}$$

where $u(x,y,t)$ is the longitudinal velocity of the viscous fluid, $p(x,y,t)$ is the pressure field of the viscous fluid, and we use subscripts to denote partial derivatives. With $\kappa = h_{xx}$ representing the linearised interfacial curvature, and γ the interfacial coefficient of surface tension, the interface is subject to the following conditions on the capillary wall, $y = d$, and bubble interface, $y = d - h(x,t)$:

$$u(x,d,t) = 0, \qquad u_y(x,d-h,t) = 0, \qquad [p]_{y=d-h_-}^{y=d-h_+} = -\gamma\kappa, \tag{3.12a-c}$$

representing conditions of no-slip on the sides of the capillary, no-stress at the interface with the inviscid bubble, and the jump in capillary stress across the interface, respectively. Integrating (3.11b) subject to the jump condition (3.12c), we obtain the pressure in the film,

$$p(x,t) = p_0 - \gamma\kappa(x,t), \tag{3.13}$$

where p_0 is an arbitrary constant reference pressure; owing to the assumed incompressibility of the fluids, p_0 will have no effect on the dynamics of the problem. Integrating (3.11a) twice and applying (3.12a,b), we obtain the velocity profile

$$u = \frac{p_x}{2\mu}(y-d)(y-d+2h), \tag{3.14}$$

and hence, with $\kappa = h_{xx}$, the volume flux (per unit width),

$$q(x,t) = \int_{d-h}^{d} u \, \mathrm{d}y = \frac{\gamma}{3\mu} h^3 h_{xxx}. \tag{3.15}$$

Substituting the above into the continuity equation of the fluid film, $h_t = -q_x$, we obtain the governing nonlinear hyperdiffusion equation

$$h_t = -\frac{\gamma}{3\mu} \left(h^3 h_{xxx} \right)_x . \tag{3.16}$$

Conditions (3.1) provide the two boundary conditions:

$$h(0,t) = h_0, \qquad q(0,t) = q_c. \tag{3.17}$$

We couple the necking film to the interior thickness of the Taylor bubble (3.5) by applying the matching condition,

$$\lim_{x \to \infty} h = h_T, \tag{3.18}$$

which creates a connection to the interior thickness of the film within the Taylor bubble h_T. A similar condition was applied by Zhao *et al.* (2018) in their lubrication model of capillary withdrawal. For conformity with (3.18), we apply the initial condition

$$h(x,0) = h_T. \tag{3.19}$$

Equations (3.16)–(3.19) form a closed system describing the growth of the necking film $h(x,t)$. At the time t_* defined by

$$h_m(t_*) \equiv \max_x \left(h(x,t_*) \right) = d, \tag{3.20}$$

the viscous fluid critically spans the width of the channel, defining the pinch-off time of the bubble. Our focus will be to understand the parametric dependence of pinch-off time t_*.

3.1.3 Dimensionless system

We define the following non-dimensional variables:

$$x = \left(\frac{\gamma h_T^4}{\mu q_c} \right)^{1/3} \hat{x}, \qquad t = \left(\frac{\gamma h_T^7}{\mu q_c^4} \right)^{1/3} \hat{t}, \qquad h = h_T \hat{h}. \tag{3.21}$$

Upon dropping hats, (3.16) becomes

$$h_t = -\tfrac{1}{3}\left(h^3 h_{xxx}\right)_x, \tag{3.22}$$

such that $q = \frac{1}{3}h^3 h_{xxx}$. Conditions (3.17) and (3.18) become

$$h(0,t) = \frac{H}{B}, \qquad q(0,t) = 1, \qquad \lim_{x\to\infty} h = 1, \tag{3.23a-c}$$

where $H = h_0/d$. The initial condition (3.19) becomes

$$h(x,0) = 1. \tag{3.24}$$

The pinch-off criterion (3.20) becomes

$$\max_x \left(h(x,t_*)\right) = \frac{1}{B}, \tag{3.25}$$

where $B \equiv h_T/d$ is the ratio of the bubble interior thickness to the channel half-width.

The non-dimensionalisation has reduced the dependence of the solutions to two dimensionless numbers:

$$B \equiv \frac{h_T}{d}, \qquad H = \frac{h_0}{d}, \tag{3.26}$$

representing the ratio of the interior film thickness h_T to the half-width of the capillary d, and the ratio of the film thickness at the inlet to the half-width of the capillary, respectively. The number B is correspondent with the quantity $B(C)$ given by the one-to-one function of C represented by (3.6), and is thus a surrogate for the capillary number. Capillary numbers in microfluidic systems, for example, are characteristically small (e.g. Anna, 2016; Garstecki *et al.*, 2006) with $C \lesssim 10^{-2}$, for which (3.6) gives $B \lesssim 0.1$. The second dimensionless number H sets the level of confinement of the nozzle relative to the width of the capillary. The number is restricted to $0 < H < 1$, with $H \ll 1$ representing the limit of a strongly confining nozzle.

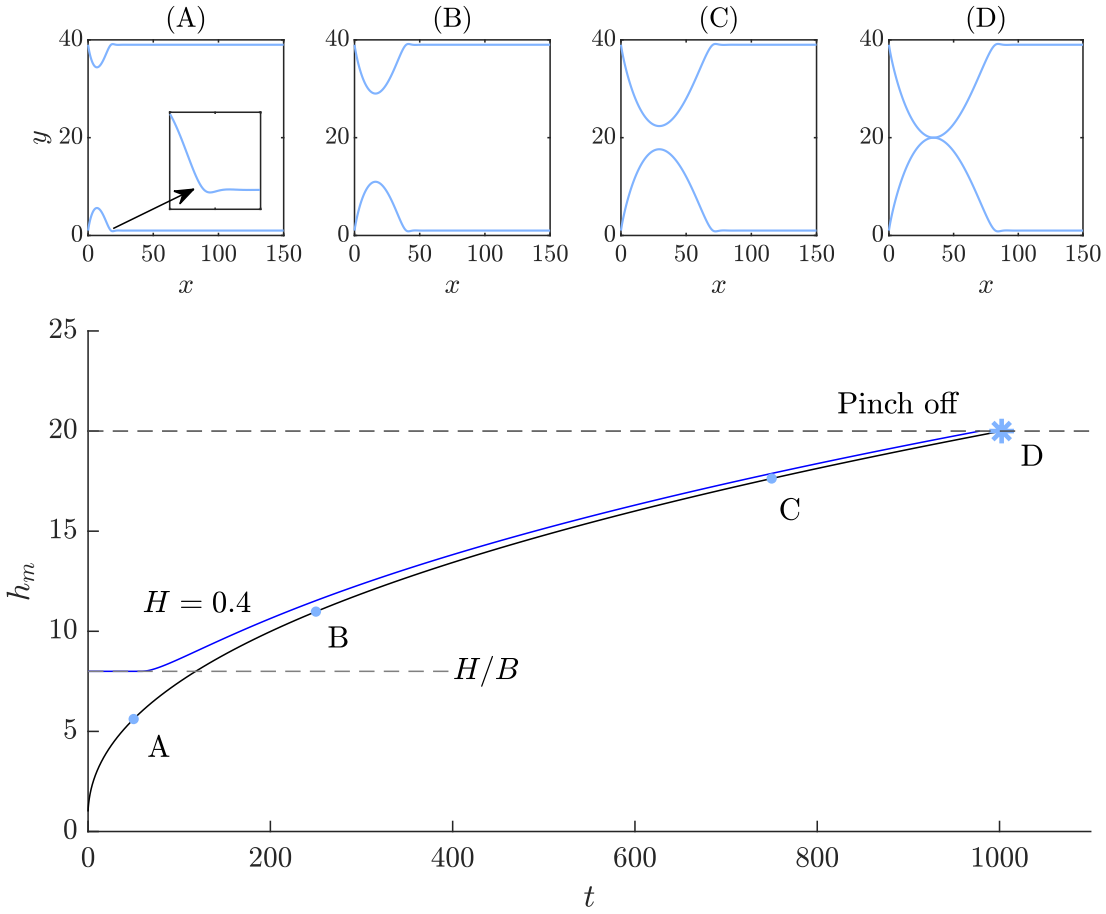

Figure 3.3: Example snapshots of the solution to the necking zone system (3.22)–(3.24) with parameters $H = 0.05$ and $B = 0.05$ are shown in (A)-(D). The corresponding maximum height of the fluid film $h_m(t)$ grows until the bubble thickness reaches zero and pinch-off occurs at a finite time t_*, as shown in panel D. The evolution of maximum film thickness are plotted for $H = 0.05$ (black) and $H = 0.4$ (blue), each with $B = 0.05$. The pinch-off time in the former is indicated by the asterisk marker. For the case $H = 0.4$, the film thickness at the nozzle H/B is indicated by a horizontal dashed line, illustrating its initial correspondence with the maximal thickness in that case.

3.2 Mathematical analysis

An illustrative solution to the system (3.22)–(3.24) is shown in figure 3.3 for $B = 0.05$ and $H = 0.05$. The solution was obtained numerically using the method

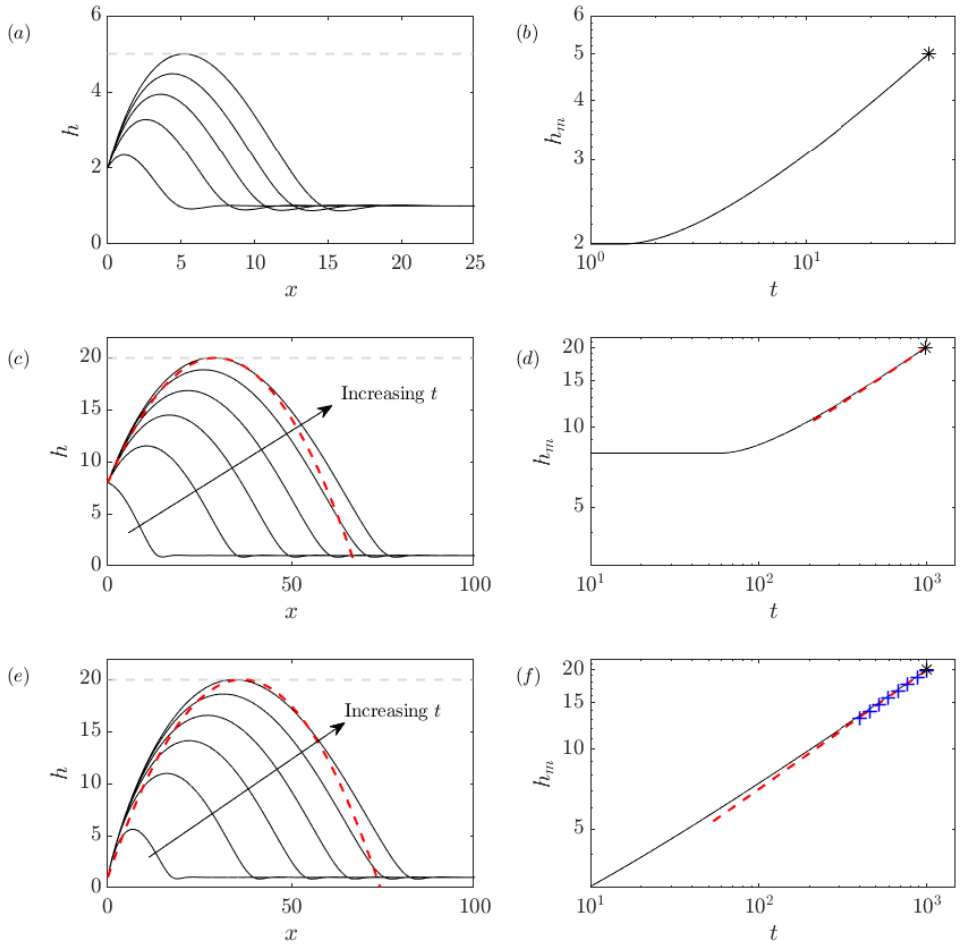

Figure 3.4: The panels on the left show the film thickness h and the final pinch-off time t_* given by the solution to (3.23) with (*a*) $B = 0.2$ and $H = 0.4$ at $t = 4, 12, 20, 28, t_* \approx 37.09$, (*c*) $B = 0.05$ and $H = 0.4$ at $t = 50, 250, 450, 650, 850, t_* \approx 978.35$, and (*e*) $B = 0.05$ and $H = 0.05$ at $t = 50, 250, 450, 650, 850, t_* \approx 1002.3$. The red dashed line represents the parabola (3.30) at final time t_*. The centreline of the channel, representing the thickness of the film at which pinch-off occur, $h_m(t_*) = 1/B$, is indicated by a horizontal dashed grey line in each case. The panels on the right plot the corresponding maximal film thickness h_m as a function of time t, showing approach to a quasi-static solution with front position given by (3.39) (red dashed). The asymptotic prediction of h_m in the small H limit (3.46) is overlayed as blue crosses in the case $H = 0.05$.

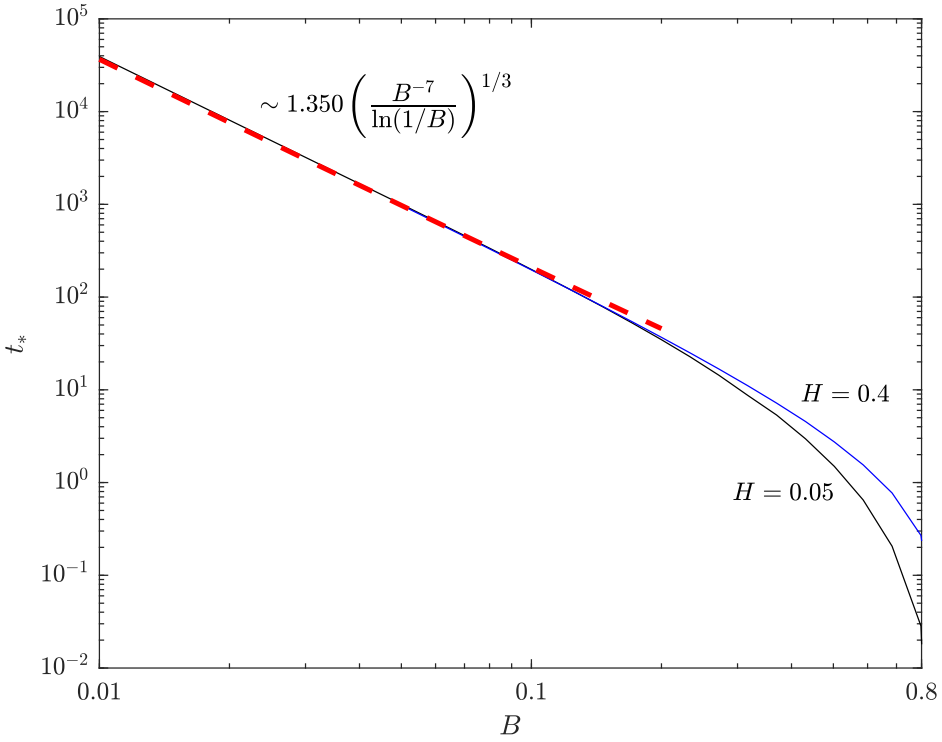

Figure 3.5: The (scaled) time taken to pinch-off $t_*(H, B)$ as a function of B for $H = 0.05$ (black) and $H = 0.4$ (blue). The dashed red line represents the asymptotic prediction (3.49) in the small B limit.

of lines, in which spatial derivatives are discretised using centred differences and time stepping is conducted using the stiff MATLAB integrator `ode15s`. The top four panels show snapshots of the interface evolution at a progression of times $t = 50, 250, 750$ up to the critical time of pinch-off, $t_* \approx 1000$, illustrating the development of a near-parabolic necking disturbance. The near-parabolic region transitions to the downstream uniform thickness relatively abruptly through a region in which the interface exhibits a small-scale spatial oscillation, shown in the zoomed inset of panel (A). The lower panel presents the evolution of the maximal film thickness $h_m(t)$, showing that it grows with a sublinear trend before attaining the pinch-off value $h_m(t_*) = 1/B$, indicated by a horizontal dashed line, at $t_* \approx 1000$. The evolutions of the maximal thickness $h_m(t)$ for $H = 0.4$ is shown in blue, exhibiting a slightly faster pinch-off time for the case of a smaller nozzle $t_* \approx 978$. The evolution of the maximum film thickness demonstrates a consistent

growth of the surrounding film until the interfaces meet at the centreline of the channel, corresponding to a point of pinch-off.

Figure 3.4 shows more illustrative solutions for the film profile, like those shown in figure 3.3, for different combinations of B and H. The ratio H/B controls the height of the fluid film at the inlet, with larger ratio corresponding to a larger film thickness and hence a more asymmetric shape of the necking region. The progression of the film profile with specified dimensionless parameters $B = 0.2$ and $H = 0.4$ is shown in panel (a) with the corresponding maximal film thickness $h_m(t)$ displayed in panel (b). The solutions connect a necking zone disturbance to a region of uniform film thickness with a small spatial oscillation at the front. The disturbance grows until the point of pinch-off $h_m(t_*) = 1/B$, represented by a grey dashed horizontal line in panel (a), and an asterisk in (b). The solutions represented in panels (c) and (d) correspond to a smaller uniform film thickness $B = 0.05$. As the value of B decreases, corresponding to a smaller capillary number, the size of the oscillation at the front of the spreading region decreases and the solution can be approximated as quasi-static. Under a quasi-static assumption, solutions adopt a parabolic shape (red, dashed). The shape of the disturbance predicted by the model is reminiscent of the shapes of droplets spreading along a precursor film (e.g. Damania & Bose, 1986; King & Bowen, 2001; Kiradjiev *et al.*, 2019), which likewise form an almost parabolic profile that transitions to a precursor film through a briefly oscillatory frontal zone. For the solutions shown in figure 3.4, the uniform thickness surrounding the Taylor bubble behaves like the precursor film. Finally, the bottom row of figure 3.4 corresponds to solutions with both input parameters taking a small value ($B = 0.05, H = 0.05$). Compared with the other film profiles, the solution in panel (e) is more symmetrical. Again, the solution can be approximated as a parabola.

To determine the function $t_*(H, B)$ for a given value of H, we begin by solving (3.22)–(3.24) numerically for the evolving interface profile $h(x, t)$. We then read off the time t_* at which $h_m(t_*) = 1/B$ for all B. The function $t_*(H, B)$, encapsulating the time to pinch-off over the entire parameter space of the necking zone theory, is shown as a function of B in figure 3.5 for two illustrative values of $H = 0.05$ and 0.4. The function t_* generally forms a decreasing function of

the film thickness B, appearing to converge to an approximately $B^{-7/3}$ asymptotic trend as $B \to 0$. At moderate values of $B \gtrsim 0.3$, we see that the effect of the nozzle–wall spacing H can significantly impact the pinch-off time by a factor of 2–3. On the other hand, for small $B \lesssim 0.1$, the pinch-off times appear to become insensitive to the nozzle-wall spacing H, with both example values of H approaching a mutual asymptote as $B \to 0$. The determination of $t_*(B, H)$, when combined with the intrinsic scales used for non-dimensionalisation (3.21), yields a general functional dependence of the pinch-off time of the Taylor bubble in the two-dimensional coflow system. The results demonstrate a simple asymptotic trend developing in the limit of $B \to 0$, indicating an asymptotic mathematical theory arising at small capillary numbers that we now seek to understand.

3.2.1 Quasi-static theory for small capillary numbers

We now develop a simplified analytical theory based on utilising an asymptotic framework of quasi-static interfacial evolution. A theoretical approach of this kind has been applied previously, in particular, in the context of droplet spreading (e.g. Hocking, 1983; Hocking & Rivers, 1982; King & Bowen, 2001; Kiradjiev *et al.*, 2019; Savva & Kalliadasis, 2009, 2011, 2013; Vellingiri *et al.*, 2011). The theory is based on a separation of the thin-film flow into two asymptotic regions: an outer region, wherein a fast diffusive time-scale maintains the interface close to the shape of a static meniscus (a parabola for two-dimensional droplets; Kiradjiev *et al.* (2019)); and an inner zone localised near a frontal *apparent* contact-line position, wherein the flow is matched to the precursor film. The outer region evolves quasi-statically in response to a slow time-scale associated with the evolution of the contact line. The leading-order equation of the outer region is the Young-Laplace equation describing a static meniscus. The inner zone instead forms a travelling-wave state (exhibiting the small spatial oscillation in the interface of the kind we see in figure 3.3A), the analysis of which yields a matching condition (the Cox-Voinov law; Cox, 1986; Voinov, 1976) on the outer region.

In the present context, we interpret the necking dynamics as a kind of forced droplet-like disturbance that spreads into an effective precursor film left by the extending Taylor bubble. As noted above, a quasi-static theory requires the

necking disturbance to grow much thicker than the precursor film. In our context, we recall that the dimensionless precursor film thickness is unity and the pinch-off criterion is $h_m(t_*) = 1/B$. Therefore, if $B \ll 1$, the necking disturbance will necessarily grow much thicker than the precursor film prior to pinch-off, with $1 \ll h_m(t) \leq 1/B$. Since H is order one, the only remaining parameter in the system is t and hence quasi-static dynamics must arise for $C \to 0$ over a 'large' temporal range $1 \ll t \leq t_*(H, B)$. Within this dominant time interval, the necking disturbance, in accordance with the proposed quasi-static theory, forms a two-zone structure: an outer quasi-static zone of approximately parabolic form; and an inner zone localised near a position $x_N(t)$ that advances in accordance with a Cox-Voinov law. We proceed to develop the quasi-static theory and validate its predictions by comparison with the predictions of the full time-dependent theory.

We begin by solving for the outer quasi-static region. Within the quasi-static framework, the flow adjusts rapidly to a near-static state with $q \ll 1$ and hence, from the expression for flux $q = \frac{1}{3}h^3 h_{xxx}$,

$$h_{xxx} \approx 0. \tag{3.27}$$

The above represents the equation describing the ultimate shape formed by relaxation under linearised surface tension, $\kappa_x = 0$; in other words, it is the linearised Young-Laplace equation describing a static two-dimensional meniscus. On the scales of the quasi-static outer region ($h \gg 1$), the precursor-film thickness is effectively vanishing to leading order,

$$h(x_N(t), t) = 0. \tag{3.28}$$

The condition at the input nozzle (3.23) gives the further boundary condition,

$$h(0, t) = H/B. \tag{3.29}$$

Integration of (3.27) subject to (3.28) and (3.29) gives us the leading-order parabolic solution

$$h(x, t) = \left(A(t)x + \frac{H}{Bx_N(t)} \right) (x_N(t) - x), \tag{3.30}$$

where $A(t)$ is a constant of integration related to the height of the parabola. Since the volume must equal t in accordance with the dimensionless input flux $q(0,t) = 1$, the interface must satisfy the volume constraint

$$\int_0^{x_N} h \, \mathrm{d}x = \frac{1}{6}A(t)x_N^3 + \frac{H}{2B}x_N = t, \tag{3.31}$$

where we have substituted (3.30) and evaluated the integral. Hence,

$$A(t) = \frac{3}{x_N(t)^3}\left(2t - \frac{Hx_N(t)}{B}\right). \tag{3.32}$$

The only remaining unknown in the quasi-static solution (3.30) is now the position of the contact line $x_N(t)$. Thus, we require a further condition for closure.

The additional condition is given by a Cox-Voinov relation that matches the quasi-static solution to the precursor film via an inner travelling-wave state at $x \approx x_N(t)$. Within the inner region, the solution transitions from its approximately linear form predicted by the outer solution (3.30) as $x \to x_N(t)$ to the downstream precursor-film thickness. A step-by-step derivation of the associated matching condition,

$$h_x^3 = -3\dot{x}_N \log(\dot{x}_N x_N^3) \qquad (x \to x_N^-(t)), \tag{3.33}$$

reviewing its development from a travelling-wave analysis of (3.22), is provided in appendix 3A. The result relates the rate of advancement of the contact line $\dot{x}_N(t)$ to the instantaneous interfacial gradient of the outer solution at the contact line $h_x(x_N, t)$. The length scale of the inner zone is $\sim (\dot{x}_N)^{-1/3}$, and hence it is necessary that $(\dot{x}_N)^{-1/3} \ll x_N$ in order for the required length-scale separation defining the asymptotic structure to apply. In other words, the argument of the natural logarithm in (3.33) is intrinsically large as part of the consistency of the theory. As $x_N(t)$ grows, the condition $(\dot{x}_N)^{-1/3} \ll x_N$ will become ever more strongly satisfied with time ($t \gg 1$), concurrently with the thickness becoming much larger than that of the precursor film, $h_m(t) \gg 1$. The control of $x_N(t)$ implied by the matching condition (3.33) is solely responsible for introducing dependences of the quasi-static evolution on the viscous and capillary parameters.

With the system now fully closed, we seek an explicit evolution equation for the contact-line position $x_N(t)$. First, we isolate the rate of change $\dot{x}_N(t)$ in (3.33)

by writing that equation in the equivalent form

$$x_N^3 \dot{x}_N = \exp\left(W\left(-\tfrac{1}{3}x_N^3 h_x^3\right)\right) \qquad (x = x_N(t)), \tag{3.34}$$

where $W(z)$ is the Lambert W-function (which, for our purposes, is sufficient to define as the unique positive root of $We^W = z$). The criterion for quasi-static scale separation $(\dot{x}_N)^{-1/3} \ll x_N$ noted below (3.33) requires both sides of the equation above to be large, and hence the argument of the W function in (3.34) is large. The large-argument form of the Lambert-W function (Abramowitz & Stegun, 1965), namely

$$W(z) \sim \log\left(\frac{z}{\log z}\right) \qquad (z \to \infty), \tag{3.35}$$

gives the leading term in $\exp(W(z)) \sim z/\log z$. Equation (3.34) thus has the leading-order form

$$\dot{x}_N \sim \frac{-h_x^3}{3\log\left(-\tfrac{1}{3}x_N^3 h_x^3\right)} \qquad (x = x_N(t)), \tag{3.36}$$

giving the leading-order rate of change of the contact line in terms of the frontal interfacial slope of the quasi-static region h_x. The frontal slope of the quasi-static parabolic solution (3.30) can be evaluated as

$$h_x(x_N, t) = -\frac{2}{x_N}\left(\frac{3t}{x_N} - \frac{H}{B}\right). \tag{3.37}$$

Substituting (3.37) into (3.36), we obtain

$$\dot{x}_N = \frac{\frac{8}{3}\left(\frac{3t}{x_N} - \frac{H}{B}\right)^3}{x_N^3 \log\left(\frac{8}{3}\left(\frac{3t}{x_N} - \frac{H}{B}\right)^3\right)}, \tag{3.38}$$

yielding the desired explicit evolution equation for $x_N(t)$. The ordinary differential equation (3.38) describes the contact-line evolution of the quasi-static regime, analogously to corresponding differential equations developed in the context of droplets, as considered in axisymmetric (Hocking, 1982; Tanner, 1979) and two-dimensional cases (King & Bowen, 2001; Kiradjiev *et al.*, 2019). A distinctive

element in the present case is the pinning of one side of the parabolic interface by the injection nozzle, which introduces terms involving the parameter H/B, and results in an advancing centre of the parabola (as opposed to symmetrical spreading at a line source). We have thus drawn a link between the asymptotic structures that can underlie injection-driven pinch-off in capillaries and those encountered in the analysis of droplet spreading.

We solve the ordinary differential equation (3.38) numerically subject to an initial condition on $x_N(t_0)$, where $t_0 \gg 1$, as required for solutions in the quasi-static regime. The quasi-static states have an attractor to which the solutions converge over a time scale of order unity, and so the late time regime is largely unaffected by the initial condition. Hence, the initial value of time and position of the front are chosen to minimise the transition to the attractor, and also so that the argument of the W-function is large enough for the scale separation necessary for the quasi-static theory to develop.

With $x_N(t)$ determined, the parabolic profile (3.30) can be evaluated to give a prediction for the evolution of the interface, with pinch-off occurring once $h_m(t_*) = 1/B$, where

$$h_m(t) = \frac{\left(3t - \dfrac{Hx_N(t)}{B}\right)^2}{3x_N(t)\left(2t - \dfrac{Hx_N(t)}{B}\right)} \tag{3.39}$$

is the maximum of the parabola. The prediction of the quasi-static theory is overlayed in panels (c) to (f) of figure 3.4. The left-hand panels show the interface evolution at the pinch-off time where the quasi-static prediction is overlaid as a red dashed line, showing good agreement with the numerical prediction of the time-dependent necking zone model. The evolution of the maximal thickness (3.39) is overlaid in the right-hand panels as a red dashed line, showing excellent agreement with the numerical predictions of the full necking-zone theory (3.22)–(3.24) over the dominant time scale, $1 \ll t \leq t_*$, thus validating the quasi-static regime.

3.2.2 Asymptotic solution to the quasi-static theory for $H \ll 1$

For $H \ll 1$, the spacing between the nozzle and the sidewall is small relative to the size of the capillary. In this limit, the thickness of the film near the input nozzle can, similarly to the contact-line position (3.28), be approximated as zero on the scales of the outer quasi-static region, for all times up to pinch-off ($h(0,t) = H/B \ll 1/B$). As a result, the parabola is approximately symmetric (cf. figure 3.4, where $H = 0.05$), with a line of symmetry residing close to $x_N(t)/2$. The solution thereby retains a self-similar interfacial shape, a simplification which allows for a yet further analytical prediction within the quasi-static theory.

The implication of $H \ll 1$ within the quasi-static theory is that we can neglect the H term in the governing differential equation (3.36), reducing it to the parameterless equation

$$\dot{x}_N \sim \frac{72t^3}{x_N^6 \log(72t^3/x_N^3)}. \tag{3.40}$$

We seek a leading-order asymptotic solution to (3.40) during the quasi-static regime ($1 \ll t \leq t_*$). To derive this, we try the ansatz of the form

$$x_N(t) \sim f(t)t^\alpha \qquad (t \gg 1), \tag{3.41}$$

where α is an unknown constant to be determined and $f(t)$ is an unknown function with the property that $\log(f(t)) \ll \log t$ for $t \gg 1$ (in other words, $f(t)$ is assumed to be at most of logarithmic order in t or a power thereof). Substitution of (3.41) into (3.40) yields, on neglect of higher-order terms in $t \gg 1$,

$$\frac{504t^3}{3(1-\alpha)\log t} = \frac{\mathrm{d}}{\mathrm{d}t}(x_N^7). \tag{3.42}$$

Integrating, and using a change of variable in the integral $z = 4\log t$, we obtain

$$\frac{504}{3(1-\alpha)} E(4\log t) = x_N^7, \tag{3.43}$$

where $E(z) \equiv \int_\infty^z z^{-1}e^z \,\mathrm{d}z$ is the exponential integral function, and we have set the constant of integration to zero in order to satisfy the early-time asymptotic condition $x_N \to 0$ as $t \to 0$. With use of the large-argument asymptote of the

exponential integral function $E(z) \sim e^z/z$ as $z \to \infty$ (Abramowitz & Stegun, 1965), (3.43) reduces to

$$\frac{42t^4}{(1-\alpha)\log t} = x_N^7, \tag{3.44}$$

in the relevant limit $t \gg 1$. Comparing the equation above with the ansatz (3.41), we see that $\alpha = 4/7$ is necessary for consistency, and $f(t) = (98/\log t)^{1/7}$. Then, since $\log(f(t)) = O(\log(\log t))$, the derived function $f(t)$ satisfies the required asymptotic property stipulated in our ansatz (3.41) that $\log(f(t)) \ll \log t$, confirming the asymptotic consistency of the derivation. We conclude that the leading position of the contact line evolves as

$$x_N \sim \left(\frac{98t^4}{\log t}\right)^{1/7} \qquad (1 \ll t \leq 1/B). \tag{3.45}$$

The result of (3.45) indicates a dominant $x_N \sim t^{4/7}/(\log t)^{1/7}$ growth of the front of the pinch-off disturbance within the necking zone for small B. The corresponding prediction of the maximum of the parabolic profile (3.30), occurring at $x = x_N(t)/2$, is, with (3.45),

$$h_m(t) \sim \frac{3}{2}\left(\frac{t^3 \log t}{98}\right)^{1/7}. \tag{3.46}$$

The above is overlaid in figure 3.4(f) as blue crosses in the example with $B = 0.05$ and $H = 0.05$, showing excellent agreement with both the numerical prediction of the full necking-zone theory (3.22)–(3.24) in the limit of large t, and the prediction of the quasi-static theory represented by (3.39) with the solution for $x_N(t)$ given by the solution to the differential equation (3.38).

A $t^{4/7}$ power component was also obtained for the contact-line position in the late-time regime of the related problem of injection-driven spreading of a two-dimensional droplet along a precursor film, based on treating the logarithmic term in (3.40) as a constant (Kiradjiev *et al.*, 2019). Our analysis indicates that, for the context of a necking disturbance, the additional slowly-varying $\log t$ factor we derive in (3.45) is necessary for a consistent leading-order solution encompassing times up to the time of pinch-off, $1 \ll t \leq t_*(B)$.

To determine the pinch-off time, we substitute (3.46) into the pinch-off criterion $h_m(t_*) = 1/B$ giving

$$t_*^3 \log(t_*^3) = a\, B^{-7}, \tag{3.47}$$

where $a = (112/27)^2$ is a numerical constant. Hence,

$$t_* = \exp\left(\tfrac{1}{3}W(aB^{-7})\right). \tag{3.48}$$

Since $B \ll 1$, we can simplify the above using (3.35) to give the final result,

$$t_* \sim \left(\frac{aB^{-7}}{\log(aB^{-7})}\right)^{1/3} \sim 1.350\left(\frac{B^{-7}}{\log(1/B)}\right)^{1/3}, \tag{3.49}$$

providing an explicit asymptotic prediction for the pinch-off time t_*. The prediction is overlaid as a dashed red curve in figure 3.5, showing excellent agreement with the pinch-off time predicted by the numerical solution to the full necking-zone theory of (3.22)–(3.24) in the relevant limit of $B \to 0$. Despite being a theory based on $H \ll 1$ (as otherwise the asymmetry of the parabola precludes a simple analytical solution of the form (3.41)), the prediction captures the $B \to 0$ trend for cases of both $H = 0.05$ and 0.4. The result of (3.49) implies that $t_* \gg 1$ as $B \to 0$ and thus self-consistently predicts the existence of the large asymptotic time interval wherein the quasi-static regime occurs ($1 \ll t \leq t_*(B)$).

3.2.3 Conditions for asymptotic self-consistency of the necking-zone model

The original theory of the necking zone (3.22)–(3.24) was based on two underlying asymptotic modelling assumptions: one, that lubrication theory applies to leading-order in the necking zone; and second, that a long (Taylor) bubble forms. We now consider the parametric conditions under which these conditions hold, thereby assessing the asymptotic self-consistency of the model predictions.

Beginning with the lubrication approximation (3.9), we note that, in our non-dimensional variables, the condition of small interfacial slopes takes the form

$$|h_x| \lesssim \varepsilon\left(\frac{B}{QC}\right)^{1/3}, \tag{3.50}$$

where $\varepsilon \ll 1$ is a small dimensionless parameter charactering the size of the aspect ratio (representing the tolerance of the approximation), and $Q = q_c/q_d$ is

the ratio of the film flux to the bubble flux. Thus, the aspect ratio of the necking disturbance at the time of pinch-off is characterised by

$$h_x \sim \frac{h_m(t_*)}{x_N(t_*)} \sim 0.50\ (B\log(1/B))^{1/3}, \tag{3.51}$$

upon using $h_m(t_*) = 1/B$ and

$$x_N(t_*) = 2.0\left(\frac{1}{B^4\log(1/B)}\right)^{1/3}, \tag{3.52}$$

obtained by substituting the pinch-off time (3.49) into (3.45). Equating (3.50) and (3.51), and simplifying, we obtain the constraint on Q and C given by

$$QC\log(1/C) \lesssim 12\,\varepsilon^3. \tag{3.53}$$

If the criterion above holds then the model prediction is self-consistent with maintaining lubrication theory. The product $QC \equiv \mu q_c/\gamma d$ can be interpreted as an alternative capillary number derived from the injection flux of the viscous phase (as opposed to the bubble flux used to define C). The result indicates that the film capillary number QC is the primary control in determining the self-consistency of lubrication theory. This finding is consistent with the fact that, similarly to a droplet driven by injection (e.g. Kiradjiev *et al.*, 2019), larger injection fluxes feeding the necking disturbance will cause it to thicken relatively faster than it spreads longitudinally, yielding steeper aspect ratios. There is a weak logarithmic dependence on C stemming from its role in controlling the precursor film thickness and, in turn, the spreading rate via the Cox-Voinov law. The constraint above restricts the region of validity of the model predictions in the parameter space (C, Q) below the locus plotted as a dashed curve in figure 3.6 for the illustrative value $\varepsilon = 0.2$, showing that lubrication theory necessarily breaks down if the product of Q and C is sufficiently large.

Second, we examine the self-consistency of the Taylor-bubble regime, defined by the property that the cap of the Taylor bubble extends further downstream than the characteristic size of the necking disturbance (3.2), namely,

$$x_N(t_*) \ll x_F(t_*). \tag{3.54}$$

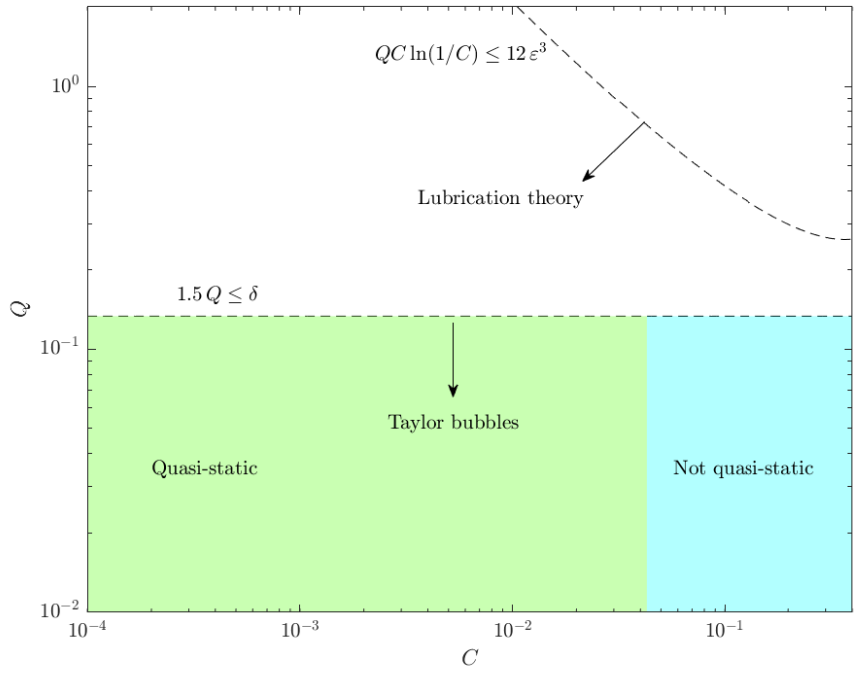

Figure 3.6: The C–Q parameter space partitioned by the characteristic regions in which the two asymptotic assumptions of the model (3.53) and (3.55) hold self-consistently (blue shading). Within this region of model self-consistency, there exists a small-C limiting sub-regime where the solution is approximately quasi-static (green shading).

Using the dimensionless form of the prediction for the characteristic length of the Taylor bubble given below (3.8), namely $x_F \sim Bt/Q$, and (3.52), we find that, after some simplification, the ratio reduces to

$$\frac{x_N(t_*)}{x_F(t_*)} \sim 1.5\,Q \lesssim \delta, \tag{3.55}$$

where $\delta \ll 1$ is a parameter representing the tolerance. Thus, it is indicated that the characteristic length of the bubble to the length of the necking disturbance is controlled independently by the flux ratio Q. For $\delta = 0.2$, the above yields $Q \lesssim 0.1$, indicating that well defined Taylor bubbles are formed if the bubble flux is less than one tenth the flux of the viscous fluid. The condition is indicated by

a horizontal dashed line on figure 3.6.

The region of (C, Q) space in which the Taylor bubble assumption (3.55) is self-consistent is entirely subsumed by the condition where lubrication theory (3.53) is self-consistent. Since the self-consistency of the model requires both of these conditions to be satisfied, we conclude that, for tolerances of $\varepsilon = \delta = 0.2$, model self-consistency (represented by the coloured region) occurs sufficiently on the basis of the Taylor-bubble condition alone. A decrease in tolerances moves the dashed lines representing validity of each condition closer together, with the conclusion that they remain separate holding for tolerances of $\varepsilon \sim \delta \sim 0.1$. For yet smaller tolerances, some overlap between the constraints of (3.53) and (3.55) is possible, with the lubrication constraint introducing some restriction on the flux ratio at moderate capillary numbers. The subregion highlighted in green on the parameter space (figure 3.6) defines where the thin-film asymptotic limit of the pinch-off time (3.49) is within 20% of the pinch-off time predicted by the necking zone model (3.22)–(3.24) with $H = 0.05$. Thus, for characteristic values of $C \lesssim 0.04$, the analytical quasi-static theory (section 3.2.1) applies to good approximation.

3.3 Summary and discussion

Our analysis has developed a progression of models at three levels of asymptotic reduction. The first comprised the full model of the necking zone (section 3.1.2) formed by coupling the standard lubrication equations to nozzle conditions and a downstream condition connecting the interface to the interior thickness of the Taylor bubble (3.22)–(3.24). Solutions to this first model can be classified based on the dimensionless Taylor-bubble film thickness B and nozzle–wall spacing H. The second level, arising for small $B \ll 1$ (equivalently, small capillary number, $C \ll 1$), forms a quasi-static theory defined by the outer region retaining a shape that is effectively instantaneously given by that of a static meniscus, and evolves in response to a slow time-scale associated with the advance of an effective dynamic contact line, $x_N(t)$, governed by a Cox-Voinov law. The regime is represented by the ordinary differential equation for the evolution of the contact line (3.38). The

third level of simplification is the asymptotic solution (3.45) within the quasi-static theory that applies strictly in the limiting case where the nozzle thickness is tightly fitting ($H \ll 1$). In this case, the self-similar propagation allows for a simple analytical form of the solution to the quasi-static theory over the time scales on which the quasi-static theory applies up to pinch-off. The result yields an analytical law for the time of pinch-off (3.49) that accurately captures the predictions of the original necking model in the relevant limit of small capillary number (equivalently, $B \to 0$; figure 3.5). Despite being derived on the basis of a tightly confining nozzle ($H \ll 1$), the result appears to capture the leading-order pinch-off time for general H.

We redimensionalise the results in order to see the parametric dependences of the predictions explicitly. Henceforth, variables will represent their dimensional versions, with non-dimensional variables indicated by hats. The general predictions of the full necking-zone theory (section 3.1.2) can be expressed as

$$t_* = \hat{t}_* \left(H, B(C)\right) \left(\frac{\gamma h_T^7}{\mu q_c^4}\right)^{1/3}, \tag{3.56}$$

where $B(C)$ is the parameterless dimensionless function of the bubble capillary number $C \equiv \mu q_d / \gamma d$ reviewed in figure 3.2, $h_T = B(C)d$ is the interior thickness of the Taylor bubble given generally by (3.5), and $\hat{t}_*(H, B)$ is the numerically determined dimensionless solution for pinch-off times shown in figure 3.5. Since neither H nor $B(C)$ depend on the flux of the film q_c, we note that the simple inverse 4/3 power-law scaling dependence in (3.56) on the viscous fluid flux q_c is a universal dependence of the pinch-off time.

For capillary numbers $C \lesssim 0.01$, we derived an explicit theoretical prediction for the pinch-off time (3.49), which takes the dimensional form

$$t_* = 1.545 \left(\frac{\gamma d^7}{\mu q_c^4 \log\left(1/C\right)}\right)^{1/3}. \tag{3.57}$$

The result predicts that the time to bubble pinch-off is controlled by an inverse proportionality to the 4/3 power of the input flux of the viscous fluid q_c, a 1/3 power of the ratio of the surface tension to the fluid viscosity γ/μ, and a 7/3 power of the channel size d. The prediction includes a weak logarithmic dependence of the pinch-off time on the bubble flux q_d contained in the capillary number C.

Finally, we note that the maximal size of the necking disturbance, as represented by $x_N(t_*)$ and non-dimensionally by the prediction of (3.52), is

$$x_N(t_*) \sim 2.3 \left(\frac{\gamma d^4}{\mu q_c \log(1/C)} \right)^{1/3}. \tag{3.58}$$

The result shows that the maximal length of the necking disturbance is controlled by a 4/3 power of the channel size d, a 1/3 power of the ratio of the surface tension to the fluid viscosity γ/μ, and an inverse proportionality to the 1/3 power of the input flux of the viscous ambient phase q_c. Thus, the length of the necking zone is primarily controlled by the width of the channel. Similarly to (3.57), there is a very weak logarithmic dependence of the maximal length of the necking zone on the bubble flux q_d contained in the capillary number C.

3.3.1 Model limitations

The theory provided in this chapter provides asymptotically self-consistent regimes with corresponding analytical predictions for bubble pinch-off time. Whilst the asymptotic consistency of the model has been rigorously clarified (section 3.2.3), the model is limited to predict the time to pinch-off of Taylor bubbles only. If we were to consider larger flux ratios, the solutions would sit outside of the Taylor-bubble regime as demonstrated in figure 3.6. Hence, the flow structure upon which the model presented in this chapter is based would no longer exist and the downstream Taylor bubble regime would need to be replaced with bubble shape that includes nose condition.

Additionally, the model is limited to describe the process up to Taylor bubble pinch-off as the linearised curvature expression cannot capture the immediate dynamics in regions of infinite gradients. Immediately after bubble pinch-off, the newly detached interfaces at both the rear of the newly formed bubble, and at the nose of the remnant of thread attached to the input nozzle, will both exhibit infinitely steep gradients. Hence, solutions (like the one shown in figure 3.3) are valid up until the point of pinch-off, but lubrication theory cannot necessarily fully capture the dynamics immediately after pinch-off, for which full nonlinear curvature and Stokes flow may be required.

We acknowledge that the analysis presented in this work is restricted to the planar coflow geometry. Extension of this analysis to the axisymmetric geometry would be of interest, and added complications relating to the breakdown of quasi-static solutions would be introduced (e.g. Collicott *et al.*, 2006; De Gennes *et al.*, 2003; Lv & Hardt, 2021; Slobozhanin *et al.*, 1999). The planar geometry acts as a key first step inroad to the application of corresponding mathematical analysis to these more complex situation, and is an asymptotic limit of the axisymmetric geometry for shallow and short necking disturbances. Hence, the two dimensional geometry is a necessary foundation for the more complicated axisymmetric geometry, and serves as a preliminary step towards developing a corresponding theoretical new principles in the axisymmetric context, which will be the focus of chapter 5.

For an interesting extension of the work presented in this chapter, one could relax the incompressibility assumption of the model in order to consider problems requiring dynamic pressures.

3.3.2 Discussion and comparisons

Cubaud *et al.* (2005) provide an experimental exploration into the length of gaseous Taylor bubbles generated at the right-angle intersection of four identical microchannels of square cross section. Using the experimental data, a simple scaling law is derived which relates the length of the Taylor bubbles to the ratio of the channel width to the liquid volumetric fraction $\alpha_L = q_c/(q_c + q_d)$. The scaling law is shown to be consistent with experimental results in a T-junction formed by channels of rectangular cross-section (Garstecki *et al.*, 2006) and numerical results in a flow-focusing geometry (Jensen *et al.*, 2006). The scaling is also validated in the coflow geometry by Xiong *et al.* (2007), who uses an experimental particle image velocimetry (PIV) system to provide a visual depiction of the interface with time, with the interface appearing approximately parabolic near to the nozzle (figure 7d of Xiong *et al.* (2007)), consistent with the predictions of our necking zone theory in section 3.1.2. Assuming the Taylor bubble takes an approximately cylindrical shape, the scaling law proposed by Cubaud *et al.* (2005) is analogous to a prediction of pinch-off time given by $t_* \propto 1/q_c$.

This scaling for pinch-off time is consistent with the experimental investigation performed by Salman *et al.* (2006) into the coaxial injection of air into a small cylindrical channel filled with water at a constant flux forming Taylor bubbles. They record the progression of the air-water interface with a high-speed camera and, from photographic observations, conclude that the frequency of bubble production increases with the flux of either fluid phase. They also conclude that the period of bubble formation exhibits only a weak dependence on the surface tension of the outer liquid, and is determined predominantly by the nozzle size and flow rates.

Whilst the predictions for pinch-off time given by Garstecki *et al.* (2006) and Salman *et al.* (2006) are qualitatively consistent the findings of this chapter (t_* is predominantly controlled by an inverse relation to $q_c^{4/3}$), the geometries are not exactly equivalent. New considerations attributed to additional azimuthal curvature terms lead to more complicated static shapes given by solutions of the Young–Laplace equation for the liquid annulus in a cylindrical capillary (e.g. Collicott *et al.*, 2006; Everett & Haynes, 1972; Lv & Hardt, 2021; Slobozhanin *et al.*, 1999) and changes in scaling due to volume of revolution considerations will change the predictions for pinch-off time presented in this chapter when considered in an axisymmetric geometry. More detailed mathematical analysis is required to explain the experimentally observed scaling laws and we hypothesis that the quasi-static analysis outlined in section 3.2 could be applied to the axisymmetric configuration to provide an equivalent theoretical prediction for Taylor bubble pinch-off times

3.4 Conclusions

The work presented in this chapter provides three primary developments. First, we formulated a simple necking zone theory with a downstream matching to Taylor bubble thickness that is asymptotically consistent with a classical linearised curvature lubrication approach, and hence a rigorous asymptotic theory of the full-Stokes problem. Second, we introduced principles of quasi-static modelling and matching to the dynamics contact line to the problem of forced capillary

pinch-off, which explicitly predicts the key time scale of bubble pinch-off and reveals a link between droplet dynamics and pinch-off dynamics. Third, we used this framework to develop an explicit theoretical prediction for pinch-off time, applicable to small capillary numbers:

$$t_* = 1.545 \left(\frac{\gamma d^7}{\mu q_c^4 \log\left(1/C\right)} \right)^{1/3}, \tag{3.59}$$

yielding the first theoretically derived result for injection-driven pinch-off in a capillary system, demonstrating from first principles its key parametric control. The result shows that the time to bubble pinch-off exhibits a $q_c^{-4/3}$ power law dependence on the flux of the liquid phase, but is almost independent of the flux of the bubble phase, with only a logarithmic dependence contained within the capillary number C. The prediction also reveals a $d^{-7/3}$ power law dependence on the half-width of the geometry, and a $(\mu/\gamma)^{1/3}$ power dependence on the ratio of the liquid viscosity to the surface tension coefficient.

The analysis of this chapter has focused on the two-dimensional flow of a Newtonian, inviscid bubble within a straight-walled channel of uniform width. The framework presented here provides a foundation for application of quasi-static analysis to an axisymmetric geometry, or to configurations where the inviscid bubble is replaced with a fluid of non-zero viscosity or a non-Newtonian fluid. Each of these presents an interesting direction for future development, for which the analysis of the present chapter provides a foundation.

Appendix 3A. Matching condition on the dynamic contact line

This appendix reviews the derivation of the Cox-Voinov law (Bonn *et al.*, 2009; Cox, 1986; Voinov, 1976) for the specific case of matching a lubrication flow to a much thinner precursor film (3.33). This limiting case of the law (effectively the case of zero contact angle) has been used, for example, in studies of droplet spreading along a precursor film (e.g. King & Bowen, 2001; Kiradjiev *et al.*, 2019). The condition arises from considering an inner region near the apparent contact line, $x \approx x_N(t)$, wherein the interface takes a universal form that connects

an upstream quasi-static region to a uniform precursor film ahead of the contact line. The region is distinguished compared to the outer quasi-static region (section 3.2.1), by requiring the full governing lubrication equation (3.22) but is simplified by forming a steady travelling wave state in the frame of the contact line.

To derive the inner equation, we first move into the frame of the contact line by defining the moving and scaled coordinate $x = x_N(t) + s(t)\zeta$, where $s(t)$ represents the size of the inner zone (to be specified). In terms of the inner coordinate ζ, the governing equation (3.22) becomes

$$h_t - \frac{\dot{x}_N}{s(t)} h_\zeta = \frac{-1}{3s(t)^4} \left(h^3 h_{\zeta\zeta\zeta}\right)_\zeta . \tag{3.60}$$

Setting $s(t) = (\dot{x}_N)^{-1/3}$ to ensure a balance between both sides of the equation and seeking a travelling-wave state, we obtain the leading-order inner equation

$$-h_\zeta = -\tfrac{1}{3}(h^3 h_{\zeta\zeta\zeta})_\zeta. \tag{3.61}$$

The equation has a first integral which, subject to the downstream condition $\lim_{\zeta\to\infty} h = 1$, is given by

$$h - 1 = \tfrac{1}{3} h^3 h_{\zeta\zeta\zeta}, \tag{3.62}$$

forming the Landau-Levich equation. For the purpose of obtaining a matching condition on the quasi-static outer solution, we are interested specifically in the asymptotic form of the solution to the equation above in the outer limit $\zeta \to -\infty$.

In the outer limit, $\zeta \to -\infty$, it is necessary that $h \to \infty$ in this inner zone in order to match to the much larger thickness scales in the outer quasi-static region ($h \gg 1$). In the matching zone, (3.62) therefore simplifies to

$$h^2 h_{\zeta\zeta\zeta} \sim 3. \tag{3.63}$$

If we were to seek a power-law solution to the equation above based on scaling, we would require $h \propto -\zeta$. However, this form would imply that the derivative $h_{\zeta\zeta\zeta}$ is identically zero, which does not allow for a consistent balance in (3.63). In such a situation, we must try the generalised ansatz that includes a logarithmic power law given by

$$h \sim -k\zeta \log(-\zeta)^\alpha \qquad (\zeta \to -\infty), \tag{3.64}$$

where α and k are constants to be determined. Substitution of the above into (3.63) gives

$$-k^3\big(-\alpha\log^{3\alpha-1}(-\zeta)+\alpha(\alpha-2)(\alpha-1)\log^{3\alpha-3}(-\zeta)\big)\sim 3. \tag{3.65}$$

The second term above contains a smaller logarithmic power ($3\alpha-1>3\alpha-3$) and hence can be neglected compared to the first term for $\zeta\to-\infty$. Comparing the left- and right-hand sides of the remaining expression, we note that we require $\alpha=1/3$ and $k=9^{1/3}$ for a consistent leading-order balance. In conclusion, the solution to (3.62) has a leading-order upstream form

$$h\sim-\zeta\left(9\log(-\zeta)\right)^{1/3}\qquad(\zeta\to-\infty). \tag{3.66}$$

Differentiating (3.66) and neglecting higher-order terms as $\zeta\to-\infty$, we obtain

$$h_\zeta\sim-\left(9\log(-\zeta)\right)^{1/3}\qquad(\zeta\to-\infty), \tag{3.67}$$

recovering the Cox-Voinov expression for zero contact angle. Recasting the above in terms of our original dimensionless variables, we obtain (3.33).

Chapter 4

A nonlinear curvature model for oscillatory bubble formation

Whilst the model framework presented in chapter 3 is able to capture the dynamics of a single Taylor bubble prior to pinch-off, it is unable to predict the oscillatory pinch-off cycle that results in a train of bubbles produced at regular intervals. Before pinch-off, the interfacial gradient of the fluid-fluid boundary remains small except for the regions near the bubble tip and in the necking region. The gradient at the nose of the bubble is infinite and hence lubrication theory cannot apply there. As we approach the nose of the bubble, the gradient of the interface increases and, in particular, the full nonlinear curvature expression as well as the inclusion of full Stokes effects are required in order to ensure sufficient accuracy. In order to address the question of what happens after the pinch-off of a Taylor bubble, we present a generalised model framework based upon lubrication theory with retention of nonlinear curvature to allow for the possibility to solve for the complete pinch-off cycle.

A common mathematical approach in the modelling of curved liquid jets is to assume a slender-jet (or long-wave) approximation whereby the length of the jet is much greater than its radius. Under this approximation, the Navier-Stokes equations reduce to a one-dimensional model for the jet shape that is significantly cheaper to solve numerically (Brenner *et al.*, 1997; Eggers, 1997; Eggers & Dupont, 1994). Eggers & Dupont (1994) develops a slender-jet model to describe the breakup of a viscous jet. The exact nonlinear curvature expression is used,

despite the fact that the retention of nonlinear curvature violates the assumptions of the formal model derivation, as the higher-order terms are shown to be important when representing regions of high interfacial gradient. Whilst the nonlinear curvature model is inconsistent with the long-wave approximation, it is shown to increase the accuracy of one-dimensional analyses and exhibit better agreement with experimental results by a number of other researchers (Ambravaneswaran *et al.*, 2002; Brenner *et al.*, 1997; Johnson *et al.*, 1991; Kheshgi, 1989; Zhang *et al.*, 1996). Eggers & Dupont (1994) compares model results to experimental observations given by Peregrine *et al.* (1990) for drop formation from a dripping tap by overlaying a time series of numerical simulations onto a photograph taken by Peregrine *et al.* (1990) at the point of breakup. The model can successfully reproduce experiments where the profile is not slender and represents the large gradients at the front of the droplet well. However, the numerical simulations can only be compared with experimental results up until the formation of a singularity when the radius of the fluid column becomes zero. Although the equations governing the jet dynamics are fundamentally different from the shear-dominated lubrication framework, the success of the model framework combining a long-wavelength model with inconsistent nonlinear curvature expression provides motivation for the framework presented in this chapter.

Snoeijer (2006) proposes a modified lubrication theory for free-surface flows at low Reynolds number that includes a correction factor for viscous effects and retains the full nonlinear curvature expression. The flow in a wedge with a slowly varying, finite opening angle $\theta(x)$ is considered, which naturally arises in free-surface flows with moving contact lines. By expanding about Stokes flow in a wedge, they present a long-wavelength theory that remains fully quantitative for steep interface slopes at low capillary numbers. The model has the same mathematical structure as the standard lubrication approximation, but remains exact for steady flows with interfacial slopes of $O(1)$ under the condition $\partial_x\theta \ll 1/h$. Snoeijer (2006) demonstrates that the long-wavelength theory is able to successfully recover the asymptotics of Voinov (1976) and Cox (1986). Their results provide an illustration that nonlinear curvature contributions become important when interfacial gradients are large, but the analysis is completed in the context of moving contact lines rather than bubble pinch-off.

As we showed in section 3.2.3 in the context of a two-dimensional planar geometry, the standard lubrication theory is consistent for small interfacial slopes $h_x \ll 1$. In this chapter, we shall derive a nonlinear curvature model that retains the full expression for curvature and includes a description of the progression of the bubble front (giving solutions for the entire bubble, rather than just the necking zone region). While the necking zone theory is asymptotically consistent with a classical lubrication with linearised curvature, and hence a rigorous asymptotic theory of the full Stokes problem, the nonlinear time-dependent framework presented in this section serves as an analytical tool to predict the interface shape of a full bubble, providing more information than the necking theory alone, though formally inconsistent with the lubrication approximation (which is based on a small slope approximation). The nonlinear curvature model can be considered as an intermediate model: the full Stokes can be considered as the 'exact' problem and the lubrication model is the fully simplified model in the case of small interfacial gradients. By retaining the full nonlinear curvature expression, the restriction on the gradient of the interface can be relaxed and the resulting more general lubrication equation allows for a model that can accommodate arbitrary slopes.

Ratulowski & Chang (1989) presents a similar model incorporating the full nonlinear curvature expression into the lubrication framework for a steady, isolated, elongated bubble. Rather than assuming a hemi-spherical front as in Bretherton, they derive a travelling wave formulation of the lubrication model that retains nonlinear curvature of the interface at the bubble front. The framework focuses on the steady state, providing predictions of the wetting film thickness for isolated bubbles, and does not allow for time-dependent phenomena such as bubble pinch-off. The model is shown to follow the Bretherton prediction in the small capillary number limit, as well as exhibiting good agreement with numerical solutions of Reinelt & Saffman (1985) for capillary numbers up to $C \approx 0.1$. The results suggest that, despite being an inconsistent model, the model is valid and offers an improved prediction of the uniform film thickness when compared with the asymptotic result derived by Bretherton (1961). However, for larger capillary numbers, the model solutions deviate from the experimental and numerical

results, which we can anticipate is due to full-Stokes effects associated with non-shear viscous stresses becoming important in resisting flow around the front of the bubble.

Lu *et al.* (2023) provide an experimental investigation into the gas–liquid displacement driven by an input pressure within a tapered capillary tube. They briefly consider a one-dimensional time-dependent equation for the bubble interface within a lubrication framework, and present numerical solutions to the unsteady lubrication equation to show the evolution of the fluid-fluid interface until the point of pinch-off. Motivated by the slow-moving bubble front observed in their experiments, the authors choose to fix the front of the bubble so as to avoid solving for this moving boundary, and also terminate the interface early to avoid the infinite slope near the nose. The numerical solutions are shown to recover the experimentally observed bubble diameters reasonably well across a range of input pressures. The model presented in this chapter differs from the work of Lu *et al.* (2023) as we include a kinematic boundary condition that allows for motion of the bubble nose. Additionally, the nonlinear curvature model presented herein is able to produce trains of bubbles by specifying a remnant of the previous rupture as an initial condition for the system, whereas the numerical simulations presented by Lu *et al.* (2023) finish at the point of bubble pinch off.

Whilst there exist many numerical (e.g. Chatterjee *et al.*, 2021; Martinez & Udell, 1989; Reinelt & Saffman, 1985; Taha & Cui, 2006) and experimental (e.g. Dietrich *et al.*, 2013; Thulasidas *et al.*, 1997; Zaloha *et al.*, 2012) investigations into the formation of Taylor bubbles, there is relatively little detailed theoretical work on modelling the fundamental pinch-off dynamics of Taylor bubbles in confined channels or pipes. In this chapter, we present a generalised time-dependent model that uses a lubrication theory of the viscous film while retaining a nonlinear description of the interfacial curvature. The model presents a compromise between simplifying the fluid mechanics to the key resistive stresses due to shear, and the flexibility to allow for complex interfacial shapes and time-dependent dynamics described by a relatively simple nonlinear hyperdiffusion equation. The work presented in this chapter is motivated two-fold. Firstly, the main objective of this chapter is to provide validation of the predictions for bubble pinch-off time derived previously in chapter 3 (where here we account for the full, periodic

cycle of bubble formation). We demonstrate the model in the context of two-dimensional coflow, and show that the framework is able to capture the necking evolution that depends inherently on time-dependent interfacial dynamics and nonlinear descriptions of curvature. Secondly, we investigate the formation of shorter, non-Taylor bubbles.

4.1 Model formulation

We shall present the nonlinear curvature model for the full bubble in the same planar coflow configuration considered previously (figure 3.1). The configuration of *coflow* is defined by the injection of an inviscid fluid at a constant volumetric flux per unit width q_d at a nozzle that lies at $x = 0$ and is centred inside the channel. We consider here the simplest case where the channel is of uniform width d and filled with a viscous fluid injected at a constant volumetric flux per unit width q_c. Defining the height of the film at the input as $h(0,t) = h_0$, the width of the input nozzle is $2(d - h_0)$.

Recall the governing equation derived in section 3.1.2,

$$h_t = -\frac{\gamma}{3\mu}\left(h^3\kappa_x\right)_x, \qquad \kappa = \frac{h_{xx}}{(1+h_x^2)^{3/2}}, \tag{4.1}$$

where here we have retained the generalised curvature expression κ, rather than using the simplification $\kappa \approx h_{xx}$. We note that this is a difference between the models, and acknowledge that retention of the nonlinear curvature leads to an inconsistency with the lubrication approximation. However, retention of nonlinear curvature terms is required to capture the large gradient of the interface at the nose and rear of bubble and is therefore necessary to describe oscillatory bubble pinch-off.

The equation is fourth order in space, and in the same coflow configuration as section 3.1, has the following boundary conditions at the input nozzle

$$h(0,t) = h_0, \qquad q(0,t) = q_c, \tag{4.2}$$

where q is the volumetric flux per unit width defined as

$$q(x,t) = -\frac{\gamma}{3\mu}h^3\kappa_x. \tag{4.3}$$

For $q_c > 0$, the configuration provides a canonical example of a system that undergoes periodic pinch-off, producing a train of bubbles at a controlled frequency. The particular case of the system in which the viscous fluid is quiescent, $q_c = 0$, represents the generation of a single long (Taylor) bubble at a nozzle without pinch-off.

Previously in section 3.1, the necking zone system utilised a matching condition to the interior thickness of a Taylor bubble in order to close the system. In the case of a full bubble accommodated here, the position of the moving boundary $x_F(t)$ must also be determined such that the system requires a total of five boundary conditions. At the front of the bubble, we apply

$$h(x_F, t) = d, \qquad h_x(x_F, t) = \infty, \qquad q(x_F, t) = q_F(t), \tag{4.4}$$

representing the condition that the thickness at the nose of the bubble is given by the half-width of the channel, the symmetry condition at the bubble nose, and a continuity condition on the flux, respectively. The function $q_F(t)$ is an as-yet-unspecified flux of the continuous (liquid) phase at the nose. In general, $q_F(t)$ will be related to the injection conditions into the system. In the particular example of a coflow system, the flux at the front of the bubble is given by the total flux of flux injected into the channel by mass conservation

$$q(x_F, t) = q_F(t) = q_c + q_d. \tag{4.5}$$

To provide an explicit evolution equation for the nose, $x_F(t)$, we differentiate the boundary condition $h(x_F, t) = d$ with respect to time, giving

$$\dot{x}_F h_x + h_t = 0, \qquad (x = x_F). \tag{4.6}$$

With use of continuity $h_t = -q_x$, the above can be written

$$\dot{x}_F = \frac{q_x}{h_x} = \frac{\gamma}{3\mu h_x}\left(h^3 \kappa_x\right)_x \qquad (x \to x_F). \tag{4.7}$$

Using the conditions $h(x_F, t) = d$ and $q(x_F) = q_F(t)$, we obtain the further simplified expression

$$\dot{x}_F = \frac{3q_F(t)}{h} + \frac{\gamma h^3 \kappa_{xx}}{3\mu h_x} \qquad (x \to x_F), \tag{4.8}$$

which shows that the rate at which the bubble nose moves is related to the specified total flux $q_F(t)$, as well as the second derivative of the interface curvature at the nose.

The system of (4.1), (4.4) and (4.8) forms a free-boundary problem based upon both lubrication theory and retention of a full nonlinear curvature. Hence, we shall refer to this system as the nonlinear curvature lubrication theory (NCLT) in order to distinguish the model from the system presented in section 3.1. The model can be applied to any geometry of channel wall and input configuration, as long as the channel is symmetric about its centreline. By accommodating both time-dependence and nonlinear curvature, the model contains the elements necessary to describe the propagation of a complete bubble, including the nonlinear-curvature dynamics at the nose that are crucial for controlling the global structure of a Taylor bubble, as well as dynamic phenomena such as oscillatory pinch-off. It should be noted that retaining nonlinearity of the curvature is in conflict with the lubrication approximation, since lubrication theory is based on small interfacial slopes, whereas nonlinear curvature arises for large interfacial slope. The main effect neglected in the model as a whole is non-shear contributions to the viscous resistance to flow of the liquid phase, such as resistive stresses due to lateral extension. Such stresses are likely important at the bubble nose at large capillary numbers, where full Stokes contributions may be important, including viscous forces due to lateral extension. However, we will demonstrate that the model is able to predict all the key asymptotic structures of classical Taylor bubbles at small capillary numbers, in addition to nozzle-transition dynamics, and can thus serve as a helpful theoretical tool in the analysis of time-dependent capillary dynamics, whilst preserving the efficacy of lubrication modelling.

4.1.1 Non-dimensionalisation

To non-dimensionalise the system, we introduce the following non-dimensional variables:

$$x = d\hat{x}, \qquad h = d\hat{h}, \qquad q = q_d\hat{q}, \qquad t = \frac{d^2}{q_d}\hat{t}. \tag{4.9}$$

We choose a different non-dimensionalisation here, compared with chapter 3, since the parameter h_T used in (3.21) is specifically related to the formation of

Taylor bubbles. Here, we define a more general system that can describe both the formation of Taylor and non-Taylor bubbles.

Dropping hats, the governing equation (4.1) becomes

$$h_t = -\frac{1}{3C}\left(h^3\kappa_x\right)_x, \qquad \kappa = \frac{h_{xx}}{(1+h_x^2)^{3/2}}, \tag{4.10}$$

where $C = \mu q_d/\gamma d$ is a capillary number. The boundary conditions (4.4) become

$$h(0,t) = H, \qquad q(0,t) = Q, \tag{4.11a}$$

$$h(x_F,t) = 1, \qquad h_x(x_F,t) = \infty, \qquad q(x_F,t) = Q+1, \tag{4.11b}$$

where $H = h_0/d$ represents the ratio of the inlet nozzle width to the channel width, and $Q = q_c/q_d$ is the ratio of the liquid flux to the bubble flux. The kinematic condition (4.8) becomes

$$\dot{x}_F = 3(Q+1) + \frac{\kappa_{xx}}{3Ch_x} \qquad (x = x_F(t)). \tag{4.12}$$

The dimensionless system above depends on three dimensionless numbers: the capillary number C; the flux ratio Q and the ratio of the nozzle size to the channel width H. For a flux ratio $Q > 0$, both fluids are injected concurrently and pinch-off of a bubble occurs at regular intervals. The capillary numbers considered in previous works are typically small ($C \lessapprox 0.01$) such that surface tension forces are dominant, and bubbles are formed when the interface obstructs the injection of the continuous phase (e.g. Anna, 2016; Garstecki *et al.*, 2004). The parameter H is restricted to the range $0 < H < 1$. The flux ratio Q can take any value, but is usually considered in the range of $0.01 \lesssim Q \lesssim 10$ in experimental studies (e.g. Cubaud *et al.*, 2005; Garstecki *et al.*, 2006; Xiong *et al.*, 2007).

4.2 The injected and detached Taylor bubble

A fundamental component of systems involving the injection of fluid into a channel filled with another immiscible fluid is the formation of Taylor bubbles, defined as having length much larger than the channel width. These bubbles can either be

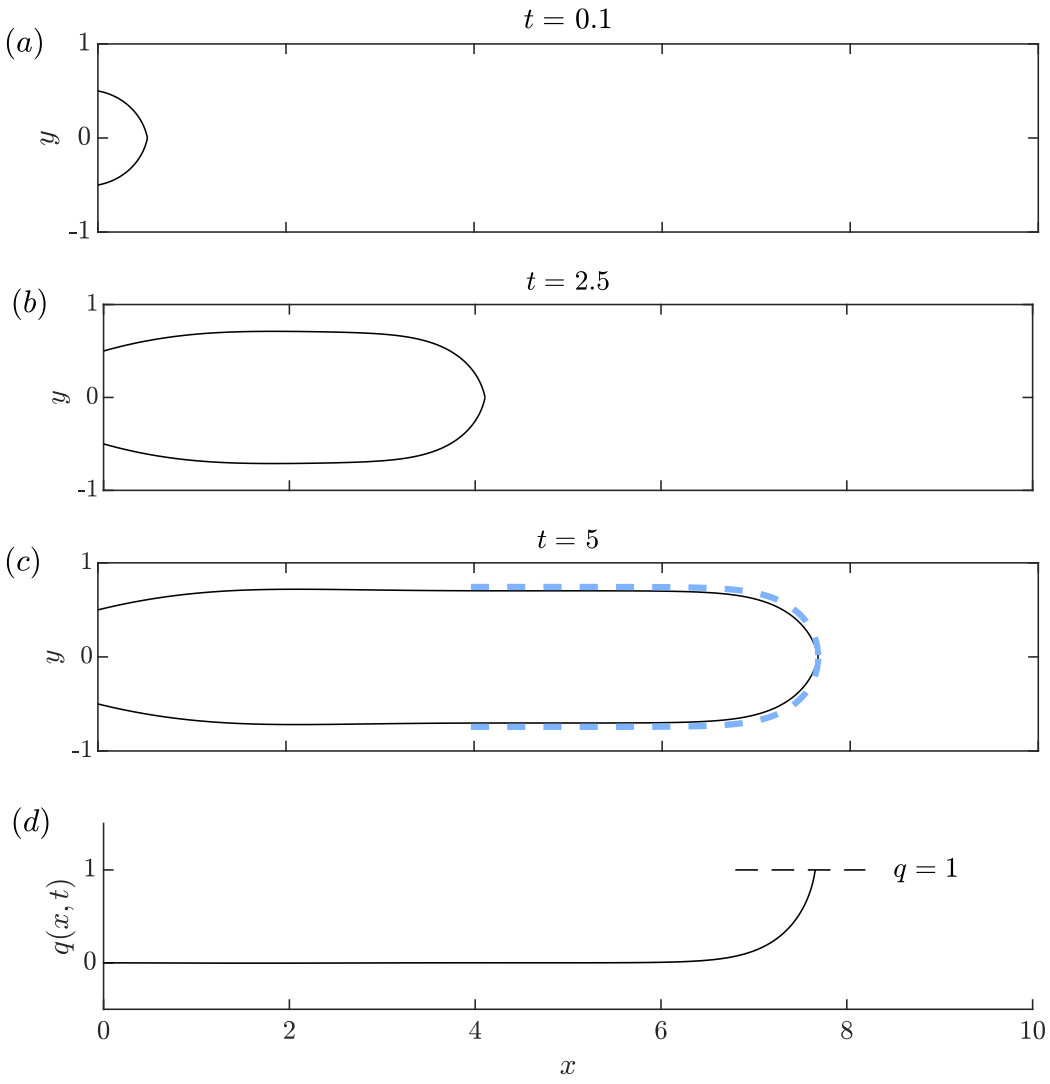

Figure 4.1: (a)-(c) Numerical solutions to the nonlinear curvature lubrication theory (4.10)–(4.12) for a quiescent ambient phase, $Q = 0$, capillary number $C = 0.2$, and relative input width $H = 0.5$, showing the progression of the interface $h(x,t)$ with time in (a)–(c). The travelling wave solution, given by the solution to (4.16)–(4.17), is overlayed as a dashed line for the final time shown in (c). (d) The profile of the film flux $q(x,t)$, showing the structure of the injected Taylor bubble, with an effectively stationary film surrounding the bubble in the region of uniform film thickness.

studied in the context of continuous injection, resulting in an ever extending bubble that remains attached to the nozzle, or as a detached bubble of finite volume that has been released into the liquid phase. This section serves as an introductory application and demonstration of the nonlinear-curvature framework to the formation of Taylor bubbles, components which are necessary foundations for our more general analysis of concurrent injection in section 4.3. This section will first apply NCLT developed above to the Taylor bubble, demonstrating in particular that the generalised lubrication theory automatically predicts the development of the asymptotic structure of a circular nose region coupled to a region of uniform film thickness as $C \to 0$, in conformity with Bretherton's theory. The results for the downstream steady travelling-wave states (section 4.2.1) specifically recover the predictions of Ratulowski & Chang (1989) in a two-dimensional geometry, providing a helpful check on the model in the context of travelling wave states.

4.2.1 The injected Taylor bubble

We first consider the case of continuous injection of the bubble phase only, corresponding to the NCLT (4.10)–(4.12) with $Q = 0$. The injected bubble phase forms a kind of one-sided Taylor bubble that remains attached to the nozzle for all times. An illustrative solution is shown in figure 4.1 for capillary number $C = 0.2$, and $H = 0.5$ fixed at the nozzle. As the bubble progresses through the channel, a thin film of constant thickness forms around the bubble.

Bubble nose and interior thickness

Let U denote the unknown steady dimensionless speed of the bubble nose. In seeking travelling wave states for the nose and interior of the Taylor bubble, we move into the frame of the bubble by defining the moving coordinate

$$z = x - Ut. \tag{4.13}$$

Seeking a steady state in the moving frame, (4.10) yields the travelling-wave equation

$$Uh_z = \frac{1}{3C}\left(h^3\kappa_z\right)_z. \tag{4.14}$$

Far upstream of the nose, the film is assumed to approach a constant value

$$\lim_{z\to-\infty} h = B, \tag{4.15}$$

where B is the as-yet-undetermined *interior thickness* of the fluid film surrounding the bubble upstream of the nose. The governing equation (4.14) with condition (4.15) is translationally invariant. Therefore, without loss of generality, we set the nose of the bubble at $z = 0$. The boundary conditions (4.4) at the nose then read

$$h_z(0) = \infty, \qquad h(0) = 1, \qquad q(0) = 1. \tag{4.16a-c}$$

Equation (4.14) has a first integral given by

$$U(h - B) = \frac{1}{3C}h^3\kappa_z \equiv q, \tag{4.17}$$

where the integration constant has been determined from (4.15). The travelling-wave system given by (4.17) and the remaining boundary conditions (4.16) is mathematically equivalent to the ordinary differential system considered by Ratulowski & Chang (1989). Imposing the boundary conditions (4.16), we obtain an expression for U as

$$U = \frac{1}{1 - B}, \tag{4.18}$$

which ensures conservation of total fluid volume in the travelling-wave state.

Equation (4.17) subject to (4.16) forms a third-order problem for the film thickness $h(z)$ describing the steady profile of the bubble in a moving frame, with an unknown number $B(C)$ representing the upstream asymptotic film thickness coating the sidewalls. We solve it using a shooting method in which we trial a value of B and integrate from an arbitrary upstream position at which we apply $h = B$ and $h_z = h_{zz} = 0$. We integrate forwards along the plateau and terminate once the solution develops an effectively infinite gradient. Depending on whether the terminating thickness of the film is greater than or less than unity, such that the bubble cap occurs at the required channel centre, we propose a new trial for B until the nose conditions of $h(0) = 1$ and $h_z(0) = \infty$ are met. We then shift the solution horizontally such that the nose is located at $z = 0$. Figure 4.2(a) and (b) show examples of the travelling-wave solution for capillary numbers $C = 0.02$

and $C = 0.2$ respectively. There is good agreement between the time-dependent solutions of the nonlinear curvature model and the corresponding travelling-wave solutions, as shown in figure 4.1(c). The slight discrepancy between the numerical solution and the travelling-wave solution shown in figure 4.1(c) is attributed to approximations made within our time-dependent solver (described in more detail in appendix 4A.1). In particular, the shooting method used to obtain a travelling-wave solution is terminated when the front of the bubble has an effectively infinite gradient. However, the infinite nose gradient cannot be represented in the Cartesian system used within the time-dependent solver, and hence a finite gradient is required. We show in appendix 4A.1 that the finite gradient implementation converges towards the infinite nose predictions, and that the gradient chosen for all solutions shown in this work is large enough to limit the size of the discrepancy.

The solutions of the travelling wave theory with nonlinear curvature (figure 4.2a,b) indicate the emergence of a near semi-circular front connected through a short transition zone to the coating film thickness interior to the bubble. The model thus appears automatically to recover the matched asymptotic structure of a small-C long bubble developed by Bretherton. We recall from section 2.1.2 that Bretherton (1961) described the structure in terms of two asymptotic regions: a large outer region representing the interior of the bubble and its preliminary lead-in to the nose in which the governing equation can be linearised; and a frontal region in which the full nonlinear curvature dynamics are important. The solution in the frontal region takes the form of a simple leading-order circular arc (or hemisphere in the axisymmetric case) with radius (and hence curvature) set by the width of the geometry. By matching the curvature given by this frontal deck as a condition on the second derivative of film thickness in the linearised outer region, the Bretherton theory yields predictions for the nose and interior of a long (Taylor) bubble for $C \to 0$. The results of figure 4.2(a,b) show that the nonlinear curvature model automatically recovers the Bretherton structure as $C \to 0$, including both the upstream linear-curvature region and the frontal circular arc, and their smooth connection across a narrow transition zone.

In order to provide a direct quantitative demonstration of the recovery of the Bretherton prediction, we review the Bretherton theory and compare it to the

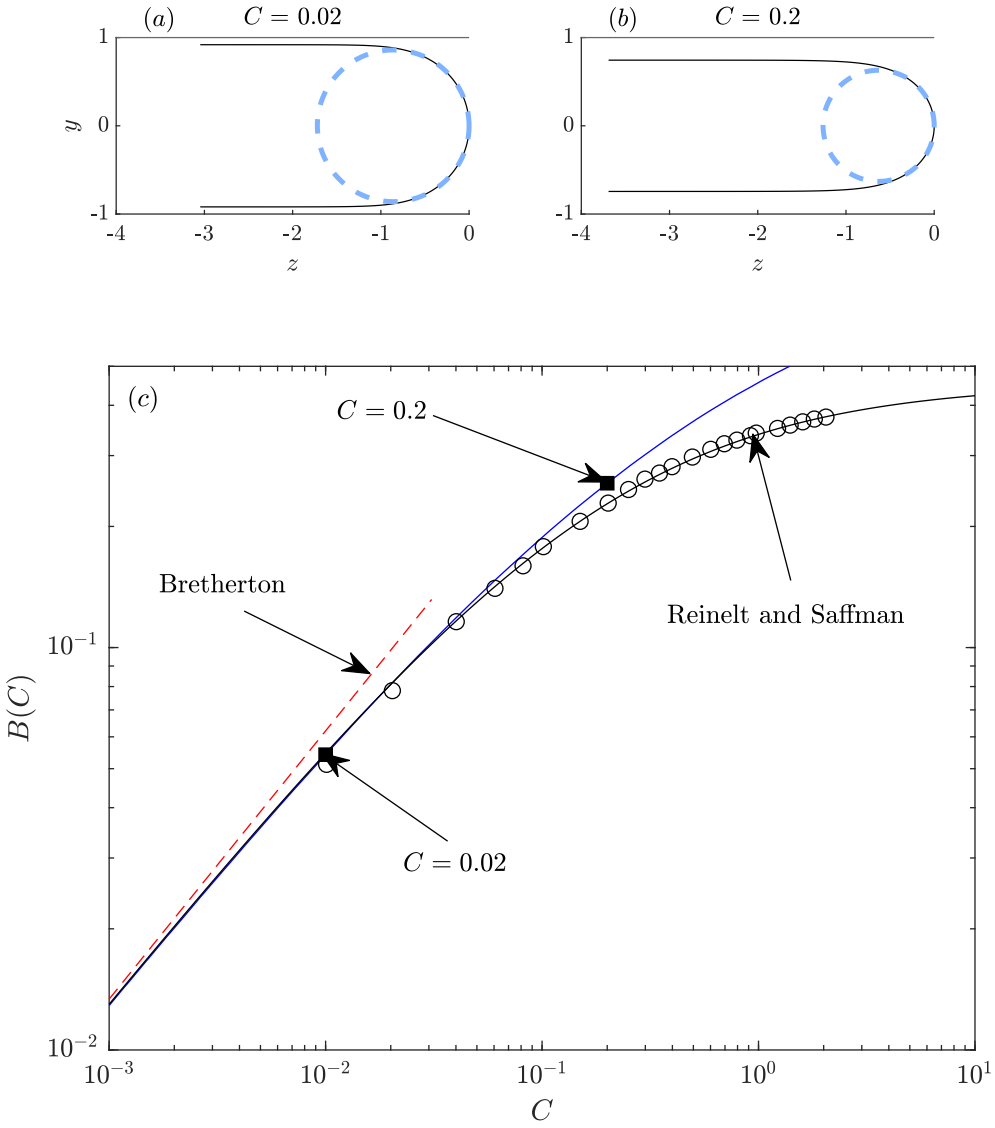

Figure 4.2: (a,b) Travelling wave solutions as predicted by the system of (4.16)–(4.17), illustrating the generation of the Bretherton asymptotic structure comprising an approximately circular front connected to a region of near uniform film thickness upstream, for two different capillary numbers $C = 0.02$ and 0.2, respectively. The leading-order circular nose is overlaid as a dashed circle in each case. The film thickness surrounding the bubble is thinner for $C = 0.02$ than $C = 0.2$. (c) The universal function $B(C)$ giving the film thickness as a function of the capillary number, as predicted by the system of (4.16)–(4.17) (solid, blue), exhibiting agreement with Bretherton's theoretical result for the small-C limit (4.22) (dashed). The analytical function determined in section 3.1.1 as (3.6) (solid, black) is overlayed to highlight its superior agreement with the numerical results of Reinelt & Saffman (1985), shown as unfilled circles.

predictions of the generalised lubrication theory. The outer region is defined by linearised curvature, namely $\kappa \approx h_{zz}$, for which the governing equation simplifies to

$$U(h - B) = \frac{1}{3C} h^3 h_{zzz} = q. \tag{4.19}$$

In the small capillary number limit, $B \to 0$, the dimensionless travelling wave speed introduced in (4.18) becomes $U \sim 1$. Further, we can absorb C from the problem by defining the further scaled variables:

$$z = C^{1/3} Z, \qquad h = C^{2/3} H. \tag{4.20}$$

The rescaled system is

$$\tfrac{1}{3} H^3 H_{ZZZ} = H - \beta, \tag{4.21a}$$

$$\lim_{Z \to -\infty} H = \beta, \qquad \lim_{Z \to \infty} H_{ZZ} = 1. \tag{4.21b}$$

where $\beta = C^{-2/3} B$. Equation (4.21a) is known as the Landau-Levich equation (Landau & Levich, 1988). The system forms a free-parameter problem for β. Solving (4.21) by treating β as a shooting parameter with bisection, we obtain a solution that satisfies the boundary conditions if and only if $\beta \approx 1.3375$, consistent with Bretherton (1961). From this, we obtain the relationship between the dimensionless coating thickness and capillary number,

$$B \sim 1.3375\, C^{2/3} \qquad (C \to 0), \tag{4.22}$$

shown as a dashed line in figure 4.2(c). There is excellent agreement between the prediction of the travelling-wave theory of the nonlinear curvature model defined by (4.17) subject to (4.16), and the Bretherton prediction above for $C \to 0$, showing explicitly that the theoretical framework is recovering the predictions of Bretherton in this limit, as required. The predictions of the nonlinear curvature model significantly extend the Bretherton asymptotic result for film thickness to higher capillary number $C \approx 0.1$, but for more moderate capillary number the prediction begins to more significantly deviate from the film thickness calculated numerically by Reinelt & Saffman (1985). This divergence was also acknowledged in the predictions of the nonlinear curvature lubrication theory studied by Ratulowski & Chang (1989) in the context of finite bubble progression through a capillary.

Nozzle transition zone

An interesting feature of the evolution shown in figure 4.1 for the case $Q = 0$ is that the solution retains a dependence on time in the region near to the nozzle. The transition between the nozzle and the Taylor bubble forms a disturbance that spreads gradually outwards from the nozzle for all time. In essence, the solution behaves like a capillary step between the nozzle thickness and the bubble coating thickness in this region.

We propose the following asymptotic system describing the nozzle transition zone. This is a similar system as derived in section 3.1.2, but for the specific case whereby the continuous phase is not injected, $Q = 0$. For this, we retain the time-dependent model with linearised curvature, on the assumption that the disturbance spreads laterally and hence becomes increasingly slender with time. Further, we apply a matching condition that the film approaches the coating thickness B downstream of the nozzle transition. Thus, the proposed reduced system for the nozzle transition is

$$h_t = -\frac{1}{3C}(h^3 h_{xxx})_x, \tag{4.23}$$

with boundary conditions

$$h(0,t) = H, \qquad h_{xxx}(0,t) = 0, \qquad \lim_{x\to\infty} h = B. \tag{4.24}$$

The system above represents a release of a capillary flow maintained at a constant thickness at a fixed position $x = 0$ that transitions to a uniform asymptotic film thickness as $x \to \infty$.

Noting that there is no time-independent intrinsic time scale in the system (4.23)–(4.24), we can anticipate that it supports similarity solutions. The relevant similarity variables, derived from scaling, are

$$\eta = \left(\frac{B^3}{C}t\right)^{-1/4} x, \qquad f = \frac{h}{B}. \tag{4.25}$$

Under these scalings, $h_x \sim (t/BC)^{-1/4}$, and hence $h_x \to 0$ as $t \to \infty$, yielding self-consistency with the assumed slenderness in this region. In terms of the similarity variables above, the governing equation becomes

$$\frac{1}{4}\eta f' = \frac{1}{3}\left(f^3 f'''\right)'. \tag{4.26}$$

The boundary conditions are

$$f(0) = D, \qquad f'''(0) = 0, \qquad \lim_{\eta\to\infty} f = 1, \tag{4.27}$$

where $D \equiv H/B$. We solve (4.26) using a shooting method in which we impose the conditions at $\eta = 0$, and implement shooting with bisection on the first and second derivatives of f at $\eta = 0$. The solutions for a selection of D are shown in figure 4.3. We notice that, for $D > 1$, the initial gradient of the solution is negative and the solution corresponds to a bubble with a convex shape in the nozzle transition region. Conversely, for $D < 1$ the gradient is initially positive and the bubble exhibits a concave shape.

Further solutions are transformed into time-dependent coordinates and overlaid onto solutions to the full time-dependent model in figure 4.4 showing good agreement between the predictions of the similarity solution and the NCLT. The parameters of these solutions are $C = 0.2$ and $Q = 0$, corresponding to a flat film region of thickness $B(C) \approx 0.37$. The height of the interface at the point of injection is fixed as $H = 0.3$ and $H = 0.5$ in (a) and (b) respectively, giving $D \approx 0.539$ and $D \approx 1.348$. Figure 4.4(c) shows the maximum/minimum film thickness for a concave/convex bubble approaches the predicted similarity value, shown as horizontal dashed lines.

We summarise the full asymptotic structure of an injected Taylor bubble as follows. The front of the bubble grows proportionally with time t. There is a transition zone established between the nozzle and the long bubble region that is defined by a time-dependent 'lock release' structure involving capillary spreading of the interface that grows as $t^{1/4}$ (e.g. Aradian *et al.*, 2001; McGraw *et al.*, 2012). In essence, the downstream transition to a long bubble sets up a step in thickness between the nozzle and the coating thickness left by the bubble. The resulting interface evolution is then effectively a capillary lock release, creating an ever unsteady self-similar expansion in front of the nozzle while the inviscid bubble fluid flows passively through it.

4.2.2 The finite (detached) Taylor bubble

Once pinch-off has occurred, the injected bubble separates into two disjoint regions: the remnant attached to the input, and a detached region forming a closed

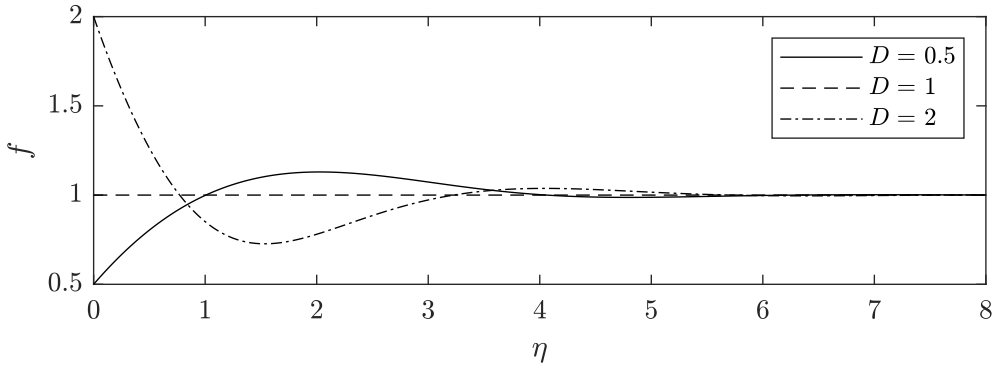

Figure 4.3: Similarity solutions describing the time-dependent relaxation of the interface in the transition zone between the nozzle and the flat section of the Taylor bubble in the case of zero ambient flux $Q = 0$, given by the numerical solution of the system (4.26)–(4.27). The solution is shown for $D = 0.5, 1$ and 2.

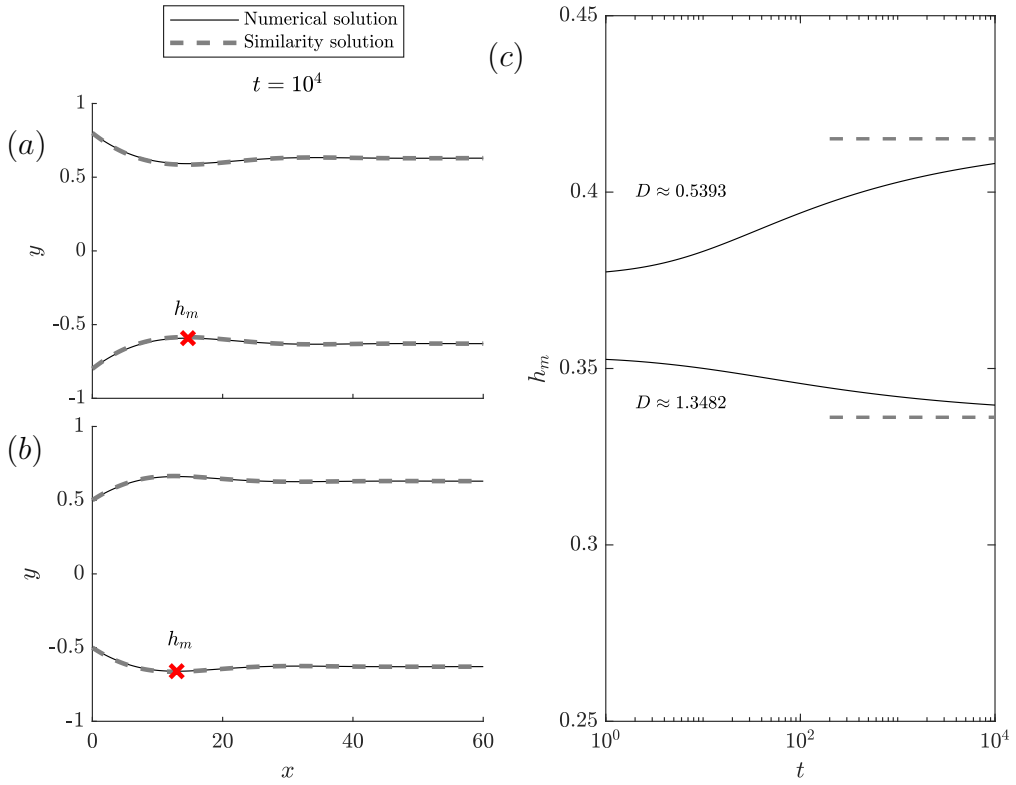

Figure 4.4: (a) and (b) show the shooting solution of (4.26) (dashed) overlaid onto time-dependent solution for the nonlinear curvature lubrication theory with $C = 0.2, Q = 0$ with $H = 0.3$, and $H = 0.5$ respectively. The red cross represents $h_m(t)$, the height of the interface at the stationary point. (c) shows the numerical time-dependent prediction of $h_m(t)$ (solid) approaches the prediction of the similarity solution (dashed) for late time in each case.

bubble. The closed, detached bubble is transported by the surrounding fluid only. Bretherton (1961) found that the thickness of the fluid film surrounding the bubble is determined uniquely by the conditions at a near-circular bubble front. The rear of the bubble instead has a spatially oscillatory profile and a steady solution matching to any film thickness. The solutions of detached Taylor bubbles presented in this sub-section is primarily review of Ratulowski & Chang (1989) as we reproduce results from their travelling wave analysis to test our numerical implementation.

The system for the detached bubble comprises the same steady-state travelling wave equation of (4.17) along with continuity conditions at both a nose ($z = 0$) and rear position ($z = z_R < 0$), along with a volume constraint. The system is

$$\frac{h - B}{1 - B} = \frac{1}{3C} h^3 \kappa_z, \tag{4.28a}$$

$$h(0) = 1, \qquad h_z(0) = \infty, \qquad q(0) = 1, \tag{4.28b}$$

$$h(z_R) = 1, \qquad h_z(z_R) = -\infty, \qquad q(z_R) = 1, \tag{4.28c}$$

and the volume constraint is

$$\int_{z_R}^{0} h \, \mathrm{d}z = V, \tag{4.29}$$

where V represents the volume per unit width of bubble fluid.

We solve the system (4.28)–(4.29) in two parts: the front, given by solving (4.28a) subject to (4.28b) using shooting as detailed in section 4.2.1; and the rear given by (4.28a) subject to (4.28c) solved similarly using shooting. The two solutions plateau to the same uniform film thickness and are joined by specifying a value of z_R such that the volume V is consistent with (4.29). The resulting solution is shown in figure 4.5 for two example choices of capillary number $C = 0.02$ and $C = 0.2$. The results show that for smaller capillary number, the surface tension forces are dominant over viscous stresses and so the bubble is able to attain form with lower surface energy. This trend is clear in the results, showing that the rear of the bubble is more circular for $C = 0.02$ than $C = 0.2$.

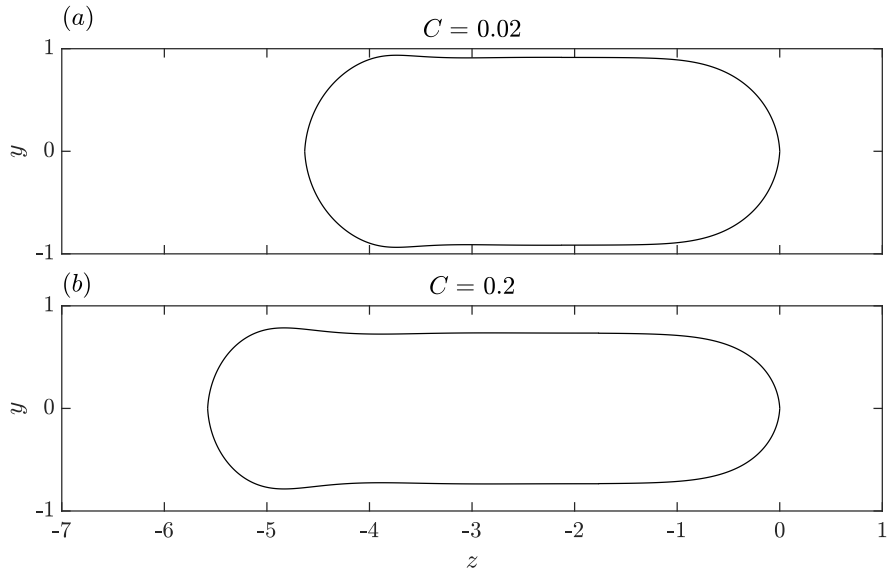

Figure 4.5: Two illustrative examples (a) $C = 0.02$, (b) $C = 0.2$ of finite Taylor bubbles formed by solving the travelling wave systems for the front and the back of the bubble, given by (4.16)–(4.17), and (4.28) respectively. The areas of the bubbles are equivalent, $V = 7.68$.

4.3 Coflow dynamics

We now consider the concurrent injection of both fluid phases ($Q > 0$). Figure 4.6 presents an illustrative example of bubble production for parameters $C = 0.2$, $Q = 0.2$, and $H = 0.5$. The first two plots show the progression of the fluid-fluid interface, showing the development of a Taylor bubble. At time $t_* \approx 10.94$, pinch-off occurs when the thickness of the bubble in the necking region goes to zero locally (figure 4.6(c)), separating the flow into a detached Taylor bubble and a remnant of the inviscid fluid between the pinch-off position and the input nozzle. Figure 4.6(d) shows a short time after pinch-off, demonstrating the rounding of the bubble rear, as well as the continued injection of the bubble phase at $x = 0$. The final plot (e) shows the truncation of the solution at the point of pinch-off. The cycle then repeats periodically at a regular interval, with a new Taylor bubble generated and pinch-off instigated, forming a train of bubbles. The figure 4.6 demonstrates the periodic nature of bubble formation that can be captured by the nonlinear curvature model; a feature that was not possible in the analysis

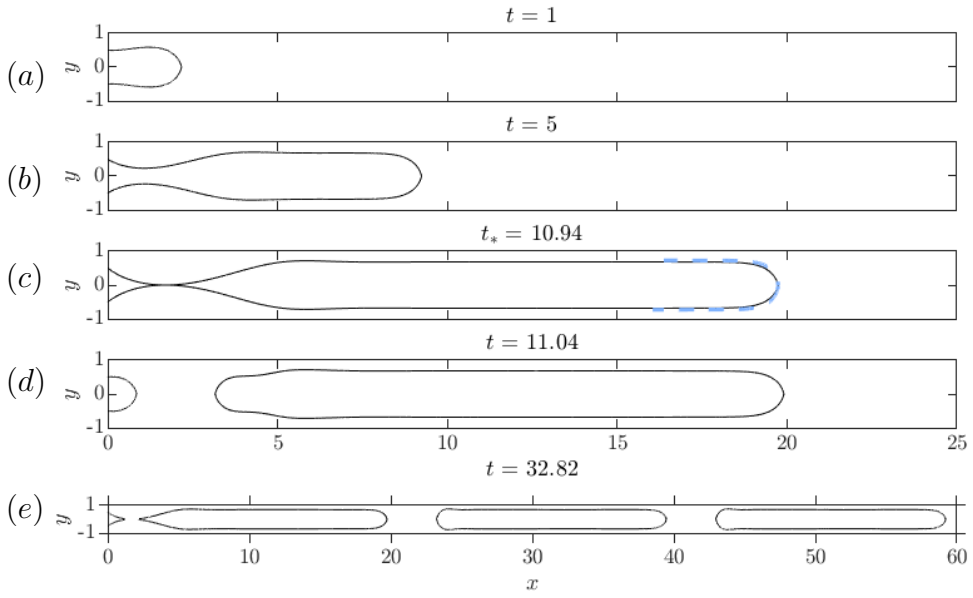

Figure 4.6: Numerical solution to the nonlinear curvature lubrication theory (4.10)–(4.12) with parameters $C = 0.2$, $Q = 0.2$, $H = 0.5$. A Taylor bubble forms at $t_* \approx 10.94$, shown in (c), before progressing through the channel as a detached bubble (d). Three detached bubbles are shown in (e), showing the regular frequency of production and generation of a bubble train.

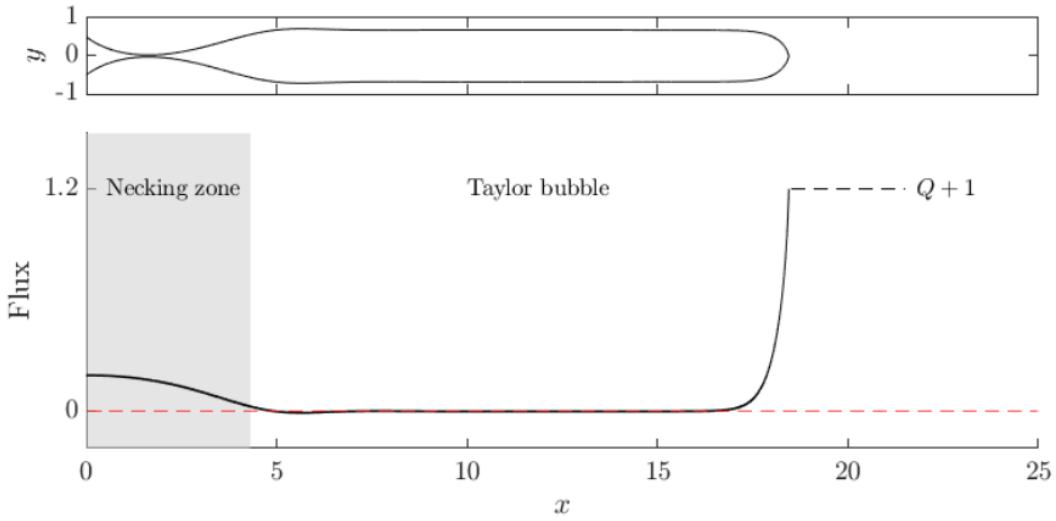

Figure 4.7: An illustrative solution to the NCLT at pinch-off time (c.f. figure 4.6(c)). The corresponding flux is zero in the thin film region which blocks the downstream flow of the viscous film, causing localised thinning in the necking zone and, ultimately, pinch-off. At the boundaries of the domain, the conditions on the flux are $q(0,t) = Q$, $q(x_F,t) = 1 + Q$, where $Q = 0.2$ here. The transition between the necking zone and the Taylor bubble illustrated here is defined by where the flux of the film is 10% of its value at the input ($q = 0.1\,Q$)).

of chapter 3.

Figure 4.7 shows the solution at the point of pinch-off and its corresponding flux $q(x,t)$, illustrating the separation of the flow structure into two regions: a necking zone containing a region of localised thickening of the film in the vicinity of the nozzle; and a Taylor bubble extending progressively downstream, illustrating the flux profile of the formed Taylor bubble. The latter comprises a long region of approximately uniform bubble thickness and zero flux; this structure formed the basis of our asymptotic theory in section 3.1. Hence, we have demonstrated that the NCLT is able to recover the asymptotic flow structure comprising a necking zone and the extending downstream Taylor bubble.

4.3.1 Testing the pinch-off time prediction

In this section, our primary focus is testing the pinch-off time prediction of the necking zone model presented in section 3.1 against the NCLT formulated in section 4.1. The nonlinear curvature lubrication framework allows for the periodic formation of bubbles in a two-dimensional coflow geometry, whereas the necking zone model is limited to the formation of a singular bubble. The initial condition for the formation of the first bubble is specified by a uniform film thickness, whereas the subsequent bubbles are initialised using the remnant left after the detachment of the previous bubble. We notice that the cycle of bubble generation and subsequent pinch off repeats periodically at a regular interval defined by t_*, and so we define the numerically determined time to pinch off predicted by the NCLT as the pinch-off time predicted for generation of the third bubble.

Figure 4.8 shows the time for bubble pinch off predicted by the NCLT (4.10)–(4.12) (blue, solid) across a range of input flux ratios Q and capillary number $C = 0.01$. The time for bubble production decreases with an increase in fluid flux ratio, specifically indicating a $-4/3$ power law trend. The results are compared to the pinch-off times predicted by the necking zone system (3.22)–(3.24) for the generation of a singular bubble (black, solid). The predictions of the models exhibit excellent agreement, providing validation that the prediction for pinch-off time provided by the necking zone system is consistent with the regular, periodic pinch-off time predicted by the NCLT. At larger flux ratios, the pinch-off times

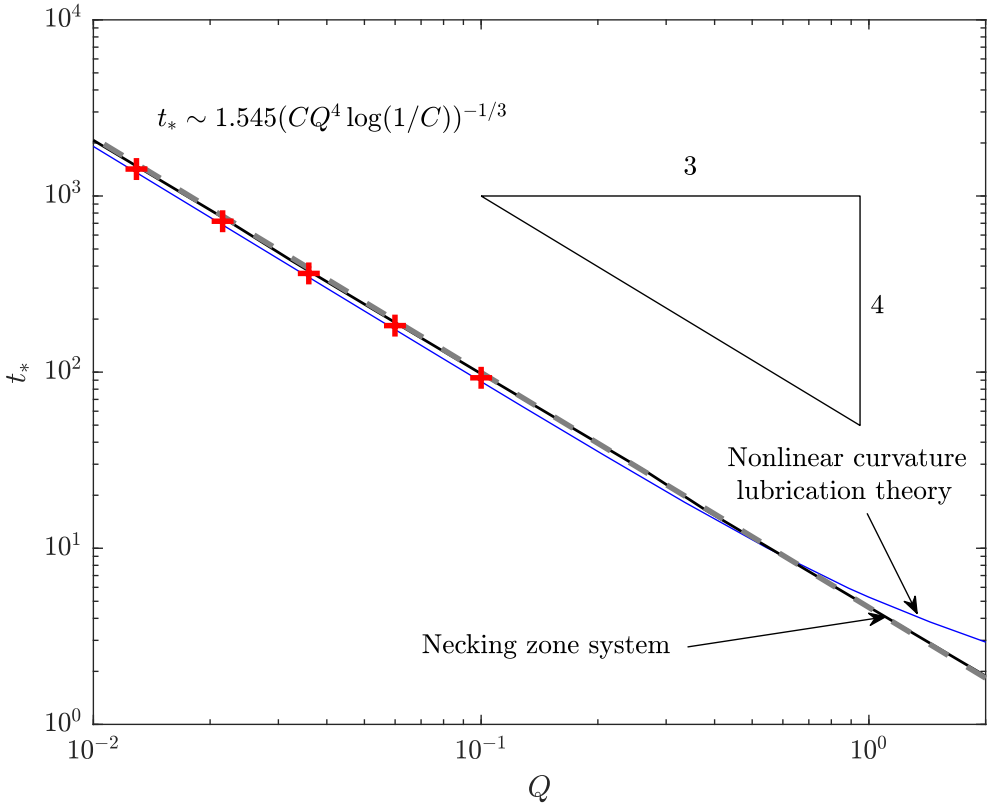

Figure 4.8: The numerical prediction for pinch-off (blue, solid) time, as predicted by the nonlinear curvature lubrication theory (4.10)–(4.12), is compared to the prediction of the necking zone system (3.22)–(3.24) (black, solid) derived in section 3.1.2 for $H = 0.1$ and capillary number $C = 0.01$, as a function of the flux ratio Q. The dashed line shows the asymptotic prediction of (4.30) for the Taylor bubble regime, demonstrating the scaling of the pinch-off time with $t_* \sim Q^{-4/3}$. The red crosses represent the small-C frequency prediction (4.31).

predicted by the NCLT deviate from the prediction of the necking zone system due to the formation of smaller bubbles that do not exhibit the characteristic Taylor bubble shape; bubbles of this kind will be explored in section 4.3.2.

The NCLT therefore provides some validation of the necking zone predictions presented in chapter 3. Whilst, as previously discussed, the NCLT is an inconsistent model, the approach has been shown by (Ratulowski & Chang, 1989) to accurately recover predictions of uniform Taylor bubble thickness for small capillary number $C \lesssim 0.1$. At more moderate capillary number, we would expect that the predictions of the nonlinear curvature theory would deviate from the necking zone model due to the discrepancy in the predictions for the fluid film thickness shown in figure 4.2. However, for sufficiently small capillary number, we speculate that the NCLT uses the same modelling approach as Ratulowski & Chang (1989) and should therefore be able to accurately predict the periodic formation of bubbles. A complete validation of the NCLT against full Stokes flow simulations is left for future work.

4.3.2 From Taylor to non-Taylor bubble pinch-off

Figure 4.9 shows a numerical solution to the NCLT (4.10)–(4.12) with $H = 0.5$, as in figure 4.6. The flow rate ratio is larger, $Q = 3$, and the capillary number is chosen to be smaller ($C = 0.01$). We notice that the bubble pinches off before it is able to form an elongated pill shape; instead, a smaller more circular bubble is formed. Hence, the time-dependent solutions provide an illustrative example that our model can also account for bubbles outside of the Taylor flow region. The final plot in figure 4.9(d) shows four cycles of bubble formation, demonstrating the progression from injection of bubble fluid until the point of pinch-off.

Since the NCLT is able to describe both the formation of Taylor bubbles and smaller non-circular bubbles, we can compare the NCLT predictions for pinch-off time to the asymptotic predictions for pinch-off time associated with Taylor bubble formation derived in section 3.2. In this way, we can map a regime diagram over the C–Q parameter space, partitioned based on type of bubbles formed (i.e. Taylor vs non-Taylor) with the Taylor-bubble region being defined by where the

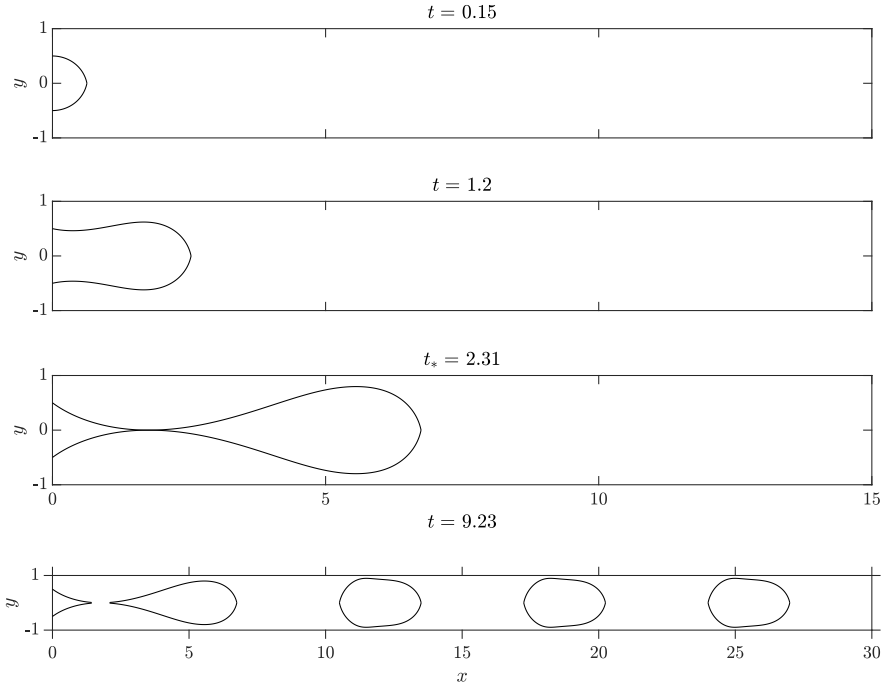

Figure 4.9: Numerical solution to the nonlinear curvature lubrication theory (4.10)–(4.12) for capillary number $C = 0.01$, and flux ratio $Q = 3$, showing the formation of smaller, more circular (non-Taylor) bubbles.

prediction of the associated regime (3.56) is within 5% of the prediction of the NCLT.

The nondimensionalisation used in this chapter is different to that used in the necking zone theory of chapter 3. To compare the numerical predictions of this chapter to the asymptotically derived results presented previously in chapter 3, we must rescale the dimensional results for pinch-off time presented in section 3.3 as (3.56) and (3.57) in terms of the non-dimensional system presented in this chapter. Specifically, recasting the dimensional pinch-off time predicted by (3.56) into the non-dimensional parameters of the system presented in this chapter gives a prediction for pinch off time as

$$t_* = \hat{t}_*(H, B(C)) \left(\frac{B^7}{CQ^4} \right)^{1/3}, \tag{4.30}$$

where $\hat{t}_*(H, B)$ is the same numerically derived dimensionless solution for pinch-off times derived in section 3.1.3 and plotted in figure 3.5. The asymptotic predic-

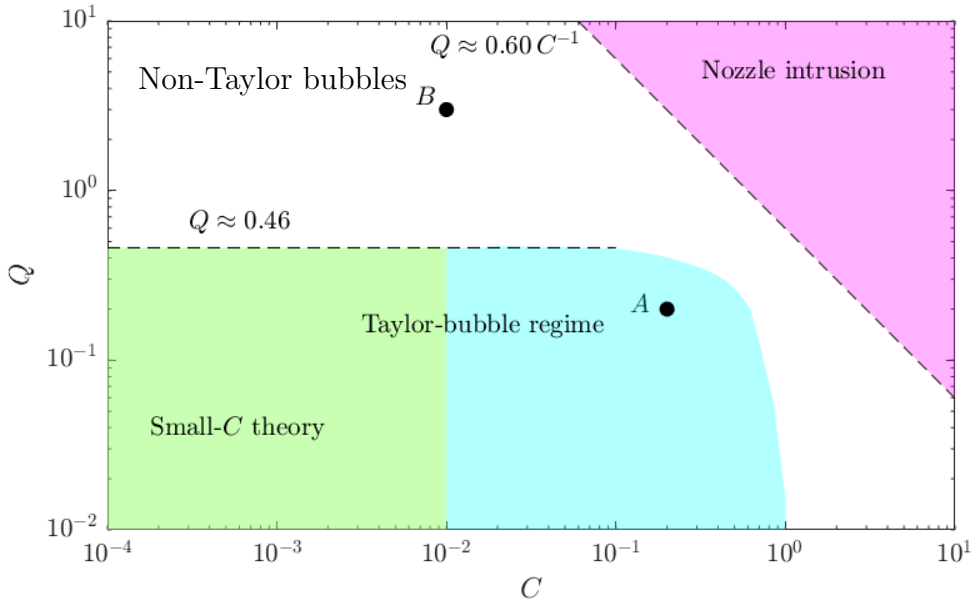

Figure 4.10: Regime diagram demonstrating the existence of a Taylor-bubble regime and a thin film regime contained as a sub-regime within this region of the C–Q parameter space. The black markers correspond to example solution A, shown in figure 4.6, and B shown in figure 4.9 respectively. The nozzle intrusion region is defined by a critical boundary beyond which our numerical solutions break down owing to the development of an infinite interfacial gradient at the nozzle.

tion for the pinch-off time of Taylor bubbles (4.30) is overlayed as a grey dashed line in figure 4.8, exhibiting excellent agreement with the predictions of the NCLT for small Q. At larger flux ratios, solutions to the NCLT predict smaller bubbles that do not exhibit the characteristic Taylor bubble shape (e.g. figure 4.9), and hence the predictions deviate from (4.30).

Similarly, the prediction determined from the quasi-static analysis in the small capillary number limit (3.57) can be recast to give the dimensionless prediction

$$t_* \sim 1.545 \left(\frac{1}{CQ^4 \log\left(1/C\right)} \right)^{1/3}. \tag{4.31}$$

The small capillary number prediction (4.31) is overlayed in figure 4.8 as red

crosses for $C = 0.01$, showing excellent agreement with the predictions of both the NCLT and the necking zone model.

Figure 4.10 provides a regime diagram in the C–Q space showing regions in which the Taylor-bubble regime applies (blue shading), and its small-C limiting sub-regime (green shading). To define the regions, solutions to the NCLT (4.10)–(4.12) were found across a range of values over the parameter space and the prediction was compared to either (4.30) or (4.31), defining the corresponding regime of the parameter space as where the two predictions differ by at most 5%. The solutions shown in figure 4.6 provide an example within the Taylor-bubble regime, labelled with a black marker as example A on the regime diagram. We see that the emergence of the Taylor-bubble regime is essentially based on two conditions: a condition on the flux ratio $Q \lesssim 0.5$ and a condition on the capillary number $C \lesssim 1$, together forming an approximately rectangular region of the parameter space. Thus, assuming that $C \lesssim 1$, the emergence of the Taylor-bubble regime is based independently on the ratio of the bubble flux to the liquid flux.

The regime diagram shown in figure 4.10 is determined by direct comparison of asymptotic and nonlinear curvature lubrication theory predictions, resulting in a division of the parameter space that is somewhat less schematic than the equivalent figure 3.6 shown in section 3.2.3, which was determined by assessing the validity of asymptotic assumptions to within some specified tolerance. The boundary of the Taylor bubble regime was previously found to correspond to a horizontal line in the (C, Q) parameter space; this is confirmed here by direct comparison of the NCLT (4.10)–(4.12) to (4.30), representing the blue region of figure 4.10. The numerically determined boundary of the long-bubble region, found here as $Q \approx 0.46$, corresponds to a prediction of the asymptotic boundary $x_N(t_*) \ll 0.69\, x_F(t_*)$. We notice that the prefactor 0.69 corresponds to a relatively large tolerance in the Taylor bubble approximation (3.55), suggesting that the time-dependent necking zone theory (3.22)–(3.24) is consistent even for relatively short Taylor bubbles (on the boundary of the asymptotically consistent regime). The boundary defining the small capillary number sub-regime in figure 4.10 is similar to the previous partition calculated in section 3.2.3, suggesting

that the pinch-off time predictions of the necking zone model (3.22)–(3.24) and the NCLT are similar in the small capillary number limit.

Analysis of the time-dependent evolutions shows that there is a critical flux Q above which the gradient of the interface transitions to being infinitely steep at the nozzle. Physically, this feature can be interpreted as a situation where the interface begins to intrude some distance into the interior of the nozzle. The region of the parameter space where this phenomenon occurs is indicated in purple in figure 4.10, which we determined by performing a sweep of the relevant part of the parameter space and checking for the breakdown in numerical solutions caused by this effectively infinite interfacial gradient at the nozzle. While we can identify the occurrence, we cannot, in Cartesian coordinates, integrate the model forwards in such situations beyond the time at which the interface becomes infinitely steep because the interface position becomes multivalued. In principle, these states could be considered by formulating an appropriate (non-Cartesian) coordinate system. A similar phenomenon was recognised by Salman *et al.* (2006) in their experimental investigation into Taylor bubble formation in a coaxial configuration. Our numerical determination of the boundary suggested that the critical breakdown is given by $Q \gtrsim 0.60\, C^{-1}$. It is apparent that the product QC, which can be interpreted as the capillary number of the liquid phase, is the key control of the occurrence of this phenomenon.

The white space on the regime diagram highlights that there exist solutions that fall outside of the Taylor-bubble regime, and do not exhibit the nozzle intrusion characteristic, particularly for small capillary numbers. An example of such a solution was shown in figure 4.9 and its corresponding position on the regime diagram is labelled with the black marker B. We notice that, in this case, the bubble formed has comparable longitudinal and lateral scales, forming a non-Taylor (more circular) bubble, without the development of an extended region of uniform coating interior to the bubble. We speculate that there lies a further asymptotic regime, defined by the property of a very large bubble flux, $Q \to \infty$, that describes a pinch-off regime that forms near-circular bubbles, which could be explored further using the model we have developed in this chapter.

4.4 Model limitations

Whilst the model is able to conveniently capture the time-dependent progression of the gas-liquid interface and predict the frequency of bubble production within a coflow geometry, we recognise limitations to the framework presented. Our model utilises lubrication theory to describe the fluid-fluid interface of a confined bubble in a channel, but retains a nonlinear curvature at the bubble front. Such a model contains the ingredients needed to account for the effect of nonlinear curvature at the nose which have a global impact on the bubble (a relevant solution would not be possible with linear terms alone), whilst allowing for the flexibility to predict dynamic phenomena. Lubrication theory requires small gradients but nonlinear curvature is required to capture the immediate dynamics in regions of infinite gradients (i.e. the front and back of a bubble). The combination of these theories suggests a contradictory model, however the model has demonstrated its capacity to automatically recover the asymptotic regimes associated with the Bretherton limit $C \to 0$. Moreover, the key pinch-off dynamics in the necking zone conform to the linearised curvature theory (section 3.1) such that, in the case of this configuration and small C, our model recovers all asymptotic regimes consistently. Additionally, the model framework can be justified as existing papers have used similar approaches and validated successfully against numerical or experimental results, setting a precedence for our approach (e.g. Lu *et al.*, 2023; Ratulowski & Chang, 1989; Snoeijer, 2006). However, in order to fully validate the nonlinear lubrication model presented herein, we would similarly require comparisons of the model results to numerical simulations of the full Stokes equations, or to experimental data.

The main effect neglected in the model is non-shear contributions to the viscous resistance to deformation in the liquid phase. Such contributions would include, for example, the effect of lateral extensional stresses in front of the bubble nose and other full-Stokes effects such as recirculation in the liquid slugs between gas bubbles. At small capillary numbers, the pinch-off dynamics and interior of the Taylor bubble conform with our model, exhibiting self-consistency, as demonstrated in figure 4.2 and in the self-consistent linearised-curvature regime of the necking zone in section 3.1. The experimental works of Taylor (1961) and

Cox (1962) investigate the amount of viscous fluid left on the walls of a channel upon the injection of an inviscid fluid for capillary numbers up to $C \approx 2$. Both authors concluded that as the capillary number increases, the coating thickness approaches a constant. Cox (1962) proposes a limiting asymptotic value of 0.40, justifying the plateau by the viscous forces becoming dominant over surface tension for $C \gtrsim 1$. In contrast, our model predicts a continued increase in the thin film thickness at large capillary numbers (figure 4.2(c)). The result is consistent with that of Ratulowski & Chang (1989) wherein corresponding travelling wave solutions are proposed in the case of the finite Taylor bubble. The discrepancy at large capillary numbers can likely be explained by the neglect of viscous resistance to lateral extension at the bubble nose, as we only model resistance to shear in our lubrication framework. As the capillary number increases, the surface tension effects become weaker such that the details of the full-Stokes viscous flow at the leading bubble nose become more important.

Another limitation associated with the large Q parameter space is the prediction of 'nozzle intrusion'. As explained in section 4.3.2, there exists a critical boundary beyond which our model predicts an infinite interfacial gradient at the nozzle, likely representing a situation where the film partially intrudes into the nozzle. This region of the C–Q parameter space is inaccessible for the Cartesian formulation of our model but could potentially be addressed under an alternative parameterisation of the interface.

Appendix 4A. Time-dependent numerical solver

In this section we outline the development, testing and implementation of our method of lines (MOL) technique used to solve the time-dependent nonlinear curvature lubrication theory (4.10)–(4.12) describing the evolution of the fluid-fluid interface of a bubble injected into a fluid-filled channel.

4A.1 Finite nose gradient approximation

First, we recognise that the infinite gradient at the nose (4.11b) cannot be represented in our (Cartesian) system. However, we can approximate the condition

by introducing a parameter $g > 0$ to represent a finite gradient at the nose, and then choosing g to be suitably large. Thus, for numerical purposes, we replace the condition on the gradient in (4.11b) with

$$h_x(x_F, t) = g. \tag{4.32}$$

First, we demonstrate here that the use of the condition above will converge towards the limiting case of $g = \infty$. We will then use the results to choose an appropriate case of g to retain accuracy to a given tolerance, which we then use in the implementation of our time-dependent solver.

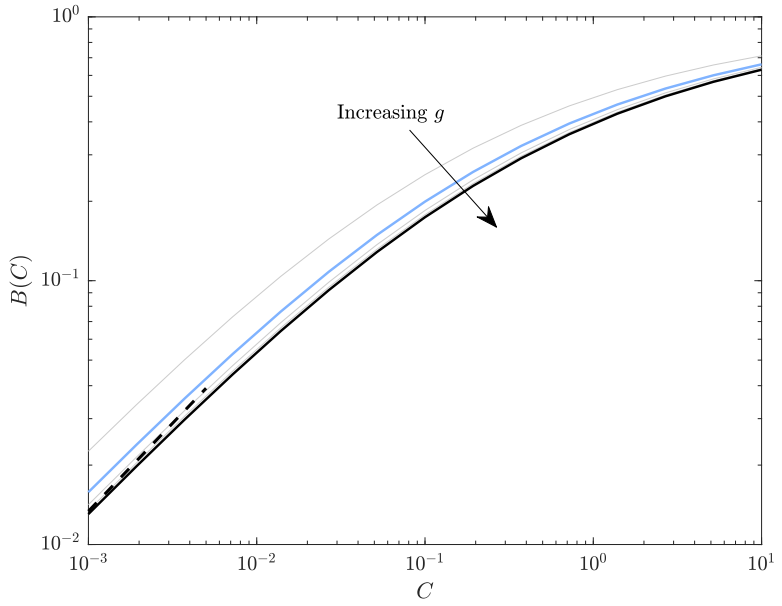

Figure 4.11: Results for the film thickness prediction converge to the Bretherton prediction (black, dashed) as $C \to 0$ for $g \gtrapprox 10$. The black, thick line corresponds to the largest value $g = 50$, and the thick light blue line is the choice of $g = 5$ we use for illustrative results presented in this chapter.

For this test, we consider the predictions of the model in the context of the travelling wave theory of section 4.2.1. To solve the travelling-wave theory, we use the same shooting procedure as in section 4.2.1, but replace the condition on termination with the equivalent of (4.32) in the moving frame, $h_z(0) = g$. In this way, we find the fundamental curve $B(C)$ for a range of specified values of $g = 2, 5, 10, 20, 50$ (figure 4.11). We notice that the prediction of the film

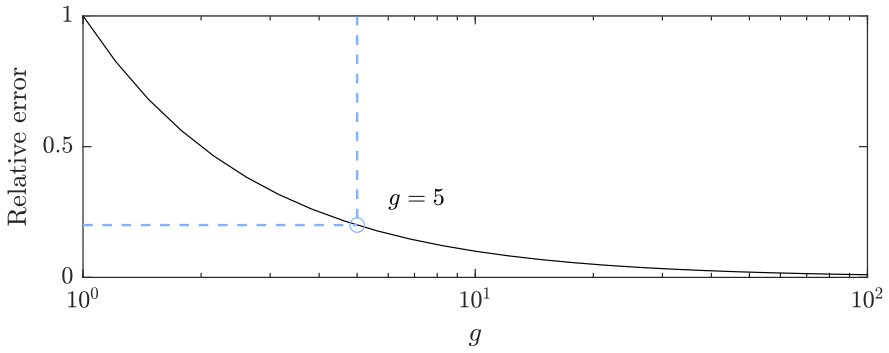

Figure 4.12: The prediction of the coefficient β_g in the analytical equation for dimensionless film thickness $B \sim \beta_g\, C^{2/3}$ approaches the Bretherton prediction as $g \to \infty$.

thickness $B(C)$ converges as the value of g is increased. In particular, for small-C, the prediction recovers the classical analytical prediction of Bretherton (1961) given by (4.22). As confirmation of this convergence, we reformulate the linearised curvature travelling wave system (4.21) such that the matching condition matches to an arc of a circle with a finite gradient g at the nose

$$\tfrac{1}{3}H^3 H_{ZZZ} = H - \beta_g, \tag{4.33a}$$

$$\lim_{Z\to-\infty} H = \beta_g, \qquad \lim_{Z\to\infty} H_{ZZ} = g/(1+g). \tag{4.33b}$$

We solve the system above for a specified value of g using the shooting method for the free parameter β_g as outlined in section 4.2.1. Defining the relative error as $|\beta - \beta_g|/\beta$, where $\beta \approx 1.3375$, the results in figure 4.12 confirm the convergence. We conclude that the approximation of finite nose gradient approaches the predictions of the model with $g = \infty$.

The choice of g for use in our time-dependent implementation is a trade-off between being small enough to be computationally viable, and being large enough to accurately represent the infinite gradient at the nose. For results presented in this chapter, we choose $g = 5$ (light blue, bold in figure 4.11), giving 20% consistency with the prediction of Bretherton limit, for example. With this choice, the bubble nose is approximately semi-circular, as shown in figures 4.1, 4.6, and 4.9.

4A.2 Mapping to a fixed domain

One challenge associated with solving the time-dependent nonlinear curvature lubrication theory (4.10)–(4.12) is the moving boundary at $x_F(t)$ and, in the case of the detached bubble, at $x_R(t)$. To address this, we define $X = x/x_F(t)$ in the case of a continuously injected semi-infinite bubble such that we can now solve the system on the fixed domain $X \in [0, 1]$. Under the coordinate mapping, the system (4.10)–(4.12) becomes

$$h_t = \frac{\dot{x}_F}{x_F} X h_X - \frac{1}{3Cx_F^2}\left(h^3\kappa_X\right)_X, \qquad \kappa = \frac{1}{x_F^2}\frac{h_{XX}}{(1+(h_X/x_F)^2)^{3/2}}, \tag{4.34}$$

subject to boundary conditions

$$h(0,t) = H, \qquad q(0,t) = Q, \tag{4.35a}$$

$$h(1,t) = 1, \qquad h_X(1,t) = gx_F(t), \qquad q(1,t) = Q+1, \tag{4.35b}$$

and kinematic condition

$$\dot{x}_F = 3(Q+1) + \frac{\kappa_{XX}}{3Cgx_F^2} \qquad (X = 1). \tag{4.36}$$

4A.3 Method of lines implementation

We discretise over the spatial domain such that $X_i = (i-1)\Delta X$ for $i = 1, \ldots, N$ with $\Delta X = 1/(N-1)$. A visualisation of the discretisation is shown in figure 4.13, with the circles representing the nodes X_i over which we define the interface $h(X_i) \equiv h_i$. Only the first and last few nodes are shown, as the internal nodes in the centre of the domain are represented in a standard way. The discretisations used for the *edge* nodes near to the outside of the domain ($i = 1, 2, N$, blue) are influenced by boundary conditions.

Rewriting the governing equation (4.34) in terms of the flux q, we obtain

$$h_t = X\left(\frac{\dot{x}_F}{x_F}\right)h_X - \frac{q_X}{x_F}, \qquad q \equiv \frac{h^3}{3Cx_F}\kappa_X. \tag{4.37}$$

Hence, in order to define the time derivative across the domain, we require the first derivative of the flux, which in turn requires calculation of the curvature in order

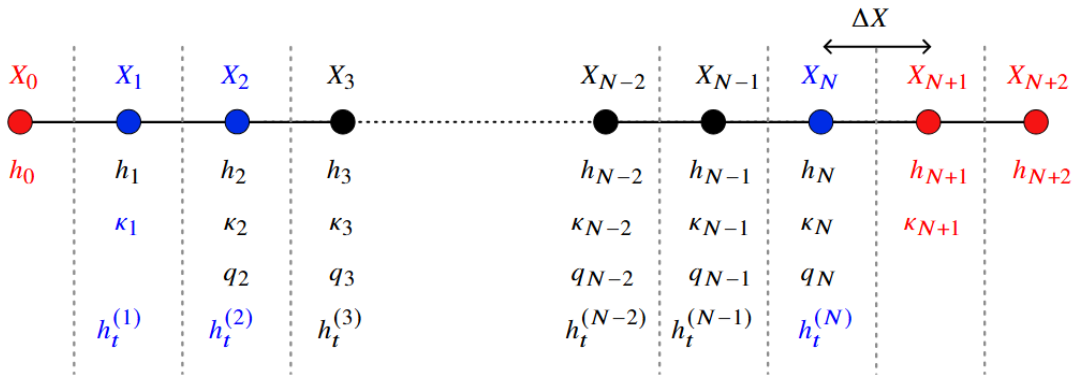

Figure 4.13: The discretisation of the domain in the case of a semi-infinite continuously injected bubble. There are three fictitious ("ghost") nodes X_0, X_{N+1}, X_{N+2} (red) added to extend the domain and allow for application of boundary conditions. Values highlighted in blue are calculated in a special way to either allow for the definition of the ghost nodes, or to impose boundary conditions.

to define the flux itself. In order to explicitly impose the boundary conditions, we place *ghost nodes* that sit outside of the domain $X \in [0, 1]$, shown in red and denoted by X_0, X_{N+1}, X_{N+2} in figure 4.13. Since the governing equation is fourth order and we discretise using centred finite difference approximation, we require the region in which we calculate the time derivative of the interface to be extended by two nodes in each direction. Since the first node is fixed at $h(0,t) = H$, we only add one additional node to the left hand boundary (X_0) and two to the right boundary (X_{N+1}, X_{N+2}) to create an extended domain. The initial condition of the system is a parabola constructed to meet the boundary conditions (4.35), with $x_F(0) = 2(1-H)/g$. The system of ODEs is solved using the stiff integrator `ode15s`. An event function is used to detect pinch-off, causing termination of the integration if the height of the interface reaches $h = 1$ at any interior node.

We begin by considering the internal nodes $(X_3, X_4, \ldots, X_{N-1})$, which are surrounded by at least three nodes on either side. We use finite difference approximations for the spatial derivatives, defined by the centred finite difference

derivatives:

$$\tilde{h}_X^{(i)} = \frac{-h_{i-1} + h_{i+1}}{2\Delta X}, \qquad i = 1, \ldots, N+1, \tag{4.38}$$

$$\tilde{h}_{XX}^{(i)} = \frac{h_{i-1} - 2h_i + h_{i+1}}{(\Delta X)^2}, \qquad i = 1, \ldots, N+1, \tag{4.39}$$

$$\tilde{h}_{XXX}^{(i)} = \frac{-h_{i-2} + 2h_{i-1} - 2h_{i+1} + h_{i+2}}{2(\Delta X)^3}, \qquad i = 2, \ldots, N, \tag{4.40}$$

$$\tilde{h}_{XXXX}^{(i)} = \frac{h_{i-2} - 4h_{i-1} + 6h_i - 4h_{i+1} + h_{i+2}}{(\Delta X)^4}, \qquad i = 2, \ldots, N. \tag{4.41}$$

From (4.37), we can define the governing equation over the internal nodes of the discretised domain as

$$h_t^{(i)} = X_i \dot{x}_F \frac{1}{x_F} \tilde{h}_X^{(i)} - \frac{q_X^{(i)}}{x_F}, \qquad i = 3, \ldots, N-1. \tag{4.42}$$

We require the first derivative of the flux, which is defined as follows

$$q_X^{(i)} = \frac{-q_{i-1} + q_{i+1}}{2\Delta X}, \qquad i = 3, \ldots, N-1. \tag{4.43}$$

The flux, as defined in (4.37), is discretised as follows:

$$q_i = \frac{1}{3C}(h_i)^3 \frac{1}{x_F} \kappa_X^{(i)}, \qquad i = 2, \ldots, N. \tag{4.44}$$

Hence, to calculate the flux across the discretised domain, we require the first derivative of the curvature

$$\kappa_X^{(i)} = \frac{-\kappa_{i-1} + \kappa_{i+1}}{2\Delta X}, \qquad i = 2, \ldots, N. \tag{4.45}$$

Based on (4.10), we define the curvature on the discretised domain as

$$\kappa_i = \begin{cases} \frac{1}{x_F^2} \tilde{h}_{XX}^{(1)} \left(1 + \left(\frac{h_2 - h_1}{x_F \Delta X}\right)^2\right)^{-3/2}, & \text{if } i = 1, \\ \frac{1}{x_F^2} \tilde{h}_{XX}^{(i)} \left(1 + \left(\frac{\tilde{h}_X^{(i)}}{x_F}\right)^2\right)^{-3/2}, & \text{if } i = 2, \ldots, N, \\ \frac{1}{x_F^2} \tilde{h}_{XX}^{(N+1)} \left(1 + \left(\frac{h_{N+1} - h_N}{x_F \Delta X}\right)^2\right)^{-3/2}, & \text{if } i = N+1. \end{cases}$$

The governing equation has now been defined on all internal nodes by (4.42), but in order to define the interface across the edge nodes $i = 1, 2, N$ that make

up the rest of the physical domain, we must now introduce ghost nodes. These nodes sit outside of the physical domain and are used to implement the boundary conditions. Notice that the values of κ_1 and κ_{N+1} are defined using both a centred and a one-sided finite difference. Since these cases are exceptions to the otherwise standard method of defining the curvature using internal nodes, the values are highlighted using colour in figure 4.13.

Defining the edge values of curvature in this way provides an explicit equation for interface at the ghost nodes,

$$h_0 = [\kappa_2 - 6CQx_F\Delta X h_1^{-3}]x_F^2\,(\Delta X)^2\left(1+\left(\frac{h_2-h_1}{x_F\Delta X}\right)^2\right)^{3/2} + 2h_1 - h_2,$$

$$h_{N+1} = h_{N-1} + 2gx_F\Delta X,$$

$$h_{N+2} = [6(Q+1)Cx_F\Delta X + \kappa_N](x_F^2)(\Delta X)^2\left(1+\left(\frac{h_{N+1}-h_N}{x_F\Delta X}\right)^2\right)^{3/2} + 2h_{N+1} - h_N.$$

Finally, we define the governing equation on the remaining edge nodes of the physical domain X_1, X_2 and X_N. Since the left hand boundary is fixed at height $h(0,t) = H$, we define $h_t^{(1)} = 0$. The time derivative at X_2 is defined using a centred finite difference approximation of the flux derivative q_X in (4.37), along with the boundary condition $q = Q$ at $x = 0$:

$$h_t^{(2)} = X_2\left(\frac{\dot{x}_F}{x_F}\right) - \frac{1}{2x_F\Delta X}(Q - q_3), \tag{4.46}$$

with q_3 as defined in (4.44). The time derivative at the only remaining node X_N is defined using the flux condition at the nose

$$q = \frac{1}{3C}h^3\kappa_x = Q + 1. \tag{4.47}$$

Since $h(x_F) = 1$, this implies $\kappa_x = 3C(Q+1)$ at the nose, which can be substituted into the derivative of the flux to obtain

$$q_X^{(N)} = 3h_X(Q+1) + \frac{1}{3Cx_F}\kappa_{XX}. \tag{4.48}$$

Hence, the governing equation in (4.37) becomes

$$h_t^{(N)} = X_N \left(\frac{\dot{x}_F}{x_F} \right) \tilde{h}_X^{(N)} - 3g(Q+1) - \frac{1}{3C} \left(\frac{-\kappa_X^{(N-1)} + \kappa_X^{(N)}}{x_F^2 \Delta X} \right). \tag{4.49}$$

To close the system, the kinematic boundary condition (4.12) is defined as

$$\dot{x}_F = 3(Q+1) + \frac{1}{3Cg(x_F^2)\Delta X} \left(-\kappa_X^{(N-1)} + \kappa_X^{(N)} \right). \tag{4.50}$$

4A.4 Mesh convergence

In order to check that our solutions are fully resolved, we perform resolution sensitivity checks. An example of mesh convergence is shown in figure 4.14. Solutions to the nonlinear curvature lubrication theory (4.10)–(4.12) for the injection of the bubble fluid only ($Q = 0$), fixed input height $H = 0.5$ and capillary number $C = 0.1$ are shown at three different resolutions, corresponding to solutions with $500, 1000$ (shown in blue) and 2000 (black) spatial nodes. Since all three solutions are virtually indistinguishable at each time shown, we can conclude that the solution has converged. If the number of spatial nodes is further decreased, we notice that there is a value of resolution below which the system no longer maintains the constancy of the frontal gradient g.

4A.5 Pinch off

Pinch-off occurs critically at the time t_* when the thickness of the bubble at any position reaches zero, such that $h(x_*, t_*) = 1$, where x_* is the position of pinch-off. After pinch-off, the system is considered in terms of two independent components: the detached bubble, and the remnant between the pinch-off point x_* and the nozzle. At the point of pinch-off, the interface forms a local maximum at x_* (figure 4.6(c)). In order to implement the boundary condition $h_x = \pm g$ at the nose of the remnant and rear of the detached bubble respectively, the solution is truncated either side of the pinch-off point x_* (figure 4.6(e)). For the remaining remnant, we continue the existing integration by moving the front to the pinch-off position, $x_F(t_*) = x_*$, which initialises a new cycle of growth and pinch-off.

For the detached bubble component, there are now two moving boundaries: one at the front of the bubble, $x_F(t)$, and one at the rear, $x_R(t)$. To map the system to a fixed domain, $X \in [0,1]$, we define a new coordinate

$$X = \frac{x - x_R(t)}{x_F(t) - x_R(t)}. \tag{4.51}$$

The governing equation (4.10) then takes the form

$$h_t = \left(\frac{X\dot{x}_F}{x_F - x_R} - \frac{(X-1)\dot{x}_R}{x_F - x_R}\right) h_X - \frac{1}{3C(x_F - x_R)} \left(h^3 \left(\frac{1}{(x_F - x_R)}\kappa_X\right)\right)_X,$$

with the following boundary conditions

$$h(0,t) = 1, \qquad h_x(0,t) = -g, \qquad q(0,t) = 1, \tag{4.52}$$

$$h(1,t) = 1, \qquad h_x(1,t) = g, \qquad q(1,t) = 1, \tag{4.53}$$

along with two associated kinematic conditions

$$\dot{x}_R = 3 - \frac{\kappa_{XX}}{3Cgx_F^2}, \qquad (X = 0), \tag{4.54}$$

$$\dot{x}_F = 3 + \frac{\kappa_{XX}}{3Cgx_F^2}, \qquad (X = 1). \tag{4.55}$$

Since the boundary is no longer fixed at the left hand side of the domain, we require two ghost nodes at each end of the domain. Either end of the domain for the finite bubble is treated like the moving boundary at the nose in the case of a semi-infinite bubble.

4A.6 Bubble volume

For mass to be conserved, the volume of the bubble must grow linearly in time to satisfy

$$V = V_0 + t, \tag{4.56}$$

where V_0 is the initial volume of the bubble at $t = 0$. In two dimensions, the bubble "volume" is equivalent to the area of the bubble which can be calculated using numerical integration. The evolutions of the bubble area with time, for the examples of bubble generation shown in figures 4.6 and 4.9, are shown in figure 4.15, providing numerical validation of the consistent, linear increase in bubble volume with time required by (4.56).

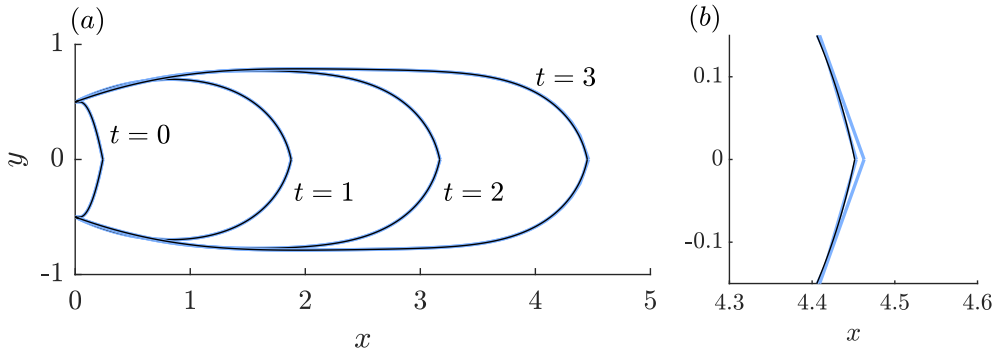

Figure 4.14: (a) An example of mesh convergence with $C = 0.1$ and $Q = 0$. Solutions with $500, 1000$ (blue) and 2000 (black) nodes are shown at four times. (b) shows the same solutions as in (a), zoomed in at the nose. The solutions overlap almost exactly, demonstrating convergence with mesh resolution.

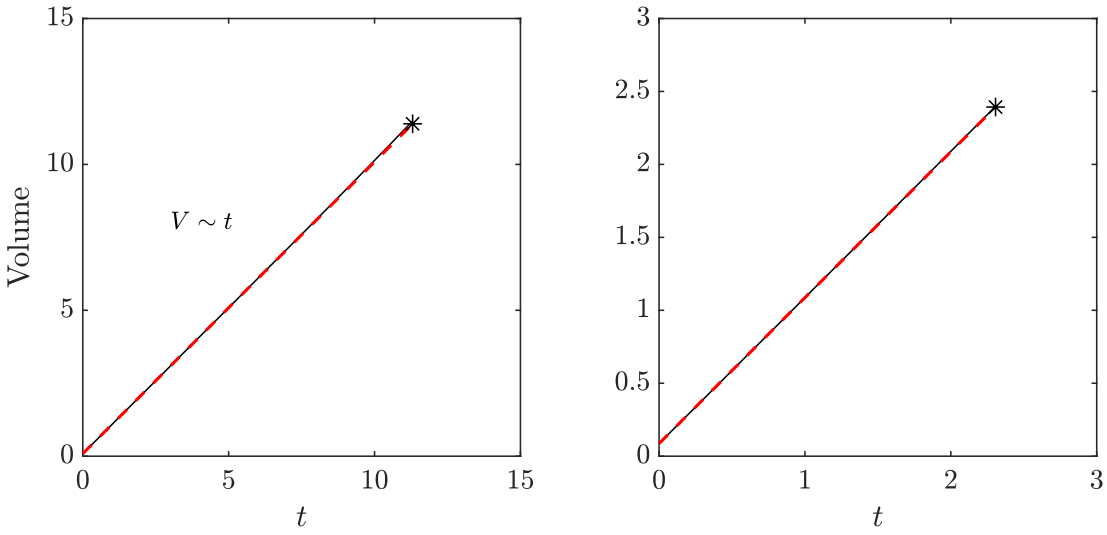

Figure 4.15: The volume of the bubbles shown in figure 4.6 ($Q = 0.2$, left) and in figure 4.9 ($Q = 3$, right) are plotted against time. The volume of each bubble grows linearly with time, providing validation of the bubble volume constraint (4.56).

Chapter 5

Theory of Taylor bubble pinch-off in axisymmetric capillary tubes

When a gas is injected into a capillary tube filled with an immiscible fluid, a bubble forms that progresses through the tube surrounded by a thin viscous film. The dominant regime observed in two-phase flows driven by surface tension is the Taylor bubble flow regime, consisting of elongated capsular bubbles that are much longer than the diameter of the tube separated by regular liquid slugs (Triplett *et al.*, 1999; Yue *et al.*, 2008). Compared with single-phase flow, the introduction of Taylor bubbles can increase heat and mass transfer by causing recirculation in the liquid slugs (Asadolahi *et al.*, 2012; Bercic & Pintar, 1997). Cubaud *et al.* (2005) provides an experimental investigation into the formation of Taylor bubbles in a cross-flow geometry formed of square microchannels joined perpendicularly to one another. The liquid phase (water) is introduced through two microchannels placed opposite to one another at either side of the main channel through which the gas phase (air) is introduced. An empirical expression for the length of the Taylor bubble L_B, normalised by the square channel width w, is obtained as

$$\frac{L_B}{w} = \frac{q_c + q_d}{q_c}, \tag{5.1}$$

where q_c and q_d are the volumetric flow rates of the liquid and gas phases respectively. The empirical scaling law has also been observed experimentally for Taylor bubble formation in a T-junction (Garstecki *et al.*, 2006), and a co-flowing

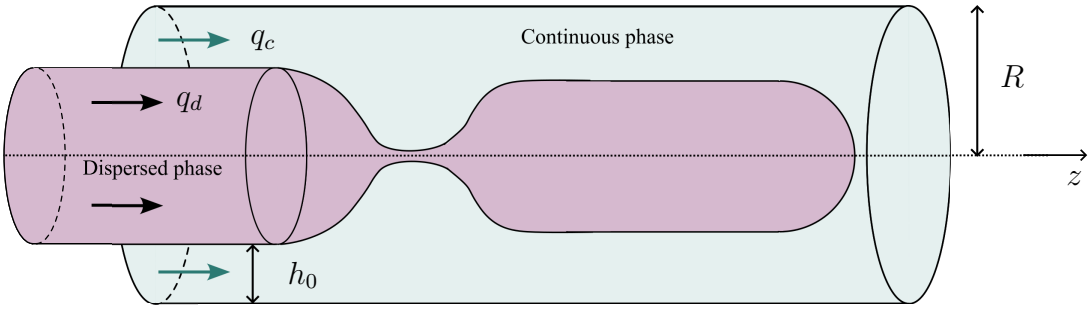

Figure 5.1: A schematic of coflow injection in an axisymmetric capillary tube of circular cross section and radius R. The flow is symmetric about the centreline so that only one half of the tube needs to be considered. The fluxes of the bubble fluid (dispersed phase) and viscous fluid (continuous phase) are specified as q_d and q_c respectively.

device of rectangular cross-section (Xiong *et al.*, 2007). Currently, no mathematically derived theoretical law exists to validate these experimental observations. Existing scalings are determined from experimental observations and are therefore very sensitive to their own data sets. Whilst numerical simulations have corroborated experimental scaling laws (e.g. Cubaud *et al.*, 2005; Jensen *et al.*, 2006), a detailed mathematical analysis and explanation of the observed results is as yet unavailable. Here, we provide the first mathematical model of injection-driven pinch-off in an axisymmetric coflow geometry, introducing a quasi-static modelling approach to theoretically derive predictions for bubble pinch-off time t_* which are compared with existing experimental scaling laws. In contrast to the planar configuration considered in chapter 3, we find that the new azimuthal curvature contribution introduced in an axisymmetric geometry fundamentally changes the pinch-off behaviour. The key result of the analysis is to derive from first principles the $t_* \sim 1/q_c$ scaling law indicated by experiments (Cubaud *et al.*, 2005; Garstecki *et al.*, 2006; Xiong *et al.*, 2007).

In this chapter, we analyse bubble formation in an axisymmetric geometry (figure 5.1), revealing fundamentally new considerations in the determination of the interface shape in comparison to the planar case considered in chapter 3. We discover that pinch-off is no longer entirely controlled by a quasi-static solution, and there instead exists a critical point at which quasi-static shapes cease to exist.

This is instead the condition that controls bubble pinch-off in an axisymmetric geometry as, beyond this point, the bubble pinches off rapidly. In turn, we show that there are two modes describing the breakdown of quasi-static solutions: quasi-static solutions can be lost due to a constraint on the maximum volume of the necking disturbance, or a constraint on the maximum length. In the volume-limited regime, bubble formation time t_* is inversely proportional to input flux q_c with a prefactor determined by the breakdown of quasi-static solutions, providing the first theoretical explanation of this law which to date has only been proposed empirically.

There is extensive existing literature on the different but related problem of surface-tension-driven flow of a viscous film coating the interior of a capillary tube. The transition between annular flow, where the fluid film lines the interior of a capillary tube, and the plug regime, where the liquid lining grows to obstruct the channel, is governed by the channel occlusion phenomenon. This phenomenon is observed in industrial applications including oil recovery, microfluidic applications and medical studies into airway closure (Dietze, 2024; Grotberg, 1994; Heil & White, 2002). The fluid film lining the capillary tube is unstable subject to the surface-tension driven Rayleigh-Plateau instability (Plateau, 1873; Rayleigh, 1878) as perturbations can result in a favourable net decrease of surface energy. As the fluid film grows, the bubble thins and the azimuthal curvature contributions become dominant and destabilises the film. The same is not true in the two-dimensional limit, where the analogous bubble is stable as comparable perturbations result in an increase in surface area (Migler, 2001; San Miguel *et al.*, 1985). In an axisymmetric geometry, the Laplace pressure instigates the flow of liquid from regions where the curvature is higher, towards a bulged area where the curvature is lower, causing the bulge to grow and form a plug that can block the capillary. Everett & Haynes (1972) obtained a threshold value of film thickness, demonstrating that channel occlusion is only possible when the volume of the surrounding fluid is sufficiently large. Below this volume, the film takes an unduloidal shape and does not obstruct the capillary. Hammond (1983) proposed a lubrication model under the assumption that the fluid film is thin to model the evolution of a film lining the interior of a capillary tube. Whilst the model was able to predict the formation of collars, it could not model the emergence of the

plug regime that is associated with sufficiently thick films. To expand upon this model, Gauglitz & Radke (1988) account for the azimuthal contributions to mass conservation in the lubrication framework and were able to determine a critical thickness value beyond which the liquid collar becomes unstable and develops to a plug.

During our analysis into Taylor bubble pinch-off in an axisymmetric geometry, we make a connection to static menisci between two discs. The Young-Laplace equation can be used to analyse the stability of static meniscus shapes at instantaneous times. This approach is commonly used to study the stability of a liquid bridge between two circular discs (e.g. Gillette & Dyson, 1971; Mason, 1970; Russo & Steen, 1986; Sanz & Martinez, 1983; Slobozhanin *et al.*, 1995), and by coupling equilibrium solutions given by the Young-Laplace equation to an equation for contact line motion, the dynamic behaviour of a fluid film can be analysed (Bonn *et al.*, 2009). Static solutions with specified, fixed surface tension are shapes of constant mean curvature (Delaunay, 1841) and the family of solution shapes can be parameterised by the characteristic length scale and volume enclosed by the surface. It is possible that two distinct solutions can satisfy the specified conditions on length and volume; both a stable, slender bridge and a strongly necked unstable bridge are possible. Within a family of solutions of the Young–Laplace equation, there exists a critical point beyond which static equilibrium solutions of the system cannot exist (Everett & Haynes, 1972). This behaviour was apparent in the study of Lv & Hardt (2021), who considered the static behaviour of a liquid ring surrounding another immiscible fluid within a capillary tube. By finding solutions to the axisymmetric Young-Laplace equation for an arbitrary contact angle, Lv & Hardt (2021) determined the criteria to define a stable regime, outside of which liquid rings cease to exist and are instead replaced by plugs or a sessile droplet.

Zhao *et al.* (2018) uses a lubrication framework with linearised curvature to model the fluid-fluid interface when a viscous fluid is displaced from a circular capillary tube by a less viscous fluid in the partial wetting regime. The system is initialised in a partially wetting regime and only transitions to a state of complete wetting when the capillary number increases beyond a critical value. At this critical point, the apparent contact angle becomes zero, meaning that the air

finger passes through the centre of the tube and is surrounded by a thin film. The thickness of the entrained liquid film depends on the finger tip velocity, providing a matching condition for the necking system. The growth of the fluid film in the necking region is initially linear in time, but accelerates at later times when the large azimuthal curvature results in a dominance of the Rayleigh-Plateau instability. The configuration considered by Zhao *et al.* (2018) differs from the system considered here, where the input nozzle fixes the height of the fluid film at $z = 0$, and both the fluids are injected at a constant flow rate.

In this chapter, we provide the first theoretical explanation of experimentally observed scaling laws for Taylor bubble formation. Whilst the configuration considered in this thesis is not exactly identical to the geometries considered in existing experimental work, the scaling law has been confirmed in a range of geometries (e.g. Cubaud *et al.*, 2005; Garstecki *et al.*, 2006; Jensen *et al.*, 2006; Xiong *et al.*, 2007). To date, there is no mathematical analysis to provide justification for the scaling law in any geometry, and therefore we choose to consider a coflow configuration as the most simple option. In section 5.1, we begin by deriving the model to describe pinch-off in an axisymmetric geometry that is based on the same matching of a necking disturbance to a downstream Taylor bubble as was used in chapter 3. We present illustrative solutions to the system in section 5.2, demonstrating the progression towards pinch-off and the initially quasi-static structure. A corresponding quasi-static theory to describe this evolution is derived in section 5.3.1, and we notice that the solutions are considerably more complex than the parabolic quasi-static states analysed in the planar geometry. An asymptotic analysis of the quasi-static solutions in section 5.4 yields explicit analytical predictions for the pinch-off time in the limit of small capillary number. We conclude by comparing our predictions to existing experimental observations and empirical scaling laws.

5.1 Theoretical development

We consider an axisymmetric capillary tube with circular cross-section of uniform radius R (figure 5.1). The capillary is filled with a viscous fluid of dynamic viscosity μ, which flows at a prescribed volumetric flux q_c. Interior to the capillary,

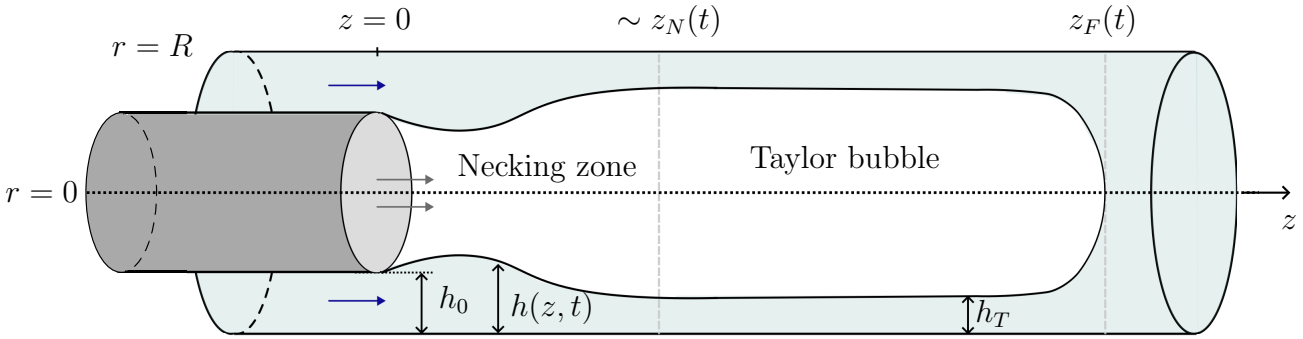

Figure 5.2: Schematic representing the asymptotic structure of a Taylor bubble formed by injection via a nozzle. The flow structure can be divided into two regions: i) the necking region where the fluid film thickens locally in the vicinity of the input nozzle, and ii) the Taylor bubble region comprising an approximately circular front connected to a region of near uniform film thickness.

an inviscid fluid is injected coaxially in a *coflow* configuration at a constant volumetric flux q_d and the system is symmetric about the centreline of the pipe. We note that there is a notational difference here (cf. chapters 3 & 4), and q now represents a three-dimensional volume flux. Defining the height of the film at the input as $h(0,t) = h_0$, the distance between the circumference of the input nozzle and the surrounding pipe wall is $(R - h_0)$. When $q_c > 0$, the configuration provides a canonical example of a system that undergoes periodic pinch-off, producing a train of bubbles at a controlled frequency.

The input conditions at the nozzle for a coflow system are specified as

$$h(0,t) = h_0, \qquad q(0,t) = q_c, \tag{5.2}$$

such that the height of the interface $h(z,t)$ is fixed at the nozzle. Our analysis of the corresponding planar version of the coflow configuration in chapter 3 showed that Taylor bubbles (of much longer dimension than their width) are generated when the bubble injection flux is much greater than the flux of the outer fluid ($q_c \ll q_d$). In this situation, the flow can be considered in two regions: a *Taylor bubble*; and a *necking zone*, with the latter connecting the back of the Taylor bubble to the input nozzle (figure 5.2).

5.1.1 The Taylor bubble

In section 3.1.1, we discussed the structure of a Taylor bubble in a planar configuration. We now address the Taylor bubble in an axisymmetric configuration, which has an asymptotic structure of a hemi-spherical nose region coupled to a region of uniform film thickness and zero flux upstream of the nose. The size of the film thickness surrounding a Taylor bubble was shown to depend crucially on the capillary number, which is defined as

$$C = \frac{\mu q_d}{\gamma R^2}, \tag{5.3}$$

and differs in form from the planar case (3.3) by an extra factor of R on the denominator due to the integration around the circumference of the axisymmetric capillary. Since the curvature of the cap contributes only a longitudinal curvature in either the two-dimensional (circular) case, or the axisymmetric (spherical) configuration, the expression for uniform film thickness derived by Bretherton (1961)

$$\frac{h_T}{R} \sim 1.3375\, C^{2/3} \equiv B(C) \qquad (C \to 0), \tag{5.4}$$

holds in both geometries in the small capillary number limit (Ratulowski & Chang, 1989; Schwartz *et al.*, 1986).

As in the planar configuration, the viscous stresses at the front of the bubble gain importance at moderate to large capillary number. Reinelt & Saffman (1985) considered the free boundary problem for the steady-state shape of a Taylor bubble and presented numerical solutions to the Stokes equations in both a two-dimensional and an axisymmetric geometry, highlighting only a small difference in the width of the bubble as $C \sim O(1)$. The numerical results in the axisymmetric configuration are shown in figure 5.3, exhibiting excellent agreement with the experimental results of Taylor (1961). The analytical function

$$B(C) = \frac{1.3375}{3.3 + C^{-2/3}} \tag{5.5}$$

plotted as a black, solid curve in figure 5.3 provides an accurate representation of both the experimental findings of Taylor (1961) and the numerical results of Reinelt & Saffman (1985), as well as the asymptotic result of Bretherton (1961)

as $C \to 0$. The fitted function (5.5) differs slightly from its planar analogue (3.6) shown in figure 3.2. The interior thickness provides a matching condition on the downstream limit of the necking zone, which avoids the need to solve for the moving nose position of the bubble.

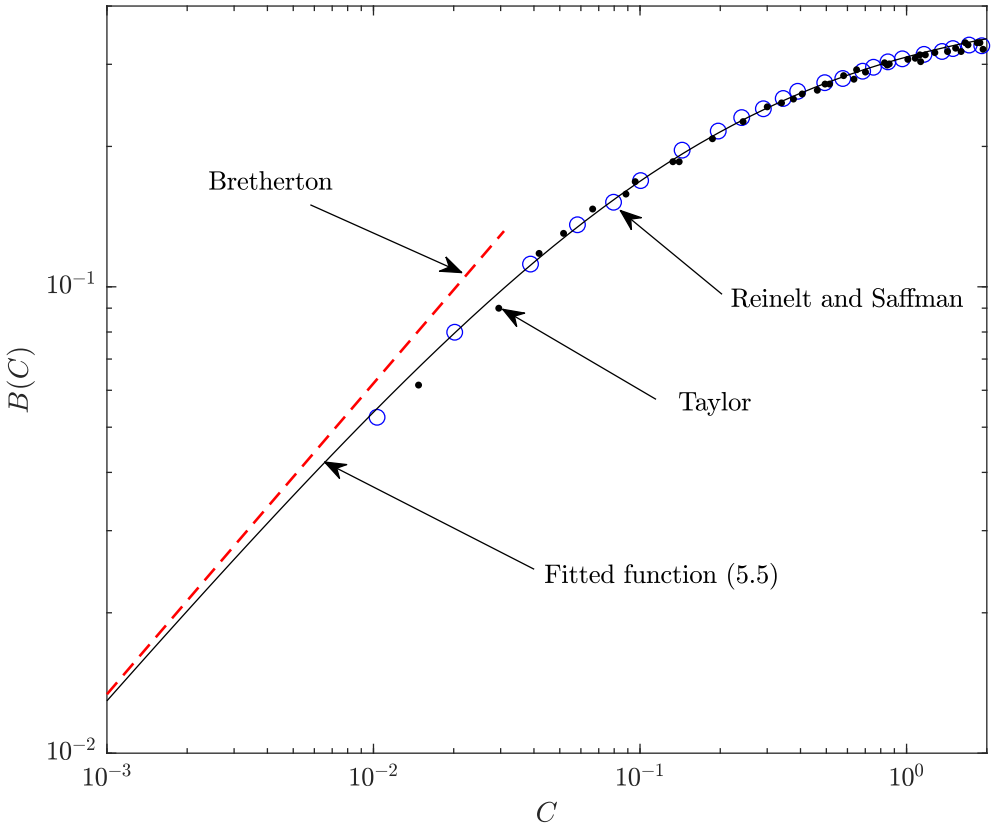

Figure 5.3: The universal function $B(C)$ giving the film thickness as specified by the expression (5.5) chosen to fit the experimental results of Taylor (1961) and the numerical results of Reinelt & Saffman (1985) in a cylindrical capillary. The function exhibits good agreement with the small-C limit of (5.4).

5.1.2 The necking zone

Similarly to the planar configuration considered in section 3.1.2, we define the necking zone as the region lying between the injection nozzle and the interior of the Taylor bubble (figure 5.2), $0 \leq z \lesssim z_N(t)$, where $z_N(t)$ is a time-dependent

characteristic scale of the developing necking disturbance to be predicted. We assume that the film approaches a constant value far downstream of the injection point, and match the necking zone solution to the *interior thickness* of the fluid film surrounding the Taylor bubble

$$\lim_{z\to\infty} h = h_T. \tag{5.6}$$

Zhao *et al.* (2018) similarly employed the Taylor bubble thickness as a boundary condition in their related study of pinch-off in an axisymmetric capillary tube. Zhao *et al.* (2018) also considered immiscible gas-liquid displacement in a capillary, but in the context of a wetting transition. The tube is initially filled with glycerol that partially wets the capillary, and is subsequently withdrawn from one end of the tube upon application of a negative pressure gradient. Air is drawn in from the opposite, open end of the tube to replace the glycerol, forming a Taylor bubble. The study has similar elements to the coflow injection considered in this thesis, such as the formation of both a region of localised necking and a Taylor bubble. The configuration differs as the contact line recedes as the dewetting rim grows, rather than being fixed at an input nozzle, and the volume of the fluid film cannot be attributed to the injection of the continuous phase, but instead its growth is given by the velocity of the receding contact line. The long-wave approximation with linearised curvature was used to describe the dynamics of a dewetting rim in an axisymmetric capillary tube, with (5.6) prescribed as a boundary condition, giving precedence for the modelling approach presented in this section.

We use a cylindrical coordinate system (r, θ, z) coaxial with the tube and assume that the flow is independent of the angular coordinate θ. Considering the outer fluid which surrounds the bubble, the lubrication approximation simplifies the Stokes equations to the two equations

$$\frac{\mu}{r}\left(r u_r\right)_r = p_z, \qquad p_r = 0, \tag{5.7a-b}$$

where $u(r, z, t)$ is the longitudinal velocity of the viscous fluid, $p(r, z, t)$ is the pressure field of the viscous fluid, and we use subscripts to denote partial derivatives. We apply the following boundary conditions on the capillary wall, $r = R$,

and bubble interface $r = R - h(z,t)$

$$u(z,R,t) = 0, \qquad u_r(z,R-h,t) = 0, \qquad [p]_{R-h_-}^{R-h_+} = -\gamma\kappa, \tag{5.8a-c}$$

where

$$\kappa = \frac{h_{zz}}{(1+h_z^2)^{3/2}} + \frac{1}{(R-h)(1+h_z^2)^{1/2}} \tag{5.9}$$

is the interfacial curvature, and γ is the interfacial surface tension. In contrast to the planar geometry, we will show that, owing to differences in how the developing necking disturbance evolves, it is crucial to retain the full nonlinearised curvature expression in the axisymmetric configuration. The expression for curvature also contains an additional term that stems from azimuthal (hoop) contributions in the axisymmetric geometry. As the height of the fluid film approaches the radius of the tube (corresponding to a zero bubble thickness), the azimuthal curvature inevitably becomes leading order, resulting in intrinsically different behaviour to the planar configuration.

The normal stress balance at the interface is derived by integrating (5.8*b*) subject to the jump condition (5.8*c*), giving the Young-Laplace equation

$$p = p_0 - \gamma\kappa, \tag{5.10}$$

where p_0 is an arbitrary constant reference pressure dependent on, for example, the pressurisation at the nozzle or pressure inside a released closed bubble (owing to the assumed incompressibility of the fluids, p_0 will have no effect on the dynamics of the problem). Integrating (5.7a) twice and applying the boundary conditions (5.8*a*, *b*), we obtain

$$u = \frac{1}{4\mu} p_z \big(r^2 - R^2 + 2(R-h)^2(\log R - \log r)\big). \tag{5.11}$$

In contrast to the planar geometry, volume flux in an axisymmetric configuration is determined by a volume of revolution

$$\bar{q} = \int_0^{2\pi} \int_{R-h(z,t)}^{R} u\, r \, \mathrm{d}r \, \mathrm{d}\theta, \tag{5.12}$$

and we can define a scaled volume flux $q \equiv \bar{q}/2\pi$ for mathematical brevity as

$$q = \frac{\gamma\kappa_z}{16\mu}(R^4 + 3(R-h)^4 - 4(R-h)^2R^2 - 4(R-h)^4(\log(R-h) - \log R)).$$

Substituting the scaled volume flux into the continuity equation $h_t = -q_z/(R-h)$, we obtain an equation for the fluid film height h as

$$\frac{\partial h}{\partial t} = -\frac{1}{R-h}\frac{\partial}{\partial z}\left(\kappa_z F(h)\right), \quad \kappa = \frac{h_{zz}}{(1+h_z^2)^{3/2}} + \frac{1}{(R-h)(1+h_z^2)^{1/2}}, \quad (5.13a\text{-}b)$$

where

$$F(h) \equiv \frac{\gamma}{16\mu}\left(R^4 + 3(R-h)^4 - 4(R-h)^2R^2 - 4(R-h)^4(\log(R-h) - \log R)\right).$$

The system of equations (5.13) describing the evolution of a thin film coating an axisymmetric capillary tube in a coflow configuration differs from the analogous planar system in numerous ways. The governing equation (5.13a) contains a prefactor of $1/(R-h)$ which leads to the formation of a gradient jump $h \to R$ and the coefficient approaches infinity. Another crucial contrast to the planar geometry is the additional azimuthal curvature term in (5.13b) that arises only in the axisymmetric geometry and results in a more rapid acceleration towards pinch-off (as will be observed in section 5.2). As the radius of the bubble thins to zero ($h \to R$), the stronger capillary pressure attributed to the azimuthal curvature pulls liquid in the fluid film more strongly towards the necking region, resulting in accelerated thinning of the bubble neck. Additionally, in contrast to the planar case, we retain the full nonlinear expression for curvature. Travelling wave forms of the same nonlinear curvature lubrication equations were studied by Ratulowski & Chang (1989) in the context of finite Taylor bubbles migrating through cylindrical capillaries. The focus of Ratulowski & Chang (1989) was computation of the pressure drop and uniform film thickness, whereas this thesis focuses on the pinch-off dynamics of a coflow system.

The equation above is fourth order in space, requiring a total of four boundary conditions to close the system. The downstream matching condition (5.6) provides a boundary condition on both the film height and its gradient, while the conditions at the input nozzle (5.2) constitute the remaining two boundary conditions required to solve the fourth-order governing equation. For conformity with (5.6), we initialise the system as a thin film of constant thickness

$$h(z,0) = h_T. \quad (5.14)$$

At the critical time t_* defined by

$$h_m(t_*) \equiv \max_z \left(h(z, t_*)\right) = R, \tag{5.15}$$

the viscous fluid spans the width of the channel, defining the pinch-off of the Taylor bubble. The focus of our analysis will be to understand the dependence of pinch-off time t_* on the system parameters.

5.1.3 Dimensionless system

To obtain a dimensionless system for the axisymmetric geometry we introduce the following variables

$$z = R\hat{z}, \qquad h = R\hat{h}, \qquad q = q_d\hat{q}, \qquad t = \frac{R^3}{q_d}\hat{t}. \tag{5.16}$$

In contrast to the analogous nondimensionalisation for the planar geometry (section 3.1.3), both length scales of the system are equal; the horizontal and the vertical lengths are now scaled by the radius of the capillary tube R. On dropping hats, the governing equation (5.13) becomes

$$\frac{\partial h}{\partial t} = -\frac{1}{C(1-h)}\frac{\partial}{\partial z}\left(\kappa_z F(h)\right), \quad \kappa = \frac{h_{zz}}{(1+h_z^2)^{3/2}} + \frac{1}{(1-h)(1+h_z^2)^{1/2}}, \tag{5.17}$$

for flux $q = (1/C)\kappa_z F(h)$, where C is a capillary number, as defined in (5.3), and

$$F(h) = \frac{1}{16}\left(1 + 3(1-h)^4 - 4(1-h)^2 - 4(1-h)^4\log(1-h)\right) \tag{5.18}$$

is an increasing function of film thickness with the limiting properties $F(h) \sim h^3/3$ as $h \to 0$ and $F(1) = 1/16$. Hence, in the thin-film limit $h \to 0$, the governing equation (5.17a) reduces to the planar case considered in section 3.1.3, but the curvature expression (5.17b) differs in the axisymmetric case due to the retention of nonlinearity and the additional azimuthal curvature contribution.

The boundary conditions at the input nozzle (5.2) and the downstream matching condition (5.6) become

$$h(0,t) = H, \qquad q(0,t) = Q, \tag{5.19a}$$

$$\lim_{z\to\infty} h = B, \tag{5.19b}$$

where $H = h_0/R$ represents a ratio of the inlet nozzle radius to the pipe radius, $Q = q_c/q_d$ is the ratio of the liquid (continuous phase) flux to the inviscid fluid (dispersed phase) flux, and $B = h_T/R$ is the ratio of the interior film thickness of the Taylor bubble to the capillary tube radius R. The initial condition (5.14) becomes

$$h(z, 0) = B, \tag{5.20}$$

and the pinch-off criterion (5.15) becomes

$$\max_z(h(z, t_*)) = 1. \tag{5.21}$$

The equation (5.17) along with boundary conditions (5.19) together form a closed system for the dynamics in the necking zone region in the vicinity of the input nozzle under the assumption that a Taylor bubble forms downstream. Under this assumption, the system describes the development of the film towards a uniform film thickness B and, in the context of injection into a pipe, B is a direct function of C. Therefore, the specified parameters of the necking zone system are C, Q and H in the pipe flow configuration considered here. The capillary number C represents the balance of viscous and surface tension forces, and also controls the value of B representing the thickness of the film surrounding the bubble. Small capillary numbers ($C \lessapprox 0.01$) are usually considered such that the flow is dominated by surface tension and the film around the bubble is thin. The remaining two parameters are the flux ratio Q and the ratio of the film thickness at the inlet to the radius of the capillary H. The value of H is restricted to the range $0 < H < 1$; a value close to zero represents a nozzle that occupies most of the pipe. Whilst the flux ratio can take any value in principle, it is often restricted in the range of $0.01 \lesssim Q \lesssim 10$ in experimental studies (Cubaud *et al.*, 2005; Garstecki *et al.*, 2006; Xiong *et al.*, 2007). In the context of Taylor bubble formation specifically, the condition $Q \ll 1$ is necessary in order to employ the matching condition to the region of uniform film thickness associated with the formation of Taylor bubbles. We note that the cylindrical capillary geometry considered here is approximately equivalent to a channel of square cross section as both configurations allow for the fluid to be confined as a cylinder (Cubaud *et al.*, 2005).

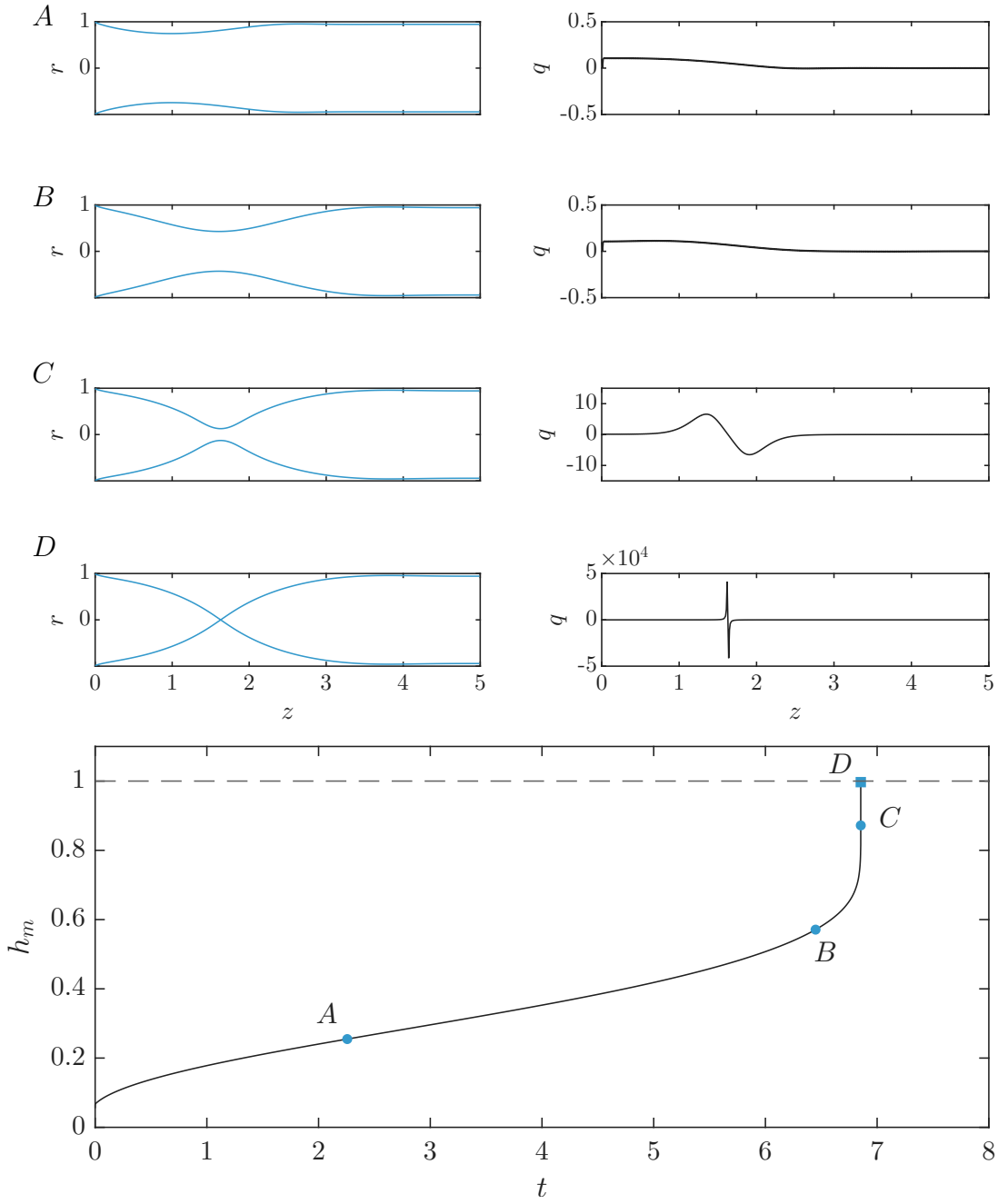

Figure 5.4: The time-dependent solution to the governing equation (5.17) with the boundary conditions of the necking zone (5.19) and parameters $C = 0.01$, $Q = 0.1$ and $H = 0.01$ (left column). The right column shows the corresponding flux at each chosen time. The maximum height of the fluid film $h_m(t)$, shown in the lower panel, grows consistently up until just before pinch-off, where the increase is rapid and the flux increases. The final time solution, shown in panel D, corresponds to the pinch-off time t_*.

5.2 Mathematical analysis

In order to analyse the dynamics of bubble pinch-off, we consider solutions to the time-dependent necking zone system as defined by the governing equation (5.17) and the boundary conditions (5.19). An example of the time-dependent interface evolution is shown in the left-hand column of figure 5.4 for a choice of parameters $Q = 0.1, H = 0.1$ and $C = 0.01$. A selection of plots are shown from a time series to demonstrate the evolution of the fluid-fluid interface up to the point of pinch-off. The thickness of the surrounding fluid film increases with time, illustrating the necking phenomenon. The corresponding flux for each example solution shown is plotted in the right hand column. At early times, the solutions A and B have extremely small fluxes that appear to be approximately zero. In the time between B and C, the flux has increased substantially, indicating a significant change in the evolution between these two times. At the pinch-off time shown in D, we recover a singularity associated with a film thickness $h = 1$. In order to visualise evolution towards pinch-off, a plot showing the progression of the maximum film thickness with time is given in figure 5.4. The maximum film thickness at a given time $h_m(t)$ has an initial period of gradual growth, before exhibiting rapid acceleration beyond $t \approx 7$ up until the point of pinch-off $t_* \approx 7.37$, where $h_m(t_*) = 1$.

Zhao *et al.* (2018) experimentally observed a similar, initially regular growth of the maximum thin film thickness (cf. figure 4(b) Zhao *et al.* (2018)), followed by a region of accelerated growth towards bubble pinch-off. Pahlavan *et al.* (2019) theoretically investigated the nonlinear acceleration of the maximal film thickness close to pinch-off and derived a scaling law for the bubble neck diameter in the times just prior to pinch-off. Specifically, Pahlavan *et al.* (2019) determines that the bubble neck radius ($r_0 \equiv (1 - h_m)$) follows a $\tau^{1/5}$ scaling in the approach to pinch-off, where $\tau = t_* - t$ is the remaining time until pinch-off at t_*. Figure 5.5 demonstrates that the maximal film thickness shown in the lowest panel of figure 5.4 is consistent with this $\tau^{1/5}$ scaling as pinch-off is approached. The "late-time" regime of Pahlavan *et al.* (2019) very close to pinch-off (which follows a linear scaling in τ) is not captured here as the lubrication theory cannot capture the full Stokes effects in this region. This nonlinear collapse was not evident in the

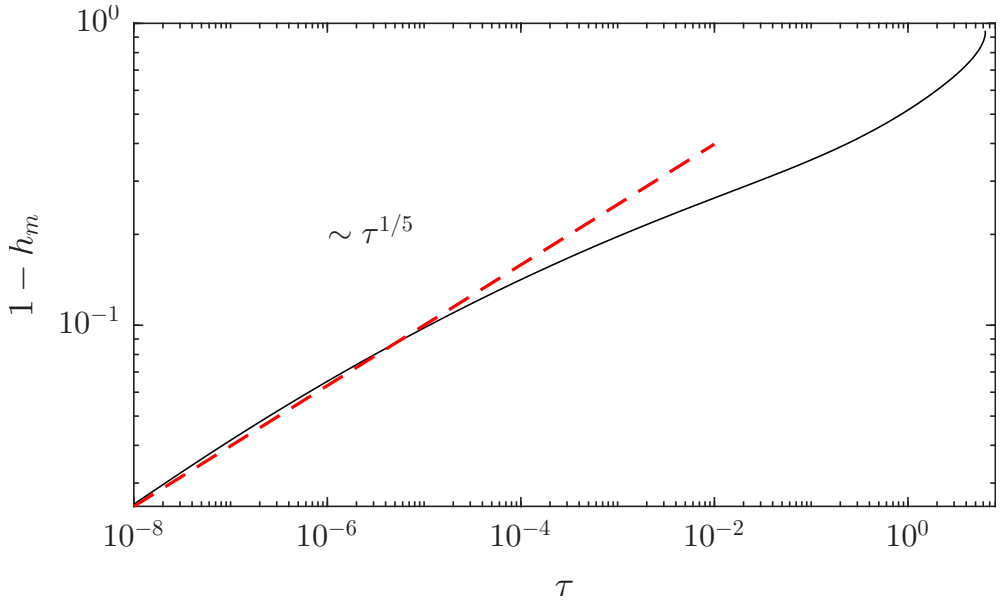

Figure 5.5: Evolution of the bubble neck radius versus remaining time to pinch-off $\tau = t_* - t$. The $\tau^{1/5}$ scaling law of Pahlavan *et al.* (2019) is captured in the approach to pinch-off $\tau \to 0$.

two-dimensional geometry considered in chapter 3, and so axisymmetric bubble pinch-off requires an entirely new asymptotic analysis. We will find that this acceleration towards bubble pinch-off can be attributed to a loss of quasi-static solutions to the necking disturbance.

Figure 5.6 shows the time for bubble pinch-off obtained when solving the necking zone system for a range of input flux ratios Q and capillary number C, with $H = 0.01$ fixed. The solutions become harder to resolve for smaller capillary number C due to the large transition at the head of the necking disturbance, and so we limit the results to the range $C = 0.0025$ to $C = 0.02$. The dimensionless pinch-off time decreases with an increase in the fluid flux ratio, and for small capillary number we observe an inverse linear power law trend $t_* \sim 1/Q$. In particular, as $C \to 0$, the results converge towards a linear trend represented by $t_* \sim 0.8672/Q$. When capillary number is larger, the relationship $t_* \sim 1/Q$ is observed only for larger Q and, as the fluid flux ratio decreases, we notice a flattening of the curve. However, the capillary number is typically small ($C < 10^{-2}$) when considering flow in microchannels (Garstecki *et al.*, 2006), and therefore we

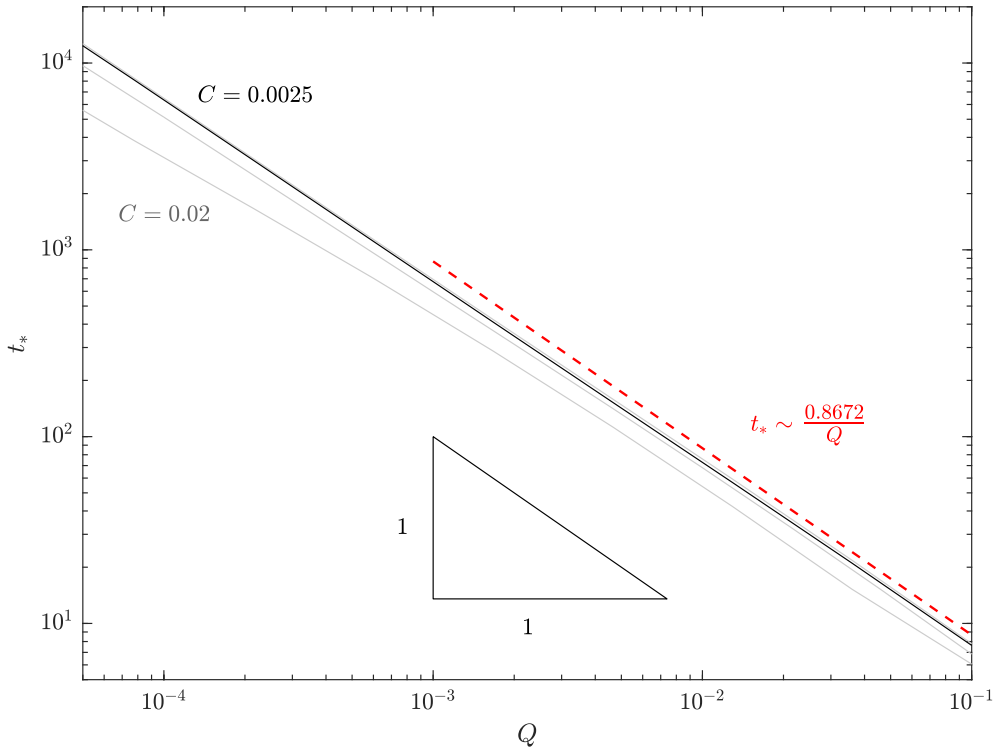

Figure 5.6: The numerical prediction for pinch-off (solid) time given by solutions to the necking zone system (5.17) and (5.19) with $H = 0.01$ for $C = 0.0025$ (black), 0.005, $0.01, 0.02$ (grey). The results corresponding to $C = 0.005$ are indistinguishable from the $C = 0.0025$ results as the pinch-off time predictions converge as $C \to 0$. The red dashed line shows the linear prediction for volume-limited breakdown of quasi-static solutions (5.40).

can conclude that the observed linear scaling is valid in the relevant parameter space for capillary flows. Later, we will show that the scaling is consistent with the widely accepted expression for Taylor bubble length derived by Cubaud *et al.* (2005) from experimentally observed relations, under the assumption that the Taylor bubble takes an approximately cylindrical shape.

5.3 Quasi-static theory for small capillary numbers

As discussed previously, figure 5.4 demonstrates that the flux of solutions is initially extremely small, and becomes significant only as the solution approaches pinch-off. This trend in the flux suggests that the evolution is quasi-static. Thus, as in section 3.2.1, we propose an asymptotic structure comprising two asymptotic decks: a quasi-static deck controlled by surface tension, and an inner deck localised at the front of the necking zone $z_N(t)$. The height of the fluid film in the necking zone is much greater than the constant film thickness defined by the Taylor bubble region ($h \gg B$), such that the height at the front position of the outer deck vanishes in comparison to the interior thickness of the outer region, and forms an apparent contact line. Hence, we impose the boundary conditions

$$h(0,t) = H, \qquad h(z_N,t) = 0, \tag{5.22}$$

on the quasi-static (outer) region, similarly to as in the two-dimensional case (3.28) and (3.29). The governing equation (5.17) is determined by the expression for the flux

$$q = \frac{1}{C}F(h)\kappa_z, \tag{5.23}$$

which becomes zero under a quasi-static assumption so that $\kappa_z = 0$ and curvature is instantaneously uniform in space

$$\kappa = \frac{h_{zz}(1-h) + 1 + h_z^2}{(1-h)(1+h_z^2)^{3/2}} \equiv K(t). \tag{5.24}$$

Hence, the quasi-static assumption in the axisymmetric geometry results in a more complex expression for constant curvature than is required to describe quasi-static solutions in the necking zone of a planar geometry (3.30). In particular, the planar analogue of the constant curvature expression (5.24) results in parabolic solutions, whereas the quasi-static states in an axisymmetric geometry are inherently more complex due to additional azimuthal curvature contributions, as well as the retention of nonlinear curvature terms.

The volume must equal Qt in accordance with the specified dimensionless input flux $q(0,t) = Q$. In contrast to the planar geometry, for which the volume was

specified by an area integral, the volume constraint in an axisymmetric geometry is specified by a volume of revolution

$$\frac{1}{2}\int_0^{z_N(t)} 1-(1-h)^2\,\mathrm{d}z = V(t) = Qt. \tag{5.25}$$

For simplicity, we will specialise here to $H \ll 1$, corresponding to the limit where the nozzle closely spans the width of the channel, as we did in section 3.2.2; some discussion of the effect of finite H is given in section 5.7. Under this assumption, the boundary conditions for the quasi-static system to leading order are

$$h(0,t) = 0, \qquad h(z_N,t) = 0. \tag{5.26}$$

The equations (5.24)–(5.26) form a sub-system for a quasi-static shape for a given volume $V(t)$ and contact line position $z_N(t)$. The axisymmetric Young-Laplace equation (5.24) describes the static shape of a surface of revolution. The contact line evolution $z_N(t)$ is derived from the matching condition

$$h_z^3 = -3C\dot{z}_N \log(\dot{z}_N z_N^3/B^3) \qquad (z = z_N(t)), \tag{5.27}$$

representing the Cox-Voinov law (Cox, 1986; Voinov, 1976) derived for the planar system as (3.33), recast in the non-dimensionalisation associated with our present analysis. Note that (5.27) is derived under a lubrication approximation and therefore requires small interfacial gradients at the apparent contact line $h_z(z_N,t) \ll 1$ to strictly apply; this criterion will be examined in section 5.9. We seek an explicit evolution equation for the contact-line position $z_N(t)$, and isolate the rate of change $\dot{z}_N(t)$ in (5.27) by writing that equation in the equivalent form

$$\dot{z}_N = \frac{B^3}{z_N^3}\exp\left(W\left(-\frac{1}{3CB^3}z_N^3h_z^3\right)\right) \qquad (z = z_N(t)), \tag{5.28}$$

where W is the non-negative branch of the Lambert function. The evolution equation (5.28) has an implicit dependence on the gradient of the interface at the contact line $h_z(z_N)$. In contrast to the planar problem, the frontal slope is not known analytically in terms of V and z_N at all times, as was given by (3.37). Hence, the quasi-static solution states given by solving (5.24) subject to (5.25) and (5.26), along with the evolution equation forms a coupled system. Solutions

to the coupled system provide trajectories in time through the parameter space defined by the two inputs z_N and V; these trajectories will be explored in section 5.4.

5.3.1 Static interfacial solutions

Before we consider the system of static shapes coupled to the moving boundary condition, we begin by analysing the shapes of the static solutions defined by the subsystem (5.24)–(5.26). At an instantaneous point in time, the volume and contact line position can be thought of as given parameters. By parametrising the static shapes by a characteristic length scale z_N and volume V for a specified point in time, we are able to analyse the stability of the static shapes, revealing stability branches in the solutions and criteria on the existence of quasi-static solutions.

In order to avoid singular slopes associated with vertical gradients in the Cartesian coordinate system, we transform the system into arc-length coordinates $\psi(s)$, where the independent variable is the arclength of the interface s pointing towards the peak of the necking disturbance and ψ is the angle between the interface and the horizontal (see appendix 5A). Transformation of the system (5.24)–(5.26) results in the coupled system of ordinary differential equations:

$$h_s = \sin\psi, \tag{5.29}$$

$$\psi_s = \frac{K((1-h)(1+\tan^2\psi)^{3/2}) - (1+\tan^2\psi)}{\sec^3\psi(1-h)}. \tag{5.30}$$

Solutions are found using a shooting method, implementing Newton Raphson to iteratively refine the initial guess until convergence to a solution that satisfies the front condition in (5.22), and the volume constraint (5.25). The iterated parameters are the constant value of curvature K, and the initial angle between the horizontal and the solution, ψ_0.

The parameter space of quasi-static (QS) solution shapes is defined by the two input parameters: the front position of the expanding necking region z_N, and the volume of the fluid film in the necking region V. Figure 5.7 shows some example solutions for a fixed value of z_N, chosen as $z_N = 2$, and a range of specified input volumes. A progression of solutions with increasing volume is shown in panels

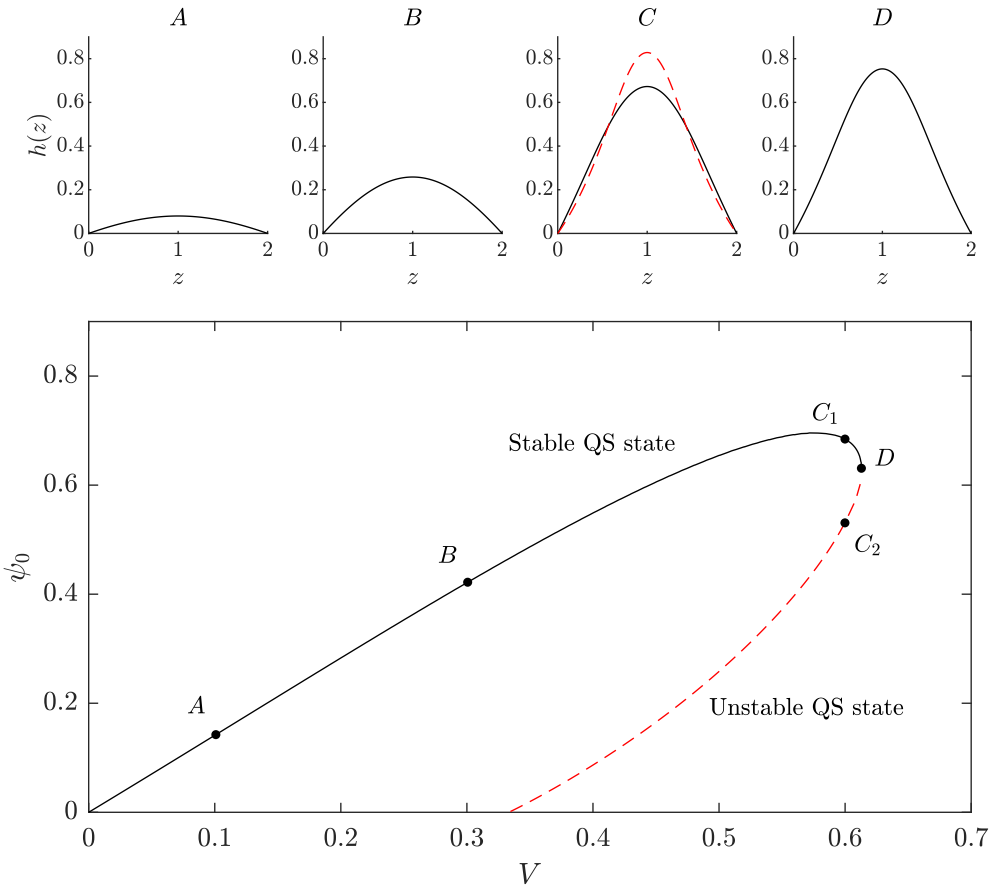

Figure 5.7: Bifurcation diagram showing the relationship between the interfacial angle at the inlet, ψ_0, and the enclosed interfacial volume of the film for fixed contact-line position $z_N = 2$, as predicted by the quasi-static system (5.24)–(5.26). The figure shows the existence of both a stable branch (black, solid) and an unstable branch (red, dashed). The top four panels A–D show the interface shape for a selection of volumes $V \approx 0.1, 0.3, 0.6, 0.613$. For case C, there are two quasi-static states, representing the stable (black, solid) and unstable (red, dashed) solutions. Case D represents the maximum V possible for a quasi-static solution to exist for this value of $z_N = 2$. Only the stable branch is relevant to the dynamic quasi-static theory.

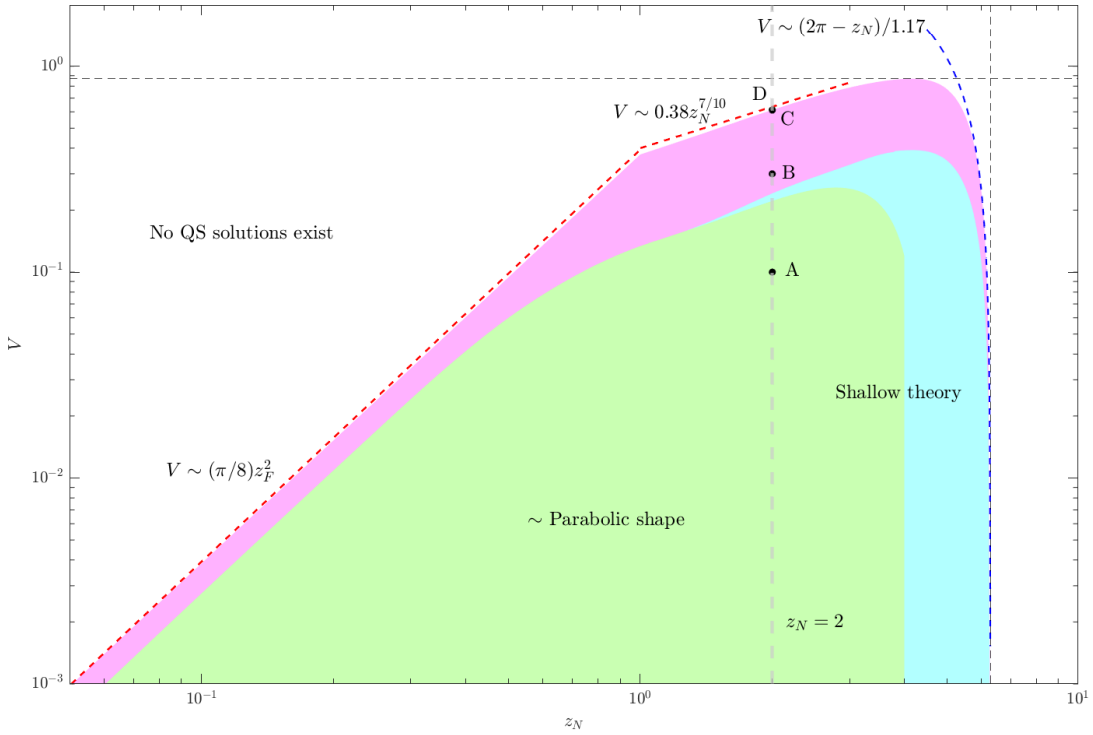

Figure 5.8: Regime diagram categorising the quasi-static solution shapes of the necking zone, as represented by the sub-system (5.24)–(5.26). Shaded regions represent the area of the parameter space for which a quasi-static solution exists, with the vertical grey dashed line corresponding the cross-section of the parameter space at $z_N = 2$ presented in figure 5.7. The region in which the solution is in the shallow wave regime (5.36) is shaded in blue, and the green shading represents the parabolic sub-regime that sits inside the blue region, represented by parabolic solutions (5.39). White space represents the region in which no quasi-static state exists. The red dashed line for $z_N \lesssim 0.9$ corresponds to static solutions with $\psi_0 = \pi/2$; it shows that if $z_N \gtrapprox 0.9$, a solution with $\psi_0 = \pi/2$ cannot exist. This is illustrated in figure 5.7 as, for $z_N = 2$, the max possible ψ_0 is around 0.7. The boundary at the right hand side of the magenta region can be well represented by the analytical expression (5.61), represented by a blue dashed line.

A to D, corresponding to solutions along a stable branch. For smaller volumes, the solutions A and B appear parabolic. As volume increases, the shape of the solution becomes taller and the solutions appear more sinusoidal. There is a critical bifurcation point at D, beyond which a solution with larger volume can no longer exist for the specified z_N. This breakdown of quasi-static solutions was not observed in the planar geometry, whereby the necking disturbance could be described by a quasi-static parabolic solution up until the point of pinch-off. There is another solution shape that can emerge from a second branch, as represented by the dashed red line in the ψ_0–V parameter space. An example is overlayed in panel C showing the two possible solution shapes. This branching behaviour was observed by Lv & Hardt (2021) in their analysis of liquid annulus stability in a capillary tube. By specifying a fixed contact angle and particular volume of the ring, both a steep surface profile and a more shallow surface profile were observed as solutions to the axisymmetric Young-Laplace equations. Lv & Hardt (2021) perform a stability analysis to confirm that the flatter solution shape has a lower interfacial energy and is therefore the only stable configuration. The stable solution branch is represented as a solid line in figure 5.7, whilst the unstable solutions are represented by red dashed lines.

To visualise the critical breakdown of quasi-static solutions in a general context (with the only fixed parameter being $H = 0$), we have shown the region for which a solution to the quasi-static system exists by coloured regions in figure 5.8. The white region represents the space in which quasi-static solutions cannot exist, determined by numerically solving the quasi-static system (5.24)–(5.26) for $z_N \in [0.05, 2\pi]$. The analysis shown by figure 5.7 acts as a cross-section of the regime diagram, corresponding to $z_N = 2$ which is represented by a grey, dashed vertical line. Specifically, the bifurcation point at $V = 0.613$ representing the breakdown of quasi-static solutions corresponds to the top boundary of the magenta region in figure 5.8 at $z_N = 2$. The diagram is plotted in log-log space and we notice that, for values of z_N up to approximately 0.9, the existence of solutions is bounded by a limiting $V \sim z_N^2$ condition. Increasing z_N beyond this value, the critical boundary of the solution space undergoes a change in gradient, reaching a maximum volume $V_m \approx 0.8672$. We note that this critical volume is close to the value 0.871 predicted by Everett & Haynes (1972), when rescaled

according to our scaled volume flux. If the volume of the liquid in the capillary tube was less than this critical value, Everett & Haynes (1972) determined that the liquid will form non-occluding annular humps (unduloids) rather than an occluding liquid plug. For yet larger z_N, there is a steep reduction in the critical volume at which we lose quasi-static solutions. Further, there are no solutions for $z_N > 2\pi$. In contrast to the planar geometry, the loss of quasi-static solutions in an axisymmetric geometry highlights a significant difference to the two-dimensional geometry for which the necking disturbance could be approximated by a quasi-static parabolic solution up until the point of pinch-off. This fundamental difference in solution behaviour signals that a substantially different approach is required for the analysis of quasi-static solutions in an axisymmetric geometry.

The shallow limit

When volume is small, the static solutions have a flatter shape as evidenced in panels A and B of figure 5.7. Hence, for small input volumes V, we can assume that the film surrounding the bubble is thin, $h \ll 1$, and that the rate of change of film thickness is small, $h_z \ll 1$. In this situation, (5.24) becomes

$$\kappa = h_{zz} + h \equiv K_1(t), \tag{5.31}$$

forming a linear ordinary differential equation with general solution

$$h = K_1(t) + A(t)\cos z + D(t)\sin z. \tag{5.32}$$

The bifurcation structure of static solutions to the linearised Young-Laplace equation has been considered by Jensen (1997) in their study of lobe stability in curved cylindrical tubes. Since $h \ll 1$, we can assume the volume constraint (5.25) reduces to leading order

$$\int_0^{z_N} h \, \mathrm{d}z = Qt. \tag{5.33}$$

The prefactors in the general solution (5.32) are found by applying the boundary conditions (5.22) and the volume constraint (5.33):

$$h = A\left(-(1-\cos z) + \frac{\sin z}{\sin z_N}(1-\cos z_N)\right) + H\left(1 - \frac{\sin z}{\sin z_N}\right), \tag{5.34}$$

where

$$A(t) = \frac{Qt \sin z_N + H[(1 - \cos z_N) - z_N \sin z_N]}{2(1 - \cos z_N) - z_N \sin z_N}. \tag{5.35}$$

For the case $H = 0$, the solution reduces as

$$h = \frac{Qt(\sin z - \sin z_N + \sin(z_N - z))}{2(1 - \cos z_N) - z_N \sin z_N}, \tag{5.36}$$

taking a simpler form whereby the film thickness is now proportional to the volume Qt directly and therefore has an essentially self-similar shape. The derivative of (5.36) with respect to z is

$$h_z = \frac{Qt(\cos z - \cos(z - z_N))}{2(1 - \cos z_N) - z_N \sin z_N}, \tag{5.37}$$

specifying a front gradient $h_z(z_N)$ that depends only on z_N and becomes zero at $z_N = 2\pi$. The slope expression in the shallow limit (5.37) is a standard result obtained by linearising the Young-Laplace equation about the base of a cylinder to obtain (5.31) (e.g. Bostwick & Steen, 2015; Cooray *et al.*, 2016; Finn, 1986; Tomotika, 1935). Since the gradient at the front of the necking zone cannot be positive, solutions cannot exist with $z_N > 2\pi$, as was observed in figure 5.8. This restriction stems from the Rayleigh-Plateau instability which states that a gaseous column will break up if its length (i.e. the length of the necking region, z_N) is greater than its circumference. Hence, pinch-off will always occur before the length of the necking region can exceed 2π.

We can compare the analytical solution of the shallow model (5.36) to the static shape predictions of the full curvature quasi-static sol system (5.24)–(5.26). Explicitly, we can use the L_2 norm

$$L_2 = \frac{1}{z_N} \int_0^{z_N} \frac{(y - y_0)^2}{\bar{y}^2} \, \mathrm{d}z, \qquad \text{with} \qquad \bar{y} = \frac{1}{z_N} \int_0^{z_N} y \, \mathrm{d}z, \tag{5.38}$$

to compare the full solution y_0 to the shallow model solution y at a specified z_N and V. We can define a subregime on the parameter space of quasi-static solutions as the region in which $L_2 < 0.01$; this region is shaded in blue on the regime diagram shown in figure 5.8. We notice that the blue region overlaps with most of the space in which quasi-static solutions exist (magenta), suggesting that the shallow limit solution is a good approximation of the quasi-static model across most of the parameter space. In particular, the shallow limit model becomes inaccurate at larger volumes, as is expected.

Parabolic solutions

Under the assumption $z_N \ll 1$, the analytical solution (5.36) reduces to a parabolic solution

$$h(z,t) = \frac{6Qt}{z_N^3} z(z_N - z). \tag{5.39}$$

The parabolic solution (5.39) recovers the two-dimensional quasi-static solutions (3.30) derived in section 3.2.1 for the case $H = 0$.

Again, we can use the L_2 norm defined in (5.38), with y now representing the parabolic analytical solution (5.39), to measure the difference in the parabolic and full curvature solutions. This region is shaded in green on figure 5.8, and is a subregime of the shallow theory model. The parabolic solutions differ from the shallow theory solutions as z_N becomes large and approaches 2π, becoming more sinusoidal.

5.3.2 Quasi-static evolutions

Now that we have analysed the shapes of the quasi-static solutions for specified values of z_N and V, we shall move to exploration of the system formed by coupling the quasi-static solutions to the moving contact line. Explicitly, we specify the input parameters z_N and V at an initial time and solve for the interfacial shapes as in section 5.3.1. The gradient of the solution at the contact line z_N is then substituted into the evolution equation for the front (5.28), resulting in an ordinary differential equation (ODE) for the contact line position. This process is repeated at each time step, resulting in a trajectory for the front position of the necking zone $z_N(t)$. Our numerical implementation involved generating a database of the interfacial gradient $h_z(z_N, t) = f(z_N, V)$ at the front of the necking zone for a given z_N and V over the parameter space of valid quasi-static solutions. Hence, to calculate the trajectory, the particular z_N and V value is specified at each time step and the closest corresponding entry for the front gradient is found from the database and used in the evolution equation for the moving contact line.

Example trajectories for $C = 0.01$ are overlaid onto the (z_N, V) space for quasi-static solutions (figure 5.9) as dashed lines for a range of flux ratios from $Q = 10^{-7}$ to $Q = 0.1$. The trajectories are attractors and so do not depend on the

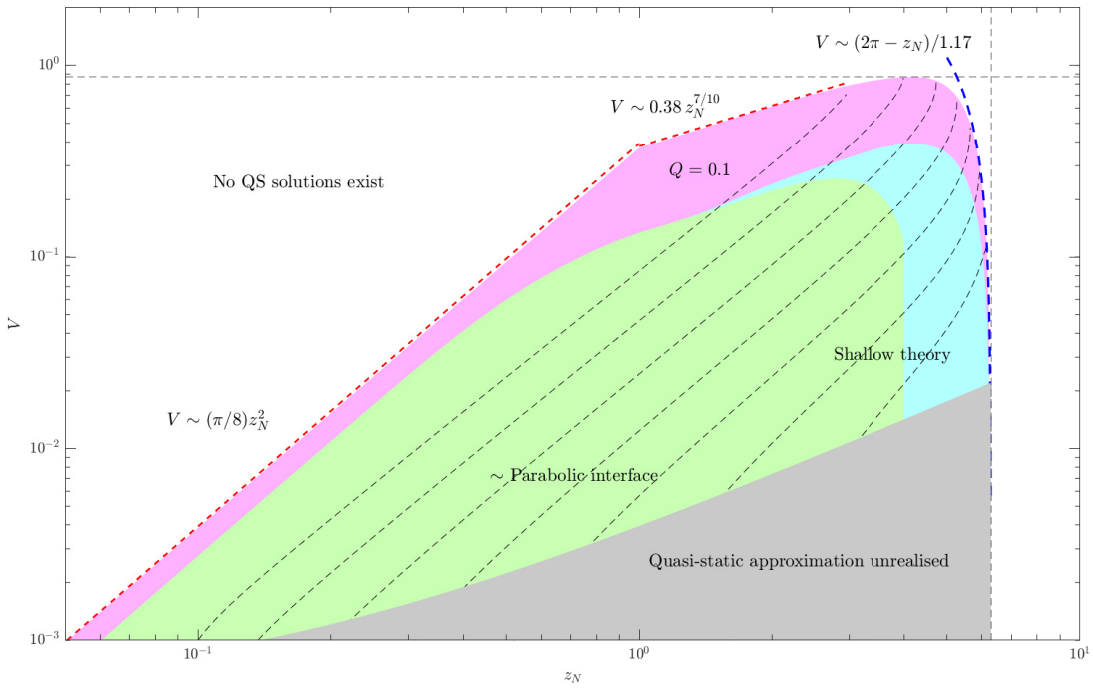

Figure 5.9: Regime diagram for the axisymmetric static shapes, with the trajectories for the coupled system with $C = 0.01$ and $Q = 0.1$ to 10^{-7} overlayed as black, dashed lines. The trajectories terminate at the boundary of the coloured region, which represents the loss of quasi-static solutions. In the grey region, the quasi-static approximation remains unrealised (for this particular capillary number) as the length-scale separation underlying its asymptotic structure has not been established.

initial conditions of the system. The trajectories terminate when they reach the critical boundary of the region in (z_N, V) space where the quasi-static solutions cease existing, represented by the whitespace in figure 5.8; the critical time at which the quasi-static solution no longer exists is defined as t_c.

The maximum volume and front position that can be attained by the quasi-static solutions with $H = 0$ are $V_m \approx 0.8672$ and $z_N = 2\pi$. These limits are represented as horizontal and vertical dashed lines respectively in figure 5.9. As the front position grows towards 2π, the trajectories for small Q bend upwards before termination, representing a saturation in the length of the necking zone z_N. Since volume is proportional to time as $V = Qt$ for constant input flux, the termination of trajectories due to the volume constraint $V = V_m$ gives a corresponding time condition on the termination of quasi-static solutions

$$t_c = \frac{0.8672}{Q}. \tag{5.40}$$

However, in some cases the constant value $V_m = 0.8672$ does not characterise the terminating volume precisely. For example, the trajectory corresponding to an input flux ratio $Q = 0.1$ reaches the volume-constrained limit (top boundary) of the quasi-static solution domain at a volume slightly less than V_m, specifically the terminating volume for $Q = 0.1$ is $V = 0.783$. Additionally, the trajectory shown in figure 5.9 with $Q = 10^{-7}$ terminates due to a length constraint as z_N approaches the limiting value 2π. To improve the scaling for volume-limited breakdown of solutions and to develop a theory for the length-restricted breakdown of quasi-static solutions, we require a better mathematical understanding of the trajectories.

We note significant differences in our findings so far compared to the two-dimensional geometry. In the planar geometry, the solution could be approximated by a parabolic quasi-static shape until the point of pinch-off, and asymptotic predictions for the pinch-off time could be directly calculated from the analytical parabolic solutions. In contrast, static solutions in the axisymmetric geometry do not always conform to a parabolic solution, and the region of the parameter space over which quasi-static solutions exist is limited. Hence, the behaviour of solutions outside of the parabolic regime must be analysed in order to obtain predictions for pinch-off time. Additionally, we find that the quasi-static

states are not able to describe the evolution of the interface up until the point of pinch-off $h_m(t_*) = 1$. However, we hypothesise that the breakdown of quasi-static solutions might be equivalent to the pinch-off time. This speculation is motivated by the form of (5.40), which suggests an inverse linear relationship between the dimensionless pinch-off time and the flux ratio, corresponding to a linear dependence of t_c on q_c when redimensionalised according to the scalings defined in (5.16). The same scaling has been observed experimentally (e.g. Cubaud *et al.*, 2005; Garstecki *et al.*, 2006; Xiong *et al.*, 2007). The hypothesis that $t_* = t_c$ will be revisited in section 5.6, after we have analysed the asymptotic behaviour of the quasi-static solution evolutions.

5.4 Asymptotics of the quasi-static trajectories

In order to understand the forward trajectories and conditions for which the breakdown of solutions can be attributed to a volume-limited constraint rather than a length-limited constraint, we need to understand the asymptotics of the trajectories of quasi-static solutions. The regime diagrams shown in figure 5.8 and 5.9 partition the coloured region over which quasi-static solutions exist into shallow theory (blue) and parabolic (green) sub-regimes. In the parabolic regime, trajectories follow the path predicted by the parabolic solution (5.39) coupled with the evolution equation (5.28) up until the point of pinch-off (e.g. $Q = 0.1$ in figure 5.9). As Q decreases, we notice that the trajectories curve up before reaching the boundary for the existence of quasi-static solutions. Trajectories that follow this characteristic path are said to be in the length-saturation regime (shown most clearly for $Q = 10^{-4}$ and $Q = 10^{-5}$ in figure 5.9).

5.4.1 Trajectories in the parabolic regime

To begin the analysis of the trajectories, we can utilise the analytical solutions of the parabolic solution (5.39), which have an explicit prediction for the gradient at the contact line

$$h_z(z_N) = -\frac{6Qt}{z_N^2}. \tag{5.41}$$

The parabolic gradient (5.41) is the same as was derived in the quasi-static analysis for the planar geometry (3.37), under the assumption $H = 0$. Interestingly, the trajectories are therefore initially the same in the axisymmetric case as they were in the planar configurations. Hence, we can proceed in the same way as in section 3.2.2 to derive a leading order expression for the front position of the necking zone z_N. First, we substitute the gradient (5.41) into the z_N evolution equation (5.28) as

$$\dot{z}_N = B^3 z_N^{-3} \exp\left(W\left(72C^{-1}B^{-3}z_N^{-3}(Qt)^3\right)\right). \tag{5.42}$$

To analyse (5.42), we note that there are two intrinsic scalings: the first is from the prefactor to the exponential function, and the second is from the argument of the W-function

$$z_N^4 \sim B^3 t, \qquad \text{and} \qquad z_N \sim \frac{Qt}{BC^{1/3}}. \tag{5.43}$$

Combining these scales, we can define the rescaled variables

$$t = \left(\frac{B^7C^{4/3}}{Q^4}\right)^{1/3}\tau, \qquad z_N = \left(\frac{B^4C^{1/3}}{Q}\right)^{1/3}\xi_N \equiv Z\,\xi_N, \tag{5.44}$$

such that the evolution equation (5.42) becomes

$$\xi_N^3\frac{\mathrm{d}\xi_N}{\mathrm{d}\tau} = \exp\left(W\left(\frac{72\tau^3}{\xi_N^3}\right)\right). \tag{5.45}$$

Note that in (5.44) we have defined a dimensionless parameter Z, which will be used later in the analysis of the length-saturation regime.

Using the large-argument asymptote $W \sim \log(z) - \log(\log(z))$ as $z \to \infty$, (5.45) reduces to an ordinary differential equation

$$\dot{\xi}_N \sim \frac{72\tau^3}{\xi_N^6\log(72\tau^3/\xi_N^3)}, \tag{5.46}$$

that is equivalent to (3.40) in the planar geometry. The notation differs between (3.40) and (5.46) due to the different non-dimensionalisations defined for each of the two geometries. As in section 3.2.2, we seek a leading-order asymptotic solution to (5.45), using the large-argument asymptote $W \sim \log(z) - \log(\log(z))$ as $z \to \infty$.

Following the same steps, we determine that the front of the necking zone evolves as

$$\xi_N = \left(\frac{98\tau^4}{\log\tau}\right)^{1/7} \qquad (\tau \gg 1), \tag{5.47}$$

and the analytical prediction for the leading-order position of the front of the pinch-off disturbance within the necking zone (5.47) is the same in these scaled variables as was derived as (3.45) in section 3.2.2.

Recall from section 3.2.1 that, in the planar geometry, the quasi-static solutions existed up until the pinch-off time t_*, and hence the time restriction was $1 \ll t \leq t_*$ in the dimensionless coordinates defined in section 3.1.3. The lower bound was specified by the requirement on length-scale separation associated with the defining asymptotic structure of solutions. In terms of the scaled coordinate system studied here, the criterion for quasi-static scale separation becomes

$$\frac{1}{(\dot{\xi}_N)^{1/3}} \ll \xi_N, \tag{5.48}$$

and the condition must hold in order to ensure that the inner deck is much smaller than the scaling of the outer deck. In particular, as $\xi_N(t)$ grows, the condition (5.48) will become ever more strongly satisfied with time ($\tau \gg 1$). Hence, the necessary boundary layer structure does not exist at early times, and the theory is only consistent at times large enough for attraction to a quasi-static state to have been established. We recast the time scale on which the quasi-static regime emerges $\tau \sim 1$ in the new non-dimensional time coordinate t associated with the axisymmetric geometry, to give a time scale t_Q on which attraction to the quasi-static solution is complete

$$t = B^{7/3}C^{4/9}Q^{-4/3} \equiv t_Q. \tag{5.49}$$

Quasi-static solutions in an axisymmetric configuration are therefore restricted by the criterion

$$t_Q \ll t \leq t_c, \tag{5.50}$$

where the upper bound is defined by the critical time t_c at which a quasi-static solution ceases to exist. The condition (5.50) then represents the region of the parameter space over which the assumption of a quasi-static regime is consistent.

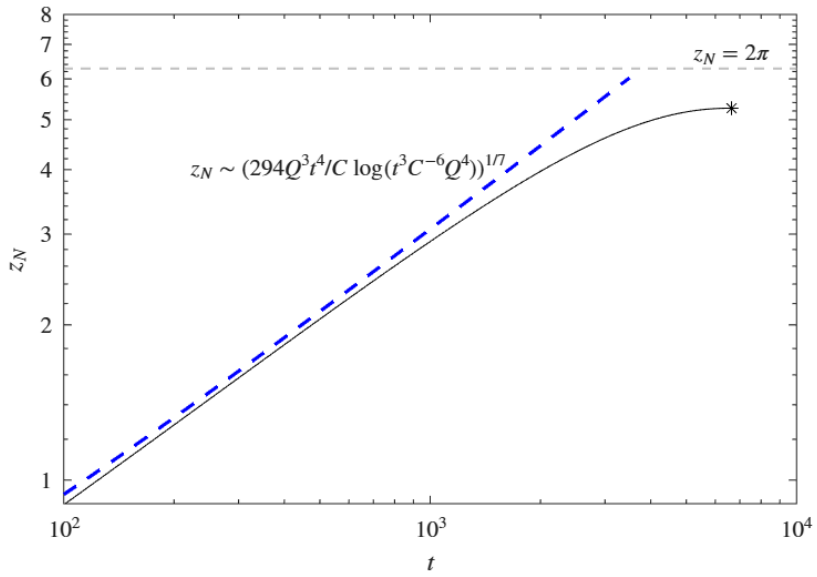

Figure 5.10: A plot of the z_N evolution according to the system of quasi-static interfacial shapes (5.24)–(5.26) coupled to the evolution equation (5.28) with $Q = 10^{-4}$ and $C = 0.01$. The trajectory initially follows the asymptotic prediction (5.47), before deviating as t increases further. Specifically, the z_N evolution slows down as the front position approaches 2π.

In order to determine the region over which this assumption is valid, we must determine t_c.

Figure 5.10 shows the prediction of the $z_N(t)$ evolution given by numerical solutions to the quasi-static coupled system with $C = 0.01$, $Q = 10^{-4}$. The late time asymptotic solution (5.47) is recast into the original dimensionless variables using the scaling (5.43), and overlaid as a blue dashed line showing excellent agreement with the coupled quasi-static system (5.24)–(5.26) along with the evolution equation (5.28) for $z_N \lessapprox 2$. As z_N increases further, the trajectory departs from the parabolic sub-regime and therefore deviates from the late-time asymptotic prediction specified by (5.47). Figure 5.10 shows a plateau in the evolution of $z_N(t)$ corresponding to a saturation in the front position z_N as it increases towards its maximum value of 2π; the behaviour of trajectories in this regime will be the focus of the following subsection (section 5.4.2).

The trajectories demonstrate that quasi-static states evolve towards a point

at which a quasi-static solution ceases to exist. We hypothesise that the loss of a quasi-static solution corresponds closely with the time at which pinch-off occurs (i.e. $t_c = t_*$). This hypothesis will be examined later in section 5.6. For now, we focus on the behaviour of the quasi-static solutions as they approach the boundary of existence, with the aim of obtaining an expression for the time to breakdown of quasi-static solutions t_c that will ultimately give a condition from (5.50), defining the region of the parameter space over which quasi-static solutions breakdown before a quasi-static state can be attained.

5.4.2 Trajectories in the length-saturation regime

Figure 5.9 shows that, at larger Q, the trajectories continue along the path determined by the parabolic solution $z_N \sim t^{4/7}$ (equivalently, $V \sim z_N^{7/4}$) until their termination. However, at smaller flux ratios $Q = 10^{-4}$ and 10^{-5}, the trajectories deviate from the $t^{4/7}$ scaling associated with the parabolic regime and exhibit a bend upwards on the regime diagram as the front position z_N approaches 2π. The deviation from the parabolic regime is highlighted by the trajectory shown in figure 5.10. Specifically, the trajectory initially follows the late-time asymptotic solution predicted by the parabolic regime (5.47). At later times, the $z_N(t)$ evolution predicted by the coupled system slows down in comparison with the solution of the parabolic regime.

In order to obtain a reduced description of such trajectories that exhibit the characteristic associated with the length-saturation regime, we can utilise the large-argument approximation of the W function $W(z) \sim \log(z/\log z)$ to reduce the evolution equation (5.28) as follows

$$\dot{z}_N = \frac{-\frac{1}{3}C^{-1}h_z^3}{\log(-\frac{1}{3}C^{-1}B^{-3}z_N^3h_z^3)}. \tag{5.51}$$

In the asymptotic analysis presented thus-far in section 5.4.1, we have been considering the parabolic regime which is a subset of the shallow limit quasi-static solutions. Now, since z_N is becoming $O(1)$, the trajectories depart from the parabolic regime and we use the full analytical front gradient in the shallow limit (5.37) as

$$h_z = -Qtf(z_N), \qquad \text{where} \qquad f(z_N) = \frac{1-\cos z_N}{2(1-\cos z_N) - z_N \sin z_N}, \tag{5.52}$$

which, in contrast to the parabolic expression (5.39), allows for $z_N = O(1)$. Introducing a stretched time $t = C^{1/4}Q^{-3/4}s$, we can substitute (5.52) into the reduced evolution equation (5.51) to obtain

$$\frac{\mathrm{d}z_N}{\mathrm{d}s} = \frac{\frac{1}{3}s^3 f(z_N)^3}{\log\left(\frac{1}{3}Z^{-9/4}z_N^3 s^3 f(z_N)^3\right)}, \tag{5.53}$$

where Z is as defined in (5.44). The argument of the logarithm must be must sufficiently large

$$\frac{1}{3}Z^{-9/4}z_F^3 s^3 f(z_F)^3 \gg 1, \tag{5.54}$$

and so, since all other factors on the left hand side of (5.54) are $O(1)$, we require Z to be small for quasi-static theory to be realised before the breakdown of quasi-static solutions can occur. Hence, $Z^{9/4} = \varepsilon$ is a small parameter in the problem. The solution to the ordinary differential equation in (5.53) describes trajectories that begin in the parabolic regime but deviate from the $t^{4/7}$ scaling before termination, and shows that trajectories are equivalent subject to a temporal scaling. This is evident as a shift in parallel trajectories shown in the regime diagram (figure 5.8).

The late-time prediction of the parabolic regime will become the early-time behaviour of the solution in the length-saturation regime. Hence, we can recast (5.47) into the scaled time variable to obtain the early-time regime

$$z_N = \left(\frac{98s^4}{\log\left(\frac{s}{\varepsilon^{7/9}}\right)}\right)^{1/7}. \tag{5.55}$$

The trajectory begins to deviate from the prediction of the parabolic regime (5.55) when $f(z_N)$ can no longer be approximated by the small z_N approximation that defines the parabolic regime (5.41), which corresponds to the condition $z_N = O(1)$. Hence (5.55) gives a time scale on which the trajectory transitions from the parabolic regime to the length-saturation regime as

$$s \sim \log\left(1/\varepsilon^{7/9}\right)^{1/4}, \tag{5.56}$$

such that (5.55) is consistent when the condition (5.56) is satisfied. At this time scale, the ordinary differential equation (5.53) reduces as

$$\frac{\mathrm{d}z_N}{\mathrm{d}s} = \frac{s^3 f(z_N)^3}{3\log\left(\varepsilon^{-1}\right)}, \tag{5.57}$$

since, by definition of the length-saturation regime, (5.56) holds and $z_N = O(1)$ so that we can neglect the higher-order terms of size $\log(\log(f(z_N))) \ll \log(z_N)$. Upon the definition of a further stretched time coordinate $s = (\log(1/\varepsilon^{7/9}))^{1/4}\sigma$, the ordinary differential equation (5.57) further reduces as

$$\frac{\mathrm{d}z_N}{\mathrm{d}\sigma} = \frac{1}{3}\sigma^3 f(z_N)^3, \tag{5.58}$$

giving a parameterless expression for the evolution of the front position through the parabolic and length-saturation regimes.

Hence, we have obtained a reduced description of the z_N evolution as it deviates from the parabolic regime and approaches length saturation. The solution can be obtained as a numerically represented function $z_N(\sigma)$ which should better approximate the $z_N \to 2\pi$ plateau observed in figure 5.10. Early-time and late-time regimes of (5.58) come from using the small and large z_N leading order representations of $f(z_N)$ respectively. Using the leading-order small z_N representation $f \sim 6z_N^{-2}$, the ordinary differential equation (5.58) becomes separable with analytical solution

$$z_N = (126\sigma^4)^{1/7}. \tag{5.59}$$

Similarly, $f \sim -(z_N - 2\pi)/4\pi$ in the limit $z_N \to 2\pi$, and the resulting ordinary differential equation has solution

$$z_N = 2\pi - \sqrt{\frac{384\pi^3}{\sigma^4}}, \tag{5.60}$$

forming a late-time regime of (5.58) that characterises the behaviour of trajectories in the length-saturation regime as they approach termination. Figure 5.11 shows excellent agreement between the numerical solution to the system of quasi-static interfacial shapes (5.24)–(5.26) coupled to the evolution equation (5.28) and the early-time asymptotic prediction of the universal solution (5.59), overlaid as a red dashed line. In the late time limit, the evolution of the necking front in the coupled system slows down until termination when quasi-staticness is lost. The asymptotic result (5.60) (blue, dashed) captures the deviation from the parabolic regime, particularly for smaller flux ratios Q where the length saturation z_N persists over a longer time.

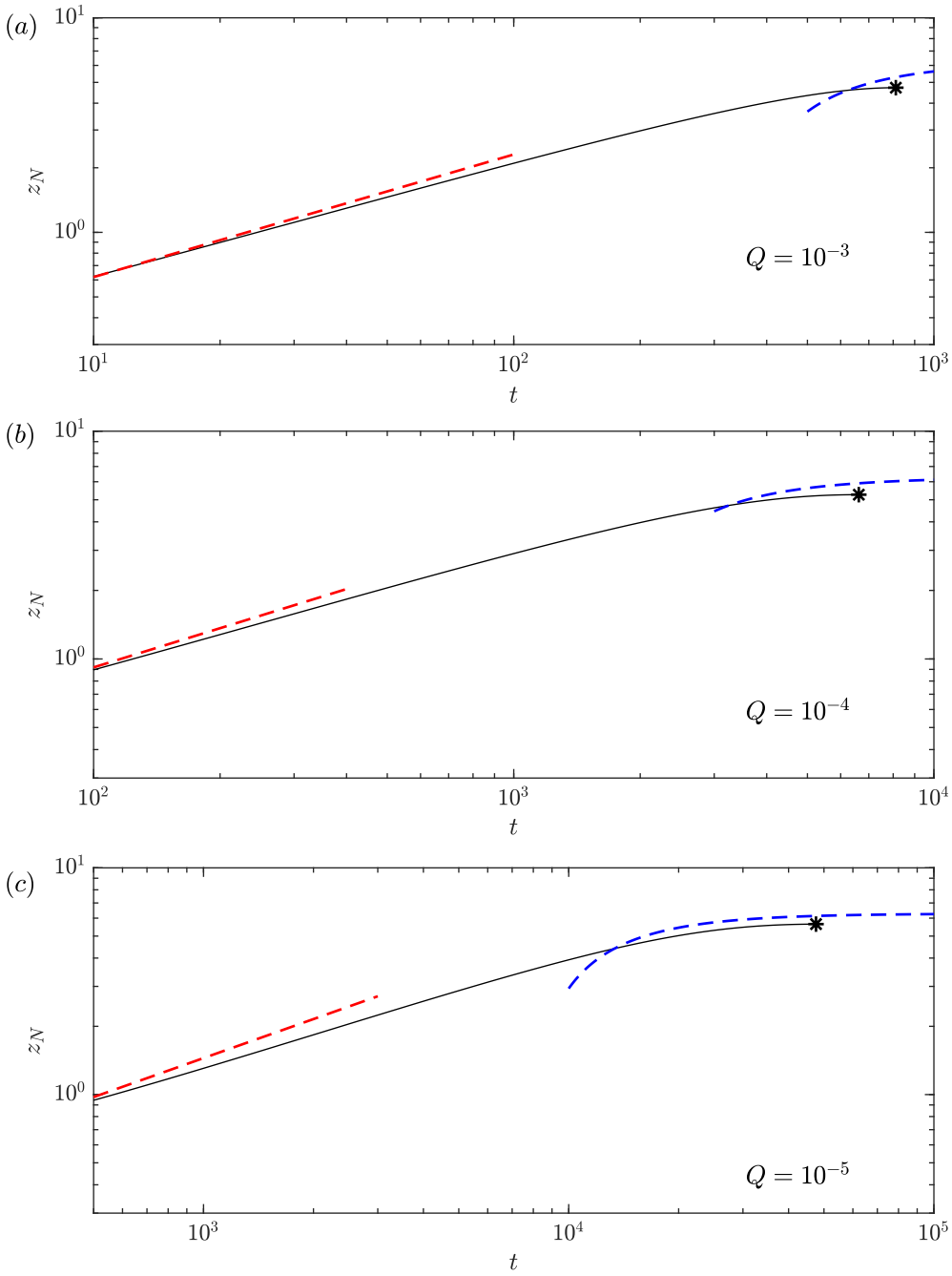

Figure 5.11: Example trajectories with $C = 0.01$ given by the coupled system (black) in the length-saturation regime with (a) $Q = 10^{-3}$ (b) $Q = 10^{-4}$ and (c) $Q = 10^{-5}$. The trajectory terminates when a quasi-static solution ceases to exist (represented by an asterisk). The early-time (5.59) (red) and late-time (5.60) (blue) asymptotic predictions of the length-saturation regime are transformed into t and overlaid as dashed lines, showing improved predictions over the parabolic regime as $z_N \to 2\pi$. The agreement improves with smaller Q.

Now that we have obtained an understanding of the trajectory behaviour in the length-saturation regime, we can characterise the breakdown of quasi-static solutions as they approach length restriction $\max(z_N) = 2\pi$. We can see from the regime diagram of quasi-static solutions (figure 5.8) that the trajectories terminate when they reach the white-space representing the region in which no quasi-static solutions exist. The trajectories are either volume-limited or length-limited, depending on whether they reach the top edge or the right edge of the solution domain respectively. If a trajectory terminates as it reach the top edge, defined as $V = V_m \approx 0.8672$, it is volume-limited and the critical time for loss of a quasi-static solution is defined as in (5.40).

A trajectory may also terminate as it approaches the length restriction $z_N = 2\pi$. We obtain an expression for the right hand edge of the solution domain as

$$z_N = 2\pi - 1.17\,Qt, \tag{5.61}$$

by trialling power laws and fitting numerical prefactors until the expression above was found to provide an excellent approximation of the numerical boundary (overlaid as a blue dashed curve in figure 5.8). To find the time at which the trajectories intersect with this critical boundary, the late-time solution to the length-saturation regime (5.60) can be recast into the original time variable t as

$$z_N = 2\pi - \sqrt{\frac{384\pi^3 \log(1/\varepsilon)}{Q^3 C^{-1} t^4}}. \tag{5.62}$$

Equating the expression (5.62) to the numerically obtained critical boundary for the existence of quasi-static solutions (5.61), we obtain an expression for the length-limited breakdown of quasi-static solutions in the length-saturation regime as

$$t_c = 4.535\,Q^{-5/6}\left(C\log(1/\varepsilon)\right)^{1/6}. \tag{5.63}$$

We now have two predictions for t_c corresponding to the two modes of quasi-static solution breakdown: volume-limited, and length-limited. By comparing the two expressions, we can determine by which mode the solution will be terminated. This is the focus of the next section (section 5.4.3).

However, before we progress onto analysing the mode of breakup, we return to validating the asymptotic consistency of the assumption outlined in (5.50) as

$$t_Q \ll t_c. \tag{5.64}$$

Comparing t_Q, as defined in (5.49), to both the volume-limited and length-limited expressions for t_c gives two parametric conditions under which the assumption is consistent; both are captured in the scaling $Z \ll 1$. The condition is represented by the grey region on the parameter space shown in figure 5.12, which corresponds to the region of the parameter space over which $Z \gg 0.1$.

Now that we have determined the time scale on which a quasi-static state is reached and subsequently terminates, we can continue to analyse the mode of quasi-static breakup.

5.4.3 Volume-limited and length-limited breakdown of quasi-static solutions

In order to determine whether the breakdown of the quasi-static solution is due to the length-limited or volume-limited breakdown of solutions, we need to determine whether the trajectory is constrained by (5.63), or the constraint $V = V_m$ which results in (5.40). This is equivalent to considering an idealised trajectory that terminates at both the maximum volume and neck position z_N possible for a quasi-static solution state, i.e. termination occurs at $(z_N, V) = (2\pi, V_m)$. This trajectory represents the separation between quasi-static solutions terminated by a length-limited constraint and those terminated due to a volume limitation.

To numerically determine this partition, we can equate the two expressions for time to breakdown, (5.40) and (5.63), resulting in a condition for the breakdown of solutions as

$$Q = \frac{\phi}{CW(\phi B^{-4} C^{-4/3})} \tag{5.65}$$

where $\phi \approx 8.383 \times 10^{-5}$. The expression above specifies the boundary between the mode by which breakdown of quasi-static solutions occurs, and is used to partition the C–Q parameter space in figure 5.12 into regimes characterised by volume-limited (green) and length-limited (blue) breakdown. When the flux ratio Q is small, corresponding to a larger input flux of bubble compared with

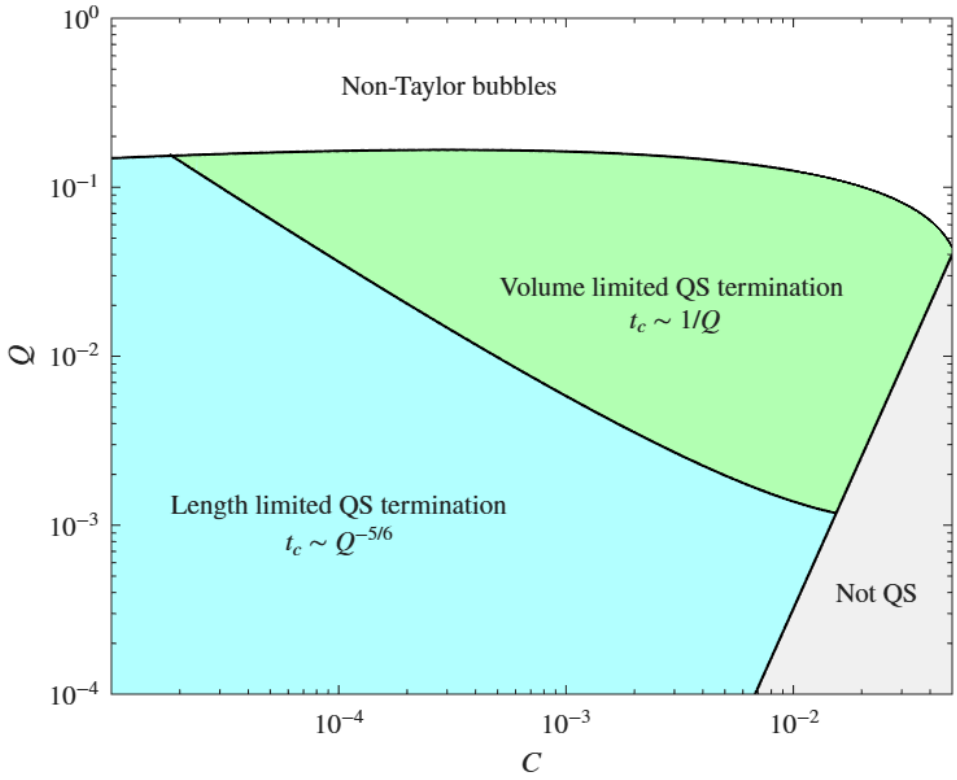

Figure 5.12: Regime diagram for the mode of breakdown of quasi-static solutions at time t_c. The grey region (partitioned by $Z = 0.1$) divides the parameter space; to the right of the line, trajectories break down before they are able to establish a quasi-static shape. To the left, the breakdown of quasi-static solutions is dependent on the position in the C-Q parameter space relative to the boundary (5.65). Solutions that are characterised by a breakdown in the length-limit $z_N \to 2\pi$ are coloured blue, while volume-limited regimes are coloured green.

liquid, the breakdown of quasi-static solutions favours the length-limited regime. Interestingly, when capillary number is small, we can apply the large-argument simplification of the Lambert-W function in (5.65) and determine that the key control parameter determining the mode of quasi-static solution breakdown is defined by the product CQ, equivalent to the capillary number of the continuous phase. This is evident in the regime diagram (figure 5.12) since the dividing line is approximately linear with gradient -1 for small C.

5.5 Conditions for asymptotic self-consistency of the Taylor bubble assumption

We examine the consistency of the Taylor-bubble regime, which again is defined by the property (cf. (3.54) for the planar geometry)

$$z_N(t_*) \ll z_F(t_*), \tag{5.66}$$

where z_N describes the characteristic length of the necking disturbance and z_F is the position of the Taylor bubble cap. In the axisymmetric configuration considered here, the length of the necking zone is always limited by 2π. The prediction for the front of the expanding necking zone $z_N(t)$ and the nose of the Taylor bubble $z_F(t)$ depends on whether the breakdown of quasi-static solutions is volume-limited or length-limited. In the length-limited regime, the scalings are defined as

$$z_N \sim 2\pi, \qquad z_F \sim 4.1\, Q^{-5/6} \left(C \log(C^{-3}Q)\right)^{1/6}, \tag{5.67}$$

where $z_F \sim t_c$ since $U \sim 1$ to leading order, and the time to pinch off is given by (5.63). Hence, (5.66) gives

$$12.1\, Q^5 \ll C\log(C^{-3}Q), \tag{5.68}$$

using the Bretherton relationship $B \sim C^{2/3}$ for small capillary numbers. Similarly, for the volume-limited regime, the scalings are defined as

$$z_N \sim \frac{16.0}{(QC)^{1/7} \log(Q^{11}C^{-18}V_m)}, \qquad z_F \sim \frac{V_m}{Q}, \tag{5.69}$$

using (5.47) and $V_m = 0.8672$ as specified in (5.40) respectively. Hence, (5.66) gives

$$18.4\, (Q^6 C^{-1})^{1/7} \ll \log(Q^{11}C^{-18}V_m). \tag{5.70}$$

Since the formation of non-Taylor bubbles primarily occurs due to the volume-limited breakdown of quasi-static solutions associated with larger flux ratio Q, we can define the regime for Taylor bubble formation according to (5.70). The restriction $z_N/z_F \ll 0.1$ corresponds to an almost horizontal line at $Q \approx 0.1$, recovering the same form of restriction on Taylor bubble formation as was derived in section 3.2.3 and section 4.3.2; namely Q must be small.

The requirement for Taylor bubble formation in a planar geometry was dependent on Q only, forming a horizontal boundary across the parameter space. For the axisymmetric case presented here, the boundary follows a similar shape and demonstrates only a weak dependence on the capillary number C.

5.6 The link between loss of a quasi-static solution and pinch-off

Our quasi-static analysis has demonstrated the conditions for the breakdown of quasi-static solutions, but does not directly predict the pinch-off time. We hypothesised in section 5.3.2 that the loss of quasi-static solutions may correlate with the time to pinch-off. As was discussed in section 5.2, solutions to the full time-dependent model (5.17) along with boundary conditions (5.19) exhibit a rapid acceleration in the maximum film thickness immediately before pinch-off occurs, corresponding to an increase in flux and hence suggesting a deviation from the quasi-static regime. If the time over which this deviation occurs is sufficiently small, we expect there to be good agreement between the necking zone prediction of t_*, and the breakdown of quasi-static solutions t_c. Here, we now examine the relationship between t_c and t_* over the parameter space.

We compare the predictions of the full time-dependent model (5.17) along with boundary conditions (5.19) against the predictions of the quasi-static system. Figure 5.13 shows the maximum film thickness $h_m(t)$ predicted by each model for $C = 0.002$ with three different flux ratios (a) $Q = 10^{-1}$, (b) 10^{-3} and (c) $Q = 10^{-5}$. The blue dashed line represents the maximum value of the static solution (5.24)–(5.26) representing the film thickness at each time step, with the position of the front $z_N(t)$ calculated by evolution equation (5.28). We notice that the point at which quasi-static solutions cease to exist (illustrated by the termination of the blue dashed curve) roughly coincides with the pinch-off of the necking zone solution (termination of the solid black line), particularly for $Q = 0.1$ and 0.0001. This idea was first observed in figure 5.4 where it was noted that the rapid increase in $h_m(t)$ just before the point of pinch-off coincided with a growth in fluid flux, equivalent to the breakdown in the quasi-static assumption.

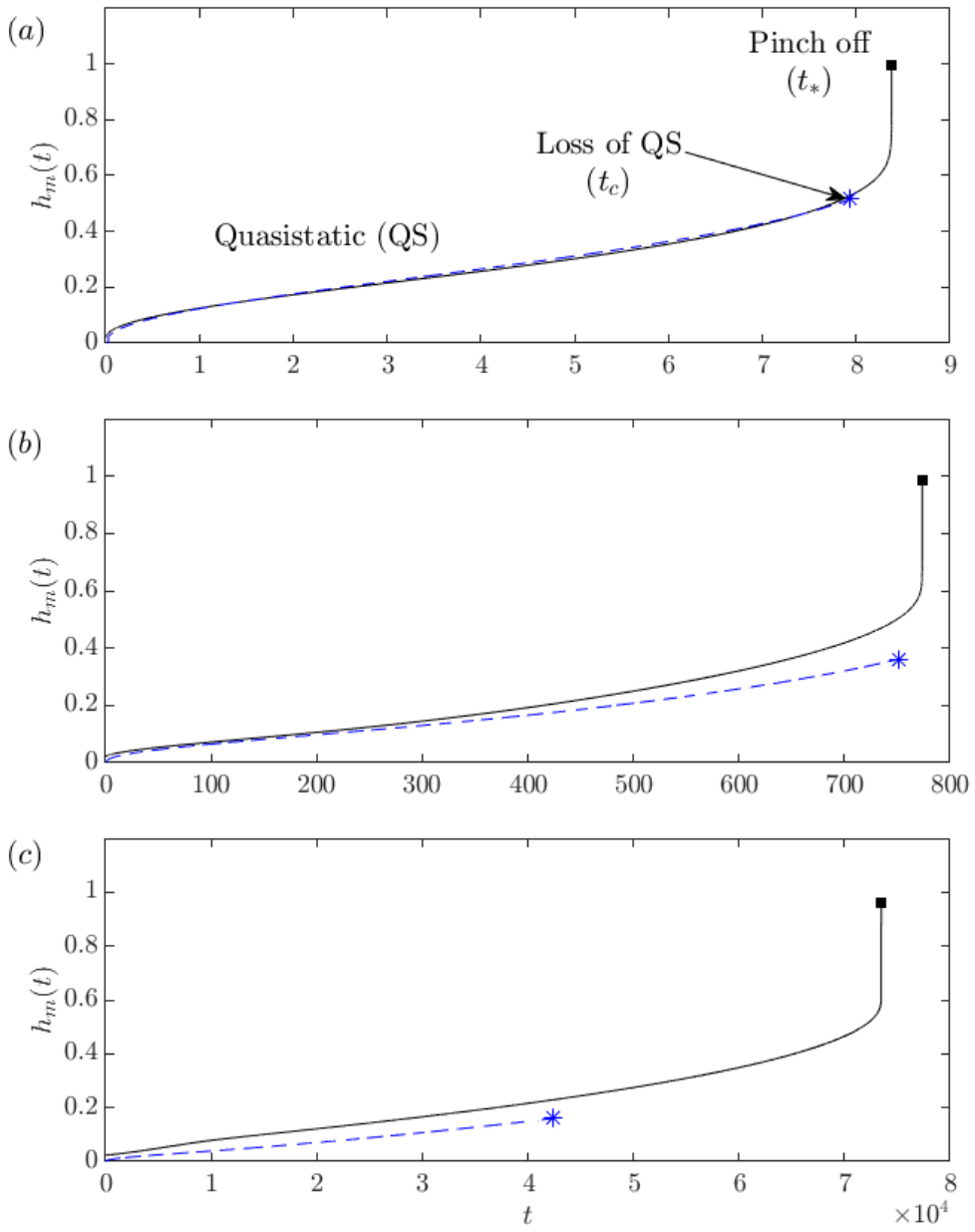

Figure 5.13: An example of the maximum film thickness $h_m(t)$ evolution with $C = 0.002$ and (a) $Q = 0.1$, (b) $Q = 10^{-3}$, (c) $Q = 10^{-5}$. The solution to the full time-dependent system defined by (5.17) subject to boundary conditions (5.19) with $H = 0.01$ up until pinch-off time t_* is compared to the solution to the quasi-static system defined by (5.24)–(5.26) coupled with the evolution equation (5.28) up until its breakdown at t_c. For larger flux ratios, the trajectories are more strongly quasi-static.

To determine a numerical measure of the relation between time to pinch-off and loss of a quasi-static solution, one can calculate the ratio t_*/t_c. In order to gain a full understanding of the relationship between t_c and t_*, one could repeat the analysis shown in figure 5.13 to obtain predictions for both pinch-off time and the quasi-static breakdown time across the whole parameter space. For example, one could highlight the parameter values for which $0.9 \leq t_*/t_c \leq 1.1$ to emphasise the region of the parameter space over which the breakdown of quasi-static solutions is essentially equivalent to the occurrence of pinch-off.

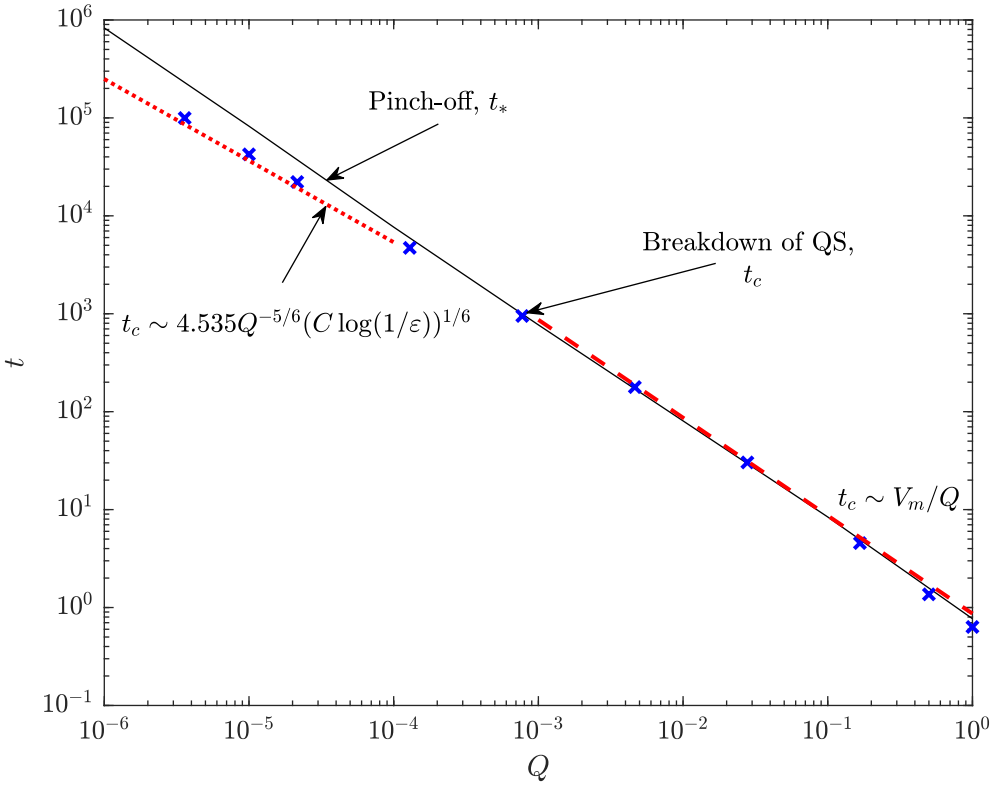

Figure 5.14: The time for bubble pinch-off t_* predicted by the full time-dependent model ((5.17) and the boundary conditions (5.19)) with $H = 0.1$ compared with the time of breakdown of quasi-static solutions t_c predicted by the coupled system (5.24)–(5.26) along with the evolution equation (5.28) for a range of flux ratios Q and fixed capillary number $C = 0.002$. The quasi-static asymptotes (5.40) and (5.63) are overlaid at large Q and small Q respectively.

Taking the time at which quasi-static solutions are lost t_c as equivalent to

the bubble pinch-off time t_*, the prediction for the volume-limited breakdown of quasi-static solutions (5.40) is sufficient to give a theoretical prediction for pinch-off time as $t_* \sim 1/Q$. The prediction for pinch-off time is overlaid as a red dashed line in figure 5.6, showing good agreement with the time-dependent solutions to the necking zone model at large Q. The time-dependent model predictions show better agreement with the asymptote derived from quasi-static solutions in the small C limit where the precursor film layer is smaller and is therefore a better approximation of the vanishing film thickness at the contact line. However, these solutions of the necking zone model become harder to resolve for very small capillary number as it becomes necessary to resolve the moving contact line singularity, and so we are restricted by how small we can make the capillary number in numerical solutions to the time-dependent necking model. Figure 5.14 compares the time for bubble pinch-off predicted by the full necking zone system (black, solid line) to the time taken to breakdown of quasi-static solutions (blue crosses) for a range of input flux ratios Q and fixed capillary number $C = 0.002$. We notice that the times are equivalent for larger Q, as was predicted by figure 5.13, but the discrepancy grows as Q decreases. As suggested previously, we can attribute this discrepancy to the inconsistent boundary conditions at the nozzle, which will be explored in more detail in section 5.7. The pinch-off time predicted by the breakdown of quasi-static solutions shows excellent agreement with the asymptotic predictions (5.63) and (5.40), overlaid as red dashed lines, in the small and large Q limits respectively.

5.7 Impact of nozzle width

In section 5.6, we noticed a discrepancy in the predictions of pinch-off time given by the time-dependent necking zone model (5.17) and(5.19) and the coupled quasi-static system (5.24)–(5.26) along with the evolution equation (5.28) for small Q. We attributed the discrepancy in pinch-off time predictions of the two models to the difference in boundary condition at $z = 0$, since the coupled quasi-static system satisfies $h(0, t) = 0$ whereas the necking zone theory fulfils a non-zero film thickness at the input boundary $h(0, t) = H$. The size of the input nozzle relative to the capillary pipe is represented by the parameter $H \in (0, 1)$,

with a larger value of H represents a larger film thickness surrounding the nozzle and hence a relatively smaller input nozzle. Here, we give a some insight into the effect of this inconsistency, leaving an in-depth exploration as future work.

It is reasonable to suggest that the parameter H plays a role in pinch-off since the loss of a quasi-static solution can happen when the thickness of the film is still quite small, when pinch-off occurs due to an almost instantaneous spike in film thickness h. This is intuitive in the parabolic case because the film thickens slowly and the solution remains quasi-static all the way to $h = 1$. In the non-parabolic case, this is more counter-intuitive as pinch-off in this case is no longer controlled by a gradual thickening to $h = 1$, but rather a gradual transition to non-quasi-static which can happen when the film thickness is still small.

We can generalise the quasi-static theory (5.24)–(5.26) to keep the boundary condition $h(0, t) = H$ as a replacement to (5.26a), allowing for non-zero film thickness at the input nozzle. Altering the boundary condition changes the shape of the quasi-static solutions, and hence each value of H must have its own corresponding database describing the quasi-static solution shapes for the parameter pairs (V, z_N). A full exploration into the effect of the boundary condition with $H \neq 0$ would therefore be a laborious task and is left as potential future work. Instead, we explore just the trajectories with $H = 0.1$. Figure 5.15 compares the quasi-static breakdown t_c predicted by the coupled system (5.24)–(5.26) with evolution equation (5.28) subject to boundary condition $H = 0$ (blue crosses) and $H = 0.1$ (red crosses) for capillary number $C = 0.002$. The predictions for t_c are compared to the pinch-off times given by solutions to the necking zone system (black line) with boundary condition $H = 0.1$. We notice that, for moderate to large flux ratios, both predictions of the quasi-static system exhibit good agreement with the necking zone theory despite the discrepancy in the boundary conditions for solutions represented by blue crosses and hence substantiates our hypothesis that $t_c \approx t_*$. However, for small flux ratio $Q \lesssim 10^{-4}$, the difference in boundary condition becomes more impactful as the red crosses agree better with the black line than the blue crosses.

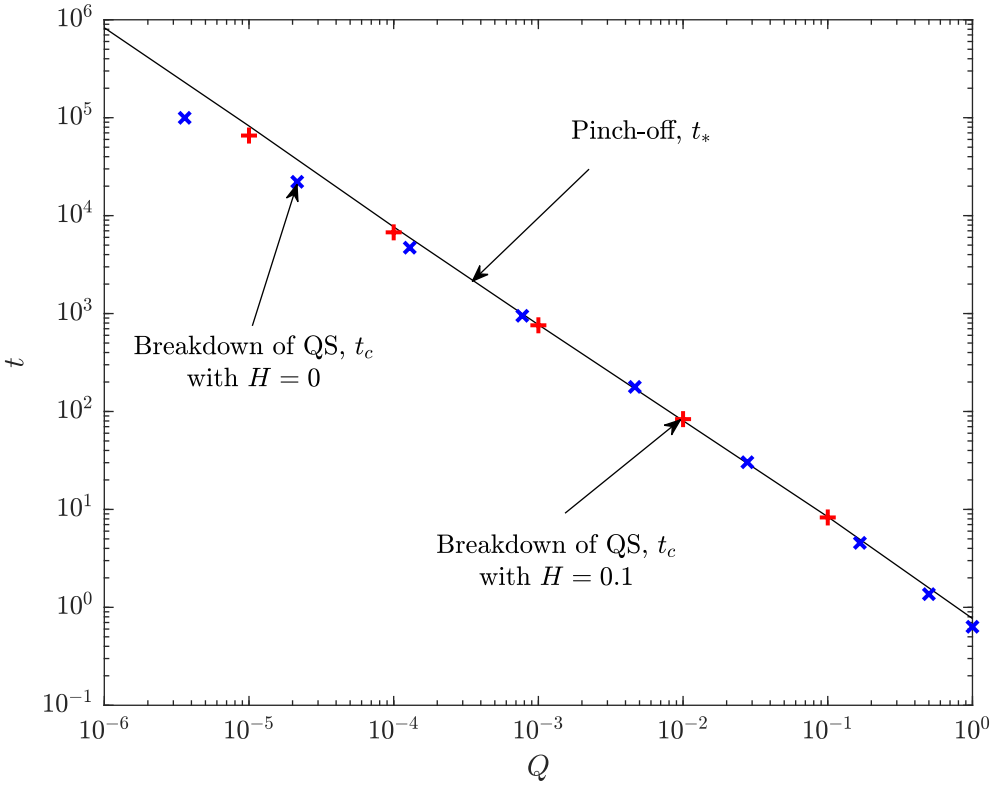

Figure 5.15: The numerical pinch-off times t_* predicted by the full time-dependent system ((5.17) and the boundary conditions (5.19)) with $h(0,t) \equiv H = 0.1$ and $C = 0.002$ are plotted alongside the critical time to breakdown of quasi-static solutions t_c predicted by the coupled system (5.24)–(5.26) along with the evolution equation (5.28). The red crosses represent quasi-static solutions that account for the boundary condition $H = 0.1$, exhibiting better agreement with the time-dependent necking solutions when compared to quasi-static solutions with $H = 0$ (blue crosses).

5.8 Comparison to experimental results

Cubaud *et al.* (2005) conducts an experimental investigation into the formation of Taylor bubbles in a microchannel of square cross-section. Microchannels of square cross-section will approximate flows in axisymmetric cylindrical capillary tubes more closely than two-dimensional planar configurations (its cross-sectional radius will deviate from a circle of equivalent area by a factor of $\sqrt{\pi/4}$). Air is

injected through one microchannel at volumetric flow rate q_d, and water is injected through two equally sized channels, placed perpendicularly at either side of the main channel, at a volumetric flow rate of $q_c/2$ (such that the total volumetric flow rate of the liquid phase is q_c). From the experimental observations, a scaling law for the length of the Taylor bubble was proposed as

$$\frac{L_B}{2R} = \frac{1}{\alpha_L} \equiv \frac{q_c + q_d}{q_c} \tag{5.71}$$

where $2R$ here represents the height of the square channel, and α_L is referred to in Cubaud *et al.* (2005) as the homogeneous liquid fraction. The range of volumetric flow rates considered for each phase are small (0.1 to 11 mm^3/s for q_d, and 0.8 to 4 mm^3/s for q_c) and the scaling law (5.71) is validated against experiments in the range $0.1 < \alpha_L < 1$.

Cubaud *et al.* (2005) recognised that the scaling law (5.71) was limited to the square channel, where the gas bubble is confined as a cylinder (as opposed to slit microchannels formed of two parallel flat plates, creating a rectangular cross-section where the height is much smaller than the width), and the surrounding liquid flows in wedges as opposed to a film coating the interior of a cylindrical capillary. However, experimental investigations into different microfluidic configurations have yielded similar scaling laws. Garstecki *et al.* (2006) considers the formation of Taylor bubbles in the context of a T-junction configuration such that bubble breakup is caused by cross-flow rupturing. A scaling law very similar to (5.71) was deduced from experimental observations as

$$\frac{L_B}{2R} = 1 + a\frac{q_d}{q_c}, \tag{5.72}$$

where a is some constant of order unity, whose exact value is determined by the geometry of the T-junction. In the case $a = 1$, (5.72) reduces to (5.71). Xiong *et al.* (2007) provides an investigation into the formation of Taylor bubbles in a co-flowing slit microchannel configuration. The air and liquid (either water, or an aqueous solution of glycerol) were injected in parallel into a microchannel of cross-sectional area 1.69×0.07 mm^2. A high-speed camera is used to capture the evolution of periodic bubble formation, and the experimental observations are validated against numerical simulations based on the volume of fluid (VOF)

method. The experimental predictions for bubble length show excellent agreement with (5.72) with $a = 1$, Although striking similarities have been found in empirical scaling laws across a wide range of geometries, there is no existing theoretical explanation of the experimentally observed results.

The theoretically derived results presented in this chapter thus far are given in terms of dimensionless numbers. In order to compare our predictions to existing experimental results, we require dimensional predictions for Taylor bubble pinch-off time. As experimental investigations are usually limited to small capillary numbers and a fluid flux ratio in the range $0.01 \lesssim Q \lesssim 10$ (Cubaud *et al.*, 2005; Garstecki *et al.*, 2006; Xiong *et al.*, 2007), it is reasonable that physically-observed are likely to correspond to the volume-limited regime shaded green in figure 5.12. Subject to the scalings presented in (5.16), we can recover a dimensional form of the prediction for the pinch-off time in the volume-limited regime (5.40) as

$$t_* = \frac{0.8672R^3}{q_c}, \tag{5.73}$$

suggesting that the time to bubble pinch-off is affected by both the radius of the capillary tube R, and the volumetric flux of the liquid phase q_c.

The empirical scaling laws reviewed above focus on the length of Taylor bubbles produced. Hence, we convert our prediction for pinch-off time (5.73) into an equivalent expression for bubble length L_B. The volume of the bubble is given by the expression

$$V_b = \bar{q}_d t_* = 2\pi q_d t_*. \tag{5.74}$$

Assuming that the bubble adopts an approximately cylindrical shape, we can obtain an expression for the bubble length as

$$L_B = \frac{2q_d t_*}{R^2}, \tag{5.75}$$

which, subject to our prediction for volume-limited pinch-off (5.73), gives

$$L_B = 0.8672 \left(\frac{2q_d R}{q_c} \right). \tag{5.76}$$

Figure 5.16 shows the experimental results of Cubaud *et al.* (2005) (blue unfilled markers), with the scaling law (5.71) overlayed as a black, solid line. As

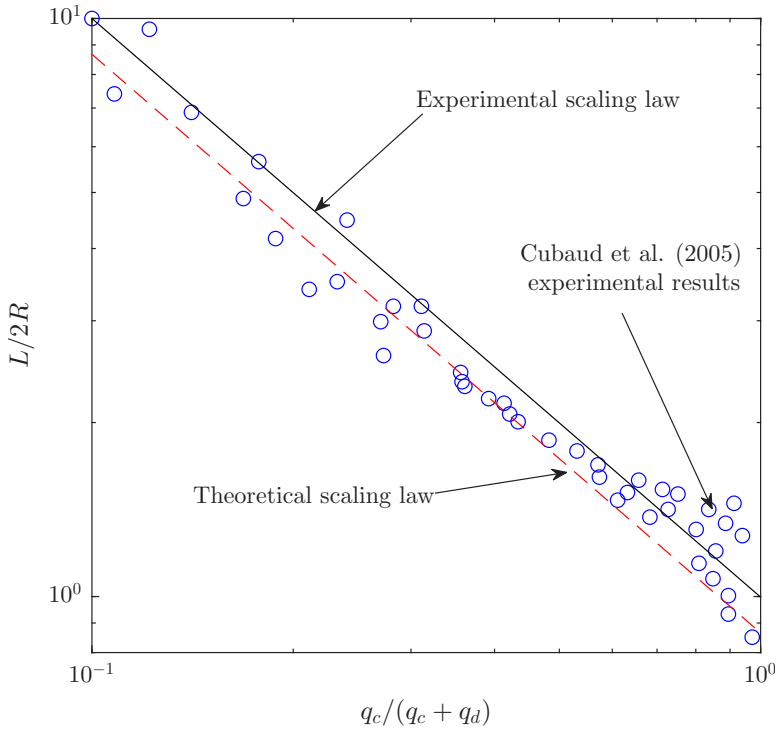

Figure 5.16: Our theoretically derived scaling law for volume-limited bubble pinch-off is compared to the water/air experimental results of Cubaud *et al.* (2005) (cf fig. 2 of Cubaud *et al.* (2005), $C \sim 10^{-2}$), showing excellent agreement.

determined earlier in section 5.5, Taylor bubbles are formed when the flux ratio Q is small (i.e. $q_c \ll q_d$) such that, under this assumption, $\alpha_L \approx q_c/q_d$ in the Taylor bubble regime (corresponding to $\alpha_L \ll 1$). Hence, we have theoretically derived the prediction $t_* \sim 1/q_c$, and have shown that the theoretically derived prefactor for the bubble length L_B has a 13% discrepancy. This agreement between our theoretically derived prediction of bubble pinch-off time (5.76) (red dashed), and the scaling law of Cubaud *et al.* (2005) (5.71) is evident in figure 5.16, highlighting particularly good agreement between experimental results and our prediction (5.76) in the limit $\alpha_L \ll 1$. Thus, we have derived a theoretical explanation of this empirical law that emerges from a volume-limited constraint in the quasi-static theory.

5.9 Discussion

In this chapter, we have provided the first theoretical explanation for the experimentally observed scaling law $t_* \sim 1/q_c$ (Cubaud *et al.*, 2005). Our analysis relies on the coupling of static shapes describing the interface in the necking region, to an evolution equation for the front position of the necking region based on the Cox-Voinov law (5.27). Whilst the static solutions allow for large interfacial gradients throughout the necking region, the Cox-Voinov law is derived from lubrication theory, requiring small interfacial gradients at the apparent contact line (corresponding to the front of the necking zone region, z_N). Hence, there is a contradiction with the allowance of large interfacial gradients by retention of the nonlinear curvature expression (5.9). In order to determine the region of the parameter space over which the model is self-consistent, we examine the situations in which the interfacial gradient at the front of the necking region $h_z(z_N)$ is small.

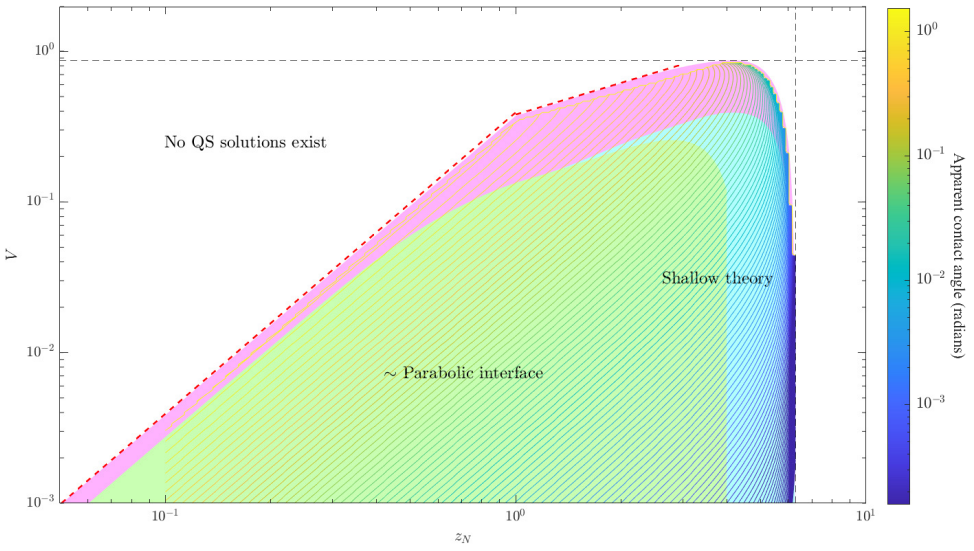

Figure 5.17: Contour plot showing the size of the angle at the apparent contact line z_N as predicted by static solutions of the axisymmetric Young-Laplace equation subject to a volume of revolution constraint, represented by the sub-system (5.24)–(5.26).

Figure 5.17 shows the size of the apparent contact angle ψ, as predicted by

static solutions represented by the sub-system (5.24)–(5.26), evaluated at z_N. Angles evaluated at the boundary of the coloured region correspond to final quasi-static states before the breakdown of quasi-static solutions, and hence correspond to the apparent contact angle at pinch-off. We notice that, for much of the growth of the pinch-off disturbance, the apparent contact angle is small ($\theta_{\text{app}} \lesssim 0.2$), corresponding to a small gradient at the front of the necking disturbance and therefore a consistent lubrication theory across the apparent contact line. The dark blue contours at the right-hand edge of the quasi-static solution space highlight that apparent contact angle is especially small in the case of length-limited breakdown of quasi-static solutions. This is justified as the width of the necking disturbance is limited by its maximal value $\max(z_N) = 2\pi$. Hence, the corresponding maximal aspect ratio in the length-limited regime is $h_z \sim 1/2\pi$ which is relatively small.

In contrast to the planar geometry, where we derived a consistency check on the lubrication approximation over the parameter space in section 3.2.3, we have not derived an exact expression to define the region of consistency from the scalings of the system. We recognise that the model presented is not entirely accurate if the interfacial gradient at z_N is order one. However, the analysis presented above leads us to expect that lubrication theory will apply, despite not being fully justifiable by the scalings of the system as in the planar geometry. We speculate that a more sophisticated representation of the contact line could be adopted to more accurately capture the evolution at large contact angles (Snoeijer, 2006).

5.10 Conclusions

The work presented in this chapter provides two key contributions towards the understanding of Taylor bubble pinch-off in an axisymmetric coflow geometry. Firstly, we developed a quasi-static theory for the evolution of the necking disturbance and analyse the quasi-static states describing the interfacial shape of the surrounding fluid film in the approach to bubble pinch-off. We analysed the region of the parameter space over which quasi-static solutions can exist, demonstrating a significant difference in contrast with the planar geometry. The time to loss of a quasi-static solution was found to be broadly the same as the pinch-off

time defined as the point at which the full time-dependent model predicts that the bubble thins to a zero thickness. Secondly, we compare the theoretical predictions of bubble pinch-off to existing experimentally observed trends and thus our results provide the first theoretical derivation from first principles of the scaling law for injection-driven Taylor bubble pinch-off time $t_* \sim 1/q_c$.

We show that the existence of quasi-static solutions is limited by both a maximal volume restriction and a maximal length condition. The parameters of the system determine whether the loss of a quasi-static solution corresponds to the volume-limited or length-limited mode of break up, and therefore control the behaviour of the necking disturbance in its evolution towards pinch-off. We show that the time between loss of a quasi-static solution and the pinch-off of the bubble is small enough that the two events can be thought of as happening simultaneously.

We hence provide a full regime analysis for the breakdown of quasi-static solutions. By presenting asymptotic simplifications of the necking zone dynamics in the late-time limit, we obtain predictions for bubble pinch-off time. In particular, we show that the volume-limited regime of quasi-static solution breakdown recovers empirical scaling laws for bubble pinch-off (Cubaud *et al.*, 2005; Garstecki *et al.*, 2006; Xiong *et al.*, 2007). Hence, the work presented in this chapter presented the first theoretical explanation of the experimentally derived relationship $t_* \sim 1/q_c$.

Appendix 5A. Arc-length–angle transformation of quasi-static theory

We shall now define the subsystem (5.24)–(5.26) in terms of the arc-length coordinate system, so that we avoid the problem of infinite interfacial gradient associated with nozzle intrusion in the Cartesian coordinate system. Defining the arclength-angle coordinate system (where the independent variable is the arclength of the interface s pointing towards the front of the bubble) as

$$\mathrm{d}z = \cos\psi \, \mathrm{d}s, \tag{5.77a}$$

$$\mathrm{d}h = \sin\psi \, \mathrm{d}s. \tag{5.77b}$$

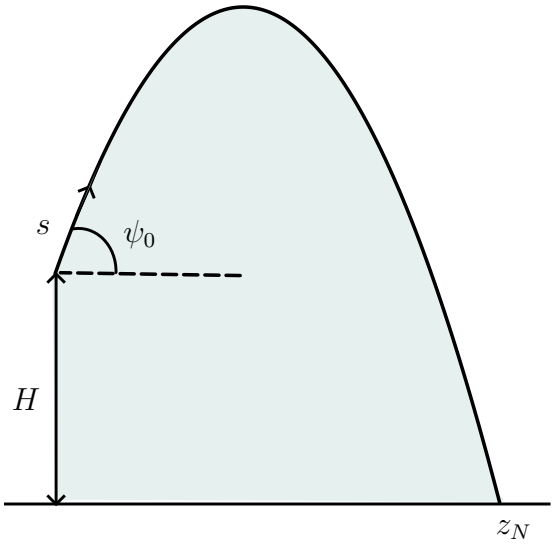

Figure 5.18: A schematic of the static equilibrium shapes to the Young-Laplace equation in an arc-length coordinate system.

where $\psi \in [-\pi, \pi]$. The constant curvature equation (5.24) becomes

$$\frac{\psi_s \sec^3\psi(1-h) + 1 + \tan^2\psi}{(1-h)(1+\tan^2\psi)^{3/2}} = K, \tag{5.78}$$

which, along with the arc length derivative h_s (5.77b), forms a coupled system

$$h_s = \sin\psi, \tag{5.79}$$

$$\psi_s = \frac{K((1-h)(1+\tan^2\psi)^{3/2}) - (1+\tan^2\psi)}{\sec^3\psi(1-h)}. \tag{5.80}$$

We solve the system using a shooting method, implementing Newton Raphson iteration to converge to a solution that satisfies the front condition in (5.22), and the volume constraint (5.25). We shoot forward from an initial condition specifying the height of the fluid film $h_0 = H$, specified by boundary condition (5.26) throughout the chapter, and initial angle above the horizontal ψ_0, and terminate when the height of the thin film reaches zero (giving the front position of the solution z_N). We vary the shooting parameters ψ_0 and K until a solution with the desired volume and front position is reached.

Chapter 6

Conclusions

1 Main findings

This thesis provides the first theoretical derivation of experimentally observed scaling laws for Taylor bubble pinch-off on a capillary scale. To reach this end result, we began with analysis of Taylor bubble pinch-off in a simple planar geometry, and built towards Taylor bubble pinch-off dynamics in an axisymmetric capillary tube by progressing through problems of increasing complexity.

As a first step, we considered Taylor bubble pinch-off in two-dimensional geometry. By considering a lubrication theory for the necking film between the bubble injection nozzle and the film thickness surrounding the developing Taylor bubble, we conducted a numerical and mathematical study of the pinch-off dynamics of two-dimensional Taylor bubbles. The theory yielded a prediction for the dimensionless pinch-off time, $t_* \propto d^{7/3}/q_c^{4/3}$, where q_c is the flux of viscous fluid and d is the half-width of the channel. For small capillary numbers, a quasi-static limiting theory is demonstrated based on coupling an outer near-static regime of the pinching film with an apparent dynamic contact line that matches the necking zone to the film surrounding the Taylor bubble. This asymptotic structure, which becomes more defined in the limit of small capillary number, revealed a fundamental link between capillary pinch-off dynamics and the asymptotic regimes underlying spreading droplets. The study thereby yielded new mathematical understanding of flow regimes that can underlie bubble generation in capillary systems, and acts as a first step to the application of quasi-static analysis to

more complex axisymmetric examples of injection-driven capillary pinch-off. The necking zone theory is asymptotically consistent with a classical lubrication with linearised curvature, and hence a rigorous asymptotic theory of the full-Stokes problem. However, the approach is limited to pinch-off of a single bubble and cannot be applied to oscillatory pinch-off dynamics.

To address the periodic pinch-off of Taylor bubbles, we developed a nonlinear time-dependent lubrication framework that serves as a simplified modelling approach to the full-Stokes equations. Two new themes were investigated with this new model: validation of the pinch-off times predicted by the time-dependent necking zone system against oscillatory pinch-off predictions, and the generation of smaller, non-Taylor bubbles. Although retention of nonlinear curvature terms in combination with a lubrication framework means that the model is somewhat inconsistent, the model is shown to recover the classical matched asymptotic structure of a Taylor bubble, as proposed by Bretherton (1961) in the small capillary number limit, as well as the predictions for bubble thickness presented by Ratulowski & Chang (1989) providing a helpful check on the model in the context of travelling wave states. The model framework can also be motivated by existing literature that has used similarly inconsistent modelling approaches and have validated their findings successfully against numerical or experimental results. In order to fully validate the model outlined in chapter 4, similar comparisons to full-Stokes flow solutions is required.

Having now established a theoretical inroad into the modelling of Taylor bubble pinch-off in a capillary, we progressed to the more complicated axisymmetric geometry that is the typical configuration of experiments. In contrast to the planar geometry, the addition of azimuthal curvature contributions significantly alters the behaviour of solutions as a bubble approaches pinch-off. As in the planar configuration, we presented a mathematical theory based on a separation of the thin-film flow into two asymptotic regions: an outer region, wherein a fast diffusive time-scale maintains the interface close to the shape of a static meniscus; and an inner region localised near a frontal apparent contact-line position, wherein the flow is matched to the precursor film. While the shape of the static meniscus could be approximated as a parabola in the planar configuration,

the solutions of the axisymmetric Young-Laplace equation cannot be entirely described as parabolic and hence a more rigorous investigation into the quasi-static regime of interfacial shapes is required. We showed that pinch-off is controlled by a critical condition at which quasi-static solutions spontaneously cease to exist; the loss of such solutions results in a rapid acceleration in the rate of necking, with pinch off occurring almost immediately thereafter. Under this hypothesis, the quasi-static theory reveals two pinch off regimes: one based on a limit to the volume of the quasi-static film; the other on the length between the input and the contact line. We find that the volume-limited criteria, typical of the flow parameters associated with microfluidics, yields a theoretical law for pinch-off time $t_* \propto 1/q_c$, hence providing the first mathematical derivation of an empirical law proposed previously on the basis of experimental observations.

2 Suggestions for future work

The framework presented in this thesis serves as a simplified modelling approach to study the pinch-off of Taylor bubbles. We acknowledge that the modelling approach is limited to a lubrication framework and does not take into account full-Stokes effects. In particular, numerical simulations of the full-Stokes problem would serve as useful validation for the nonlinear curvature lubrication theory presented in chapter 4, but is beyond the scope of the present study.

We acknowledge that using a Cox-Voinov law to specify the evolution of the dynamic contact line is a limitation of the work presented in this thesis. By including nonlinear curvature terms in the mathematical model of axisymmetric pinch off presented in chapter 5, we recognise that the model is not technically a valid lubrication theory at large apparent contact angles, in contrast to the linearised lubrication framework considered for the planar geometry. Whilst solutions to the axisymmetric Young-Laplace problem allow for large interfacial gradients in the outer region, the validity of the quasi-static analysis requires the gradient of the static meniscus to be small at the apparent contact line. We presented a contour plot of the apparent contact angle over the space of quasi-static solutions and showed that the contact angle remains reasonably small ($\theta_{\text{app}} \lesssim 0.2$) for much of the evolution of the necking disturbance. We suggest that the model accuracy

could be improved by instead implementing models of larger contact angles, such as the model proposed by Snoeijer (2006). However, this modification would have no effect on the region of the parameter space over which quasi-static solutions exist (since this is determined exclusively by the Young-Laplace equations). We believe the trajectories would be only slightly altered, and that the modification would be unlikely to alter the predictions of the time to pinch off.

Finally, validation of the hypothesis made in chapter 5, that pinch-off coincides with the loss of a quasi-static solution, would be a beneficial accompaniment to the work presented in this thesis. The assumption appears logical due to the rapid acceleration in necking that is experimentally observed as a bubble thins in its approach to pinch-off. As a first step in determining the parameter space over which $t_c \approx t_*$, we present some example results in figure 5.13 supporting the assumption for larger flux ratios. However, an in-depth mathematical analysis to compare the two times over the entire parameter space would be beneficial.

Despite the approximations of the model, we are able to recover experimentally observed scaling laws with remarkable accuracy, highlighting the benefits of the approach as a simplified but accurate compromise to full-Stokes flow. We believe that the analysis presented herein can contribute to a more detailed understanding of Taylor bubble pinch-off in a small channel or capillary, and can perhaps be applied to geometries more complex than the coflow configuration considered here (such as flow-focusing).

References

Abramowitz, M. & Stegun, I.A. (1965). *Handbook of mathematical functions: with formulas, graphs, and mathematical tables*, vol. 55. Courier Corporation. 55, 58

Ambravaneswaran, B., Wilkes, E.D. & Basaran, O.A. (2002). Drop formation from a capillary tube: Comparison of one-dimensional and two-dimensional analyses and occurrence of satellite drops. *Physics of Fluids*, **14**, 2606–2621. 18, 71

Anna, S.L. (2016). Droplets and bubbles in microfluidic devices. *Annual Review of Fluid Mechanics*, **48**, 285–309. 1, 47, 77

Aradian, A., Raphael, E. & De Gennes, P.G. (2001). "Marginal pinching" in soap films. *Europhysics Letters*, **55**, 834. 85

Arias, S. & Montlaur, A. (2020). Numerical and experimental study of the squeezing-to-dripping transition in a T-junction. *Microgravity Science and Technology*, **32**, 687–697. 22

Asadolahi, A.N., Gupta, R., Leung, S.S., Fletcher, D.F. & Haynes, B.S. (2012). Validation of a CFD model of Taylor flow hydrodynamics and heat transfer. *Chemical Engineering Science*, **69**, 541–552. 10, 108

Aussillous, P. & Quéré, D. (2000). Quick deposition of a fluid on the wall of a tube. *Physics of fluids*, **12**, 2367–2371. 15, 16, 24

Batchelor, G.K. (2000). *An introduction to fluid dynamics*. Cambridge university press. 28

Bechtel, S., Cao, J. & Forest, M. (1992). Practical application of a higher order perturbation theory for slender viscoelastic jets and fibers. *Journal of non-newtonian fluid mechanics*, **41**, 201–273. 18

Bercic, G. & Pintar, A. (1997). The role of gas bubbles and liquid slug lengths on mass transport in the Taylor flow through capillaries. *Chemical Engineering Science*, **52**, 3709–3719. 108

Bonn, D., Eggers, J., Indekeu, J., Meunier, J. & Rolley, E. (2009). Wetting and spreading. *Reviews of modern physics*, **81**, 739. 28, 32, 67, 111

Bostwick, J. & Steen, P. (2015). Stability of constrained capillary surfaces. *Annual Review of Fluid Mechanics*, **47**, 539–568. 132

Brenner, M.P., Eggers, J., Joseph, K., Nagel, S.R. & Shi, X. (1997). Breakdown of scaling in droplet fission at high reynolds number. *Physics of Fluids*, **9**, 1573–1590. 18, 70, 71

Bretherton, F.P. (1961). The motion of long bubbles in tubes. *Journal of Fluid Mechanics*, **10**, 166–188. 3, 4, 5, 10, 11, 12, 13, 15, 30, 42, 43, 44, 45, 72, 81, 83, 87, 100, 114, 162

Camassa, R. & Ogrosky, H.R. (2015). On viscous film flows coating the interior of a tube: thin-film and long-wave models. *Journal of Fluid Mechanics*, **772**, 569–599. 38

Castro-Hernández, E., Van Hoeve, W., Lohse, D. & Gordillo, J.M. (2011). Microbubble generation in a co-flow device operated in a new regime. *Lab on a Chip*, **11**, 2023–2029. 37

Cazabat, A. & Stuart, M.C. (1986). Dynamics of wetting: effects of surface roughness. *The Journal of Physical Chemistry*, **90**, 5845–5849. 32

Chatterjee, S., Ghanta, K.C. & Hens, A. (2021). Study of multiphase flow inside straight and spiral microchannel and effect of two phase flow on Dean's vortices. *Chemical Engineering Research and Design*, **165**, 398–408. 73

Chen, Y., Kulenovic, R. & Mertz, R. (2009). Numerical study on the formation of Taylor bubbles in capillary tubes. *International Journal of Thermal Sciences*, **48**, 234–242. 10, 37, 42

Cherukumudi, A., Klaseboer, E., Khan, S.A. & Manica, R. (2015). Prediction of the shape and pressure drop of Taylor bubbles in circular tubes. *Microfluidics and Nanofluidics*, **19**, 1221–1233. 15

Christopher, G.F., Noharuddin, N.N., Taylor, J.A. & Anna, S.L. (2008). Experimental observations of the squeezing-to-dripping transition in T-shaped microfluidic junctions. *Physical Review E—Statistical, Nonlinear, and Soft Matter Physics*, **78**, 036317. 22

Collicott, S.H., Lindsley, W.G. & Frazer, D.G. (2006). Zero-gravity liquid-vapor interfaces in circular cylinders. *Physics of Fluids*, **18**. 65, 66

Colombo, M. & Fairweather, M. (2025). Prediction of bubbly flow and flow regime development in a horizontal air-water pipe flow with a morphology-adaptive multifluid CFD model. *International Journal of Multiphase Flow*, **184**, 105112. 10

Cooray, H., Huppert, H.E. & Neufeld, J.A. (2016). Maximal liquid bridges between horizontal cylinders. *Proceedings of the Royal Society A: Mathematical, Physical and Engineering Sciences*, **472**, 20160233. 132

Cox, B. (1962). On driving a viscous fluid out of a tube. *Journal of Fluid Mechanics*, **14**, 81–96. 3, 10, 11, 98

Cox, R. (1986). The dynamics of the spreading of liquids on a solid surface. Part 1. Viscous flow. *Journal of fluid mechanics*, **168**, 169–194. 25, 28, 29, 30, 52, 67, 71, 126

Cubaud, T., Tatineni, M., Zhong, X. & Ho, C.M. (2005). Bubble dispenser in microfluidic devices. *Physical Review E—Statistical, Nonlinear, and Soft Matter Physics*, **72**, 037302. 6, 23, 33, 35, 38, 41, 42, 65, 77, 108, 109, 112, 120, 124, 136, 153, 154, 155, 156, 157, 159

Damania, B.S. & Bose, A. (1986). Effects of surfactants in the spreading of liquids on solid surfaces. *Journal of colloid and interface science*, **113**, 321–335. 51

Dang, M., Yue, J. & Chen, G. (2015). Numerical simulation of Taylor bubble formation in a microchannel with a converging shape mixing junction. *Chemical Engineering Journal*, **262**, 616–627. 42

Davidson, J. (1960). Bubble formation at an orifice in an inviscid liquid. *Trans. Inst. Chem. Eng.*, **38**, 335–342. 17

De Gennes, P.G., Brochard-Wyart, F. & Quéré, D. (2003). *Capillarity and wetting phenomena: drops, bubbles, pearls, waves*. Springer Science & Business Media. 28, 65

De Menech, M., Garstecki, P., Jousse, F. & Stone, H.A. (2008). Transition from squeezing to dripping in a microfluidic T-shaped junction. *journal of fluid mechanics*, **595**, 141–161. 22, 23

Delaunay, C. (1841). Sur la surface de révolution dont la courbure moyenne est constante. *Journal de mathématiques pures et appliquées*, **6**, 309–315. 111

Derby, B. (2010). Inkjet printing of functional and structural materials: fluid property requirements, feature stability, and resolution. *Annual Review of Materials Research*, **40**, 395–414. 18

Dietrich, N., Loubiere, K., Jimenez, M., Hébrard, G. & Gourdon, C. (2013). A new direct technique for visualizing and measuring gas–liquid mass transfer around bubbles moving in a straight millimetric square channel. *Chemical Engineering Science*, **100**, 172–182. 73

Dietze, G.F. (2024). Liquid plugs in narrow tubes: application to airway occlusion. *Journal of Fluid Mechanics*, **998**, A50. 110

Duclaux, V., Clanet, C. & Quéré, D. (2006). The effects of gravity on the capillary instability in tubes. *Journal of Fluid Mechanics*, **556**, 217–226. 19

Duffy, B. & Wilson, S. (1997). A third-order differential equation arising in thin-film flows and relevant to Tanner's law. *Applied Mathematics Letters*, **10**, 63–68. 31

Dussan, E. (1979). On the spreading of liquids on solid surfaces: static and dynamic contact lines. *Annual Review of Fluid Mechanics*, **11**, 371–400. 26

Eggers, J. (1997). Nonlinear dynamics and breakup of free-surface flows. *Reviews of modern physics*, **69**, 865. 18, 19, 70

Eggers, J. (2000). Singularities in droplet pinching with vanishing viscosity. *SIAM Journal on Applied Mathematics*, **60**, 1997–2008. 19

Eggers, J. (2004). Hydrodynamic theory of forced dewetting. *Physical review letters*, **93**, 094502. 45

Eggers, J. (2005a). Contact line motion for partially wetting fluids. *Physical review E*, **72**, 061605. 30

Eggers, J. (2005b). Existence of receding and advancing contact lines. *Physics of Fluids*, **17**. 45

Eggers, J. & Dupont, T.F. (1994). Drop formation in a one-dimensional approximation of the Navier–Stokes equation. *Journal of fluid mechanics*, **262**, 205–221. 18, 70, 71

Eggersdorfer, M.L., Seybold, H., Ofner, A., Weitz, D.A. & Studart, A.R. (2018). Wetting controls of droplet formation in step emulsification. *Proceedings of the National Academy of Sciences*, **115**, 9479–9484. 18

Emslie, A.G., Bonner, F.T. & Peck, L.G. (1958). Flow of a viscous liquid on a rotating disk. *Journal of Applied Physics*, **29**, 858–862. 30

Everett, D. & Haynes, J. (1972). Model studies of capillary condensation. I. Cylindrical pore model with zero contact angle. *Journal of Colloid and Interface Science*, **38**, 125–137. 19, 38, 66, 110, 111, 130, 131

Fairbrother, F. & Stubbs, A.E. (1935). Studies in electro-endosmosis. Part VI. The "bubble-tube" method of measurement. *Journal of the Chemical Society (Resumed)*, 527–529. 3, 4, 10, 11

Finn, R. (1986). Equilibrium capillary surfaces. *Grundlehren der mathematischen Wissenschaften*. 132

Fraysse, N. & Homsy, G.M. (1994). An experimental study of rivulet instabilities in centrifugal spin coating of viscous newtonian and non-newtonian fluids. *Physics of fluids*, **6**, 1491–1504. 25

Frenkel, A., Babchin, A., Levich, B., Shlang, T. & Sivashinsky, G. (1987). Annular flows can keep unstable films from breakup: nonlinear saturation of capillary instability. *Journal of colloid and interface science*, **115**, 225–233. 38

Fu, T. & Ma, Y. (2015). Bubble formation and breakup dynamics in microfluidic devices: A review. *Chemical Engineering Science*, **135**, 343–372. 33, 36

Fu, T., Ma, Y., Funfschilling, D., Zhu, C. & Li, H.Z. (2010). Squeezing-to-dripping transition for bubble formation in a microfluidic T-junction. *Chemical engineering science*, **65**, 3739–3748. 22

Gao, P., Li, L., Feng, J.J., Ding, H. & Lu, X.Y. (2016). Film deposition and transition on a partially wetting plate in dip coating. *Journal of Fluid Mechanics*, **791**, 358–383. 45

Garstecki, P., Gitlin, I., DiLuzio, W., Whitesides, G.M., Kumacheva, E. & Stone, H.A. (2004). Formation of monodisperse bubbles in a microfluidic flow-focusing device. *Applied Physics Letters*, **85**, 2649–2651. 23, 77

Garstecki, P., Stone, H.A. & Whitesides, G.M. (2005). Mechanism for flow-rate controlled breakup in confined geometries: A route to monodisperse emulsions. *Physical review letters*, **94**, 164501. 5, 6, 22, 23

Garstecki, P., Fuerstman, M.J., Stone, H.A. & Whitesides, G.M. (2006). Formation of droplets and bubbles in a microfluidic T-junction—scaling and mechanism of break-up. *Lab on a Chip*, **6**, 437–446. 6, 22, 23, 37, 38, 39, 41, 42, 47, 65, 66, 77, 108, 109, 112, 120, 123, 136, 154, 155, 159

Gauglitz, P. & Radke, C. (1988). An extended evolution equation for liquid film breakup in cylindrical capillaries. *Chemical Engineering Science*, **43**, 1457–1465. 19, 20, 24, 38, 45, 111

Gillette, R. & Dyson, D. (1971). Stability of fluid interfaces of revolution between equal solid circular plates. *The Chemical Engineering Journal*, **2**, 44–54. 111

Gordillo, J., Pérez-Saborid, M. & Gañán-Calvo, A. (2001). Linear stability of co-flowing liquid–gas jets. *Journal of Fluid Mechanics*, **448**, 23–51. 20

Goren, S.L. (1962). The instability of an annular thread of fluid. *Journal of Fluid Mechanics*, **12**, 309–319. 38

Grotberg, J.B. (1994). Pulmonary flow and transport phenomena. *Annual review of fluid mechanics*, **26**, 529–571. 110

Guerrero, J., Chang, Y.W., Fragkopoulos, A.A. & Fernandez-Nieves, A. (2020). Capillary-based microfluidics—coflow, flow-focusing, electro-coflow, drops, jets, and instabilities. *Small*, **16**, 1904344. 20

Haase, S. (2017). Characterisation of gas-liquid two-phase flow in minichannels with co-flowing fluid injection inside the channel, part II: gas bubble and liquid slug lengths, film thickness, and void fraction within Taylor flow. *International Journal of Multiphase Flow*, **88**, 251–269. 37

Halpern, D. & Grotberg, J.B. (1992). Fluid-elastic instabilities of liquid-lined flexible tubes. *Journal of Fluid Mechanics*, **244**, 615–632. 25

Hammond, P. (1983). Nonlinear adjustment of a thin annular film of viscous fluid surrounding a thread of another within a circular cylindrical pipe. *Journal of fluid Mechanics*, **137**, 363–384. 13, 19, 20, 38, 45, 110

Heil, M. & White, J.P. (2002). Airway closure: surface-tension-driven non-axisymmetric instabilities of liquid-lined elastic rings. *Journal of Fluid Mechanics*, **462**, 79–109. 110

Hocking, L. (1982). The motion of a drop on a rigid surface. In *JPL Proc. of the 2d Intern. Colloq. on Drops and Bubbles*. 37, 40, 55

Hocking, L. (1983). The spreading of a thin drop by gravity and capillarity. *The Quarterly Journal of Mechanics and Applied Mathematics*, **36**, 55–69. 32, 45, 52

Hocking, L. & Rivers, A. (1982). The spreading of a drop by capillary action. *Journal of Fluid Mechanics*, **121**, 425–442. 25, 52

Howell, P., Robinson, J. & Stone, H.A. (2013). Gravity-driven thin-film flow on a flexible substrate. *Journal of Fluid Mechanics*, **732**, 190–213. 25

Huang, J. & Yao, Z. (2022). Influencing factors and size prediction of bubbles formed by flow focusing in a cross-channel. *Chemical Engineering Science*, **248**, 117228. 41

Huh, C. & Scriven, L.E. (1971). Hydrodynamic model of steady movement of a solid/liquid/fluid contact line. *Journal of colloid and interface science*, **35**, 85–101. 26

Humphry, K.J., Ajdari, A., Fernández-Nieves, A., Stone, H.A. & Weitz, D.A. (2009). Suppression of instabilities in multiphase flow by geometric confinement. *Physical Review E—Statistical, Nonlinear, and Soft Matter Physics*, **79**, 056310. 20

Jensen, M.J., Stone, H.A. & Bruus, H. (2006). A numerical study of two-phase stokes flow in an axisymmetric flow-focusing device. *Physics of Fluids*, **18**, 077103. 23, 37, 65, 109, 112

Jensen, O. (1997). The thin liquid lining of a weakly curved cylindrical tube. *Journal of Fluid Mechanics*, **331**, 373–403. 131

Jensen, O. & Naire, S. (2006). The spreading and stability of a surfactanT-laden drop on a prewetted substrate. *Journal of Fluid Mechanics*, **554**, 5–24. 32

Johnson, M., Kamm, R.D., Ho, L.W., Shapiro, A. & Pedley, T. (1991). The nonlinear growth of surface-tension-driven instabilities of a thin annular film. *Journal of Fluid Mechanics*, **233**, 141–156. 71

Kerchman, V. (1995). Strongly nonlinear interfacial dynamics in core–annular flows. *Journal of Fluid Mechanics*, **290**, 131–166. 38

Khan, A.H., Ganguli, A., Edirisinghe, M. & Dalvi, S.V. (2025). Controlling microbubble formation in microfluidic devices: Advancements in experimental, theoretical, and numerical strategies. *Applied Physics Reviews*, **12**. 36

Kheshgi, H.S. (1989). Profile equations for film flows at moderate reynolds numbers. *AIChE Journal*, **35**, 1719–1727. 71

Kim, C.S., Rodriguez, C.R., Eldridge, M.A. & Sackner, M.A. (1986). Criteria for mucus transport in the airways by two-phase gas-liquid flow mechanism. *Journal of Applied Physiology*, **60**, 901–907. 36

King, J. & Bowen, M. (2001). Moving boundary problems and non-uniqueness for the thin film equation. *European Journal of Applied Mathematics*, **12**, 321–356. 25, 31, 32, 45, 51, 52, 55, 67

Kiradjiev, K., Breward, C. & Griffiths, I. (2019). Surface-tension-and injection-driven spreading of a thin viscous film. *Journal of Fluid Mechanics*, **861**, 765–795. 27, 31, 32, 40, 45, 51, 52, 55, 58, 60, 67

Klaseboer, E., Gupta, R. & Manica, R. (2014). An extended bretherton model for long Taylor bubbles at moderate capillary numbers. *Physics of Fluids*, **26**. 15

Lacey, A. (1982). The motion with slip of a thin viscous droplet over a solid surface. *Studies in applied mathematics*, **67**, 217–230. 25

Landau, L. & Levich, B. (1988). Dragging of a liquid by a moving plate. In *Dynamics of curved fronts*, 141–153, Elsevier. 13, 45, 83

Lee, H., Kim, H., Han, H., Lee, M., Lee, S., Yoo, H., Chang, J.H. & Kim, H. (2017). Microbubbles used for contrast enhanced ultrasound and theragnosis: a review of principles to applications. *Biomedical Engineering Letters*, **7**, 59–69. 36

Levinson, P., Cazabat, A., Cohen Stuart, M., Heslot, F. & Nicolet, S. (1988). The spreading of macroscopic droplets. *Revue de physique appliquée*, **23**, 1009–1016. 32

Lu, W., Li, E.Q. & Gao, P. (2023). Generation of microbubbles via a tapered capillary. *Physics of Fluids*, **35**. 17, 38, 45, 73, 97

Lu, Y., Fu, T., Zhu, C., Ma, Y. & Li, H.Z. (2016). Experimental investigation on the breakup dynamics for bubble formation in viscous liquids in a flow-focusing device. *Chemical Engineering Science*, **152**, 516–527. 41

Lv, C. & Hardt, S. (2021). Wetting of a liquid annulus in a capillary tube. *Soft Matter*, **17**, 1756–1772. 65, 66, 111, 130

Ma, L., Zhao, X., Hou, J., Huang, L., Yao, Y., Ding, Z., Wei, J. & Hao, N. (2024). Droplet microfluidic devices: working principles, fabrication methods, and scale-up applications. *Small Methods*, **8**, 2301406. 37, 41

Maîtrejean, G., Cousin, M., Truong, F., Verdoot, V., Hugenell, F. & Roux, D.C. (2024). Comprehensive experimental dataset on large-amplitude Rayleigh-Plateau instability in continuous inkjet printing regime. *Data in Brief*, **52**, 109941. 18

Marmur, A. & Rubin, E. (1976). A theoretical model for bubble formation at an orifice submerged in an inviscid liquid. *Chemical Engineering Science*, **31**, 453–463. 17

Martín-Banderas, L., Flores-Mosquera, M., Riesco-Chueca, P., Rodríguez-Gil, A., Cebolla, Á., Chávez, S. & Gañán-Calvo, A.M. (2005). Flow focusing: a versatile technology to produce size-controlled and specific-morphology microparticles. *Small*, **1**, 688–692. 17

Martinez, M.J. & Udell, K.S. (1989). Boundary Integral Analysis of the Creeping Flow of Long Bubbles in Capillaries. *Journal of Applied Mechanics*, **56**, 211–217. 73

Mason, G. (1970). An experimental determination of the stable length of cylindrical liquid bubbles. *Journal of Colloid and Interface Science*, **32**, 172–176. 111

McGraw, J.D., Salez, T., Bäumchen, O., Raphaël, E. & Dalnoki-Veress, K. (2012). Self-similarity and energy dissipation in stepped polymer films. *Physical Review Letters*, **109**, 128303. 85

McHale, G., Newton, M., Rowan, S. & Banerjee, M. (1995). The spreading of small viscous stripes of oil. *Journal of Physics D: Applied Physics*, **28**, 1925. 32

Mei, M., Le Men, C., Loubière, K., Hébrard, G. & Dietrich, N. (2022). Taylor bubble formation and flowing in a straight millimetric channel with a cross-junction inlet geometry. Part I: Bubble dynamics. *Chemical Engineering Science*, **255**, 117609. 42

Melo, F., Joanny, J. & Fauve, S. (1989). Fingering instability of spinning drops. *Physical review letters*, **63**, 1958. 30

Migler, K.B. (2001). String formation in sheared polymer blends: coalescence, breakup, and finite size effects. *Physical review letters*, **86**, 1023. 110

Myers, T.G. (1998). Thin films with high surface tension. *SIAM review*, **40**, 441–462. 25

Ogarev, V., Timonina, T., Arslanov, V. & Trapeznikov, A. (1974). Spreading of polydimethylsiloxane drops on solid horizontal surfaces. *The Journal of Adhesion*, **6**, 337–355. 32

Oguz, H.N. & Prosperetti, A. (1993). Dynamics of bubble growth and detachment from a needle. *Journal of Fluid Mechanics*, **257**, 111–145. 17

Oron, A., Davis, S.H. & Bankoff, S.G. (1997). Long-scale evolution of thin liquid films. *Reviews of modern physics*, **69**, 931. 13

Pahlavan, A.A., Stone, H.A., McKinley, G.H. & Juanes, R. (2019). Restoring universality to the pinch-off of a bubble. *Proceedings of the National Academy of Sciences*, **116**, 13780–13784. 38, 122, 123

Papageorgiou, D.T. (1995). Analytical description of the breakup of liquid jets. *Journal of Fluid Mechanics*, **301**, 109–132. 18

Peregrine, D.H., Shoker, G. & Symon, A. (1990). The bifurcation of liquid bridges. *Journal of Fluid Mechanics*, **212**, 25–39. 71

Plateau, J.A.F. (1873). *Statique expérimentale et théorique des liquides soumis aux seules forces moléculaires*, vol. 2. Gauthier-Villars. 18, 20, 110

Ponalagusamy, R. & Tamil Selvi, R. (2015). Influence of magnetic field and heat transfer on two-phase fluid model for oscillatory blood flow in an arterial stenosis. *Meccanica*, **50**, 927–943. 36

Raisinghani, A. & DeMaria, A.N. (2002). Physical principles of microbubble ultrasound contrast agents. *The American journal of cardiology*, **90**, 3–7. 36

Ratulowski, J. & Chang, H.C. (1989). Transport of gas bubbles in capillaries. *Physics of Fluids A: Fluid Dynamics*, **1**, 1642–1655. 4, 16, 17, 34, 72, 79, 80, 83, 87, 92, 97, 98, 114, 118, 162

Rayleigh, L. (1878). On the instability of jets. *Proceedings of the London mathematical society*, **1**, 4–13. 18, 20, 110

Rayleigh, L. (1879). On the capillary phenomena of jets. *Proceedings of the royal society of London*, 71–97. 18

Redo, M.A., Jeong, J., Giannetti, N., Enoki, K., Yamaguchi, S., Saito, K. & Kim, H. (2019). Characterization of two-phase flow distribution in microchannel heat exchanger header for air-conditioning system. *Experimental Thermal and Fluid Science*, **106**, 183–193. 36

Reinelt, D. & Saffman, P. (1985). The penetration of a finger into a viscous fluid in a channel and tube. *SIAM Journal on Scientific and Statistical Computing*, **6**, 542–561. 3, 4, 14, 16, 17, 43, 44, 72, 73, 82, 83, 114, 115

Russo, M.J. & Steen, P.H. (1986). Instability of rotund capillary bridges to general disturbances: experiment and theory. *Journal of colloid and interface science*, **113**, 154–163. 111

Rykner, M., Saikali, E., Bruneton, A., Mathieu, B. & Nikolayev, V.S. (2024). Plateau–Rayleigh instability in a capillary: assessing the importance of inertia. *Journal of Fluid Mechanics*, **1001**, A15. 45

Salman, W., Gavriilidis, A. & Angeli, P. (2006). On the formation of Taylor bubbles in small tubes. *Chemical Engineering Science*, **61**, 6653–6666. 6, 10, 37, 41, 42, 66, 96

San Miguel, M., Grant, M. & Gunton, J.D. (1985). Phase separation in two-dimensional binary fluids. *Physical Review A*, **31**, 1001. 110

Sanz, A. & Martinez, I. (1983). Minimum volume for a liquid bridge between equal disks. *Journal of Colloid and Interface Science*, **93**, 235–240. 111

Sattari-Najafabadi, M., Esfahany, M.N., Wu, Z. & Sunden, B. (2018). Mass transfer between phases in microchannels: A review. *Chemical Engineering and Processing-Process Intensification*, **127**, 213–237. 10

Savva, N. & Kalliadasis, S. (2009). Two-dimensional droplet spreading over topographical substrates. *Physics of Fluids*, **21**. 45, 52

Savva, N. & Kalliadasis, S. (2011). Dynamics of moving contact lines: A comparison between slip and precursor film models. *Europhysics Letters*, **94**, 64004. 52

Savva, N. & Kalliadasis, S. (2013). Droplet motion on inclined heterogeneous substrates. *Journal of Fluid Mechanics*, **725**, 462–491. 52

Schwartz, L., Princen, H. & Kiss, A. (1986). On the motion of bubbles in capillary tubes. *Journal of Fluid Mechanics*, **172**, 259–275. 114

Shen, Y., Dang, C., Sun, X., Cao, L. & Zhang, Y. (2024). Numerical investigation on Taylor bubble mass transfer in microchannel based on CO2 gas with the consideration of gas compressibility. *Chemical Engineering Science*, **298**, 120410. 10

Sibley, D.N., Nold, A. & Kalliadasis, S. (2015). The asymptotics of the moving contact line: cracking an old nut. *Journal of Fluid Mechanics*, **764**, 445–462. 30

Sirsi, S. & Borden, M. (2009). Microbubble compositions, properties and biomedical applications. *Bubble Science, Engineering & Technology*, **1**, 3–17. 1

Slobozhanin, L.A., Gomez, M. & Perales Perales, J.M. (1995). Stability of liquid bridges between unequal disks under zero-gravity conditions. *Microgravity Science and Technology*, **8**, 23–34. 111

Slobozhanin, L.A., Alexander, J.I.D. & Fedoseyev, A.I. (1999). Shape and stability of doubly connected axisymmetric free surfaces in a cylindrical container. *Physics of Fluids*, **11**, 3668–3677. 65, 66

Snoeijer, J.H. (2006). Free-surface flows with large slopes: Beyond lubrication theory. *Physics of Fluids*, **18**. 16, 71, 97, 158, 164

Snoeijer, J.H., Andreotti, B., Delon, G. & Fermigier, M. (2007). Relaxation of a dewetting contact line. Part 1. A full-scale hydrodynamic calculation. *Journal of Fluid Mechanics*, **579**, 63–83. 45

Sun, X., Dang, C., Jia, H., Shen, Y. & Liu, Y. (2025). Dynamics of Taylor bubble formation in a small-scale flow focusing microchannel with an acute symmetrical inlet geometry. *Chemical Engineering Science*, **305**, 121141. 5, 41

Suwankamnerd, P. & Wongwises, S. (2015). An experimental study of two-phase air–water flow and heat transfer characteristics of segmented flow in a microchannel. *Experimental Thermal and Fluid Science*, **62**, 29–39. 36

Taha, T. & Cui, Z. (2006). CFD modelling of slug flow inside square capillaries. *Chemical Engineering Science*, **61**, 665–675. 73

Tanner, L. (1979). The spreading of silicone oil drops on horizontal surfaces. *Journal of Physics D: Applied Physics*, **12**, 1473. 32, 55

Taylor, G. (1961). Deposition of a viscous fluid on the wall of a tube. *Journal of fluid mechanics*, **10**, 161–165. 3, 4, 10, 11, 14, 15, 16, 24, 42, 97, 114, 115

Thulasidas, T., Abraham, M.A. & Cerro, R.L. (1997). Flow patterns in liquid slugs during bubble-train flow inside capillaries. *Chemical engineering science*, **52**, 2947–2962. 73

Tomotika, S. (1935). On the instability of a cylindrical thread of a viscous liquid surrounded by another viscous fluid. *Proceedings of the Royal Society of London. Series A-Mathematical and Physical Sciences*, **150**, 322–337. 132

Triplett, K.A., Ghiaasiaan, S., Abdel-Khalik, S. & Sadowski, D. (1999). Gas–liquid two-phase flow in microchannels part i: two-phase flow patterns. *International Journal of Multiphase Flow*, **25**, 377–394. 9, 10, 37, 42, 108

Tsutsui, J.M., Xie, F. & Porter, R.T. (2004). The use of microbubbles to target drug delivery. *Cardiovascular Ultrasound*, **2**, 23. 36

Tuck, E. & Schwartz, L. (1990). A numerical and asymptotic study of some third-order ordinary differential equations relevant to draining and coating flows. *SIAM review*, **32**, 453–469. 30

Utada, A.S., Fernandez-Nieves, A., Stone, H.A. & Weitz, D.A. (2007). Dripping to jetting transitions in coflowing liquid streams. *Physical review letters*, **99**, 094502. 20, 37

Van Hoeve, W., Dollet, B., Gordillo, J.M., Versluis, M., Van Wijngaarden, L. & Lohse, D. (2011). Bubble size prediction in co-flowing streams. *Europhysics Letters*, **94**, 64001. 37

van Steijn, V., Kreutzer, M.T. & Kleijn, C.R. (2007). μ-PIV study of the formation of segmented flow in microfluidic T-junctions. *Chemical Engineering Science*, **62**, 7505–7514. 6

van Steijn, V., Kleijn, C.R. & Kreutzer, M.T. (2009). Flows around confined bubbles and their importance in triggering pinch-off. *Physical review letters*, **103**, 214501. 5, 6

Vellingiri, R., Savva, N. & Kalliadasis, S. (2011). Droplet spreading on chemically heterogeneous substrates. *Physical Review E*, **84**, 036305. 52

Vladisavljević, G.T., Khalid, N., Neves, M.A., Kuroiwa, T., Nakajima, M., Uemura, K., Ichikawa, S. & Kobayashi, I. (2013). Industrial lab-on-a-chip: Design, applications and scale-up for drug discovery and delivery. *Advanced drug delivery reviews*, **65**, 1626–1663. 1, 36

Voinov, O. (1976). Hydrodynamics of wetting. *Fluid dynamics*, **11**, 714–721. 25, 28, 29, 30, 52, 67, 71, 126

Wang, K., Xie, L., Lu, Y. & Luo, G. (2013). Generating microbubbles in a co-flowing microfluidic device. *Chemical Engineering Science*, **100**, 486–495. 37

Wang, X.L., Qin, J. & Gao, P. (2025). Axisymmetric evolution of thin films in spin coating. *Journal of Fluid Mechanics*, **1007**, A56. 30

Wilson, S.D. (1982). The drag-out problem in film coating theory. *Journal of Engineering Mathematics*, **16**, 209–221. 25

Wong, H., Radke, C. & Morris, S. (1995). The motion of long bubbles in polygonal capillaries. Part 1. Thin films. *Journal of Fluid Mechanics*, **292**, 71–94. 36

Wörner, M. (2012). Numerical modeling of multiphase flows in microfluidics and micro process engineering: a review of methods and applications. *Microfluidics and nanofluidics*, **12**, 841–886. 22

Xiong, R., Bai, M. & Chung, J.N. (2007). Formation of bubbles in a simple co-flowing micro-channel. *Journal of Micromechanics and Microengineering*, **17**, 1002. 6, 23, 37, 42, 65, 77, 109, 112, 120, 136, 154, 155, 159

Xu, J.H., Li, S., Tan, J. & Luo, G. (2008). Correlations of droplet formation in T-junction microfluidic devices: from squeezing to dripping. *Microfluidics and Nanofluidics*, **5**, 711–717. 22

Yue, J., Luo, L., Gonthier, Y., Chen, G. & Yuan, Q. (2008). An experimental investigation of gas–liquid two-phase flow in single microchannel contactors. *Chemical Engineering Science*, **63**, 4189–4202. 108

Zaloha, P., Kristal, J., Jiricny, V., Völkel, N., Xuereb, C. & Aubin, J. (2012). Characteristics of liquid slugs in gas–liquid Taylor flow in microchannels. *Chemical engineering science*, **68**, 640–649. 73

Zhang, J.M., Li, E.Q. & Thoroddsen, S.T. (2014). A co-flow-focusing monodisperse microbubble generator. *Journal of Micromechanics and Microengineering*, **24**, 035008. 37

Zhang, T., Zou, X., Xu, L., Pan, D. & Huang, W. (2021). Numerical investigation of fluid property effects on formation dynamics of millimeter-scale compound droplets in a co-flowing device. *Chemical Engineering Science*, **229**, 116156. 22

Zhang, X., Padgett, R.S. & Basaran, O.A. (1996). Nonlinear deformation and breakup of stretching liquid bridges. *Journal of Fluid Mechanics*, **329**, 207–245. 71

Zhang, Y., Zhu, C., Chu, C., Fu, T. & Ma, Y. (2022). Mass transfer and capture of carbon dioxide using amino acids sodium aqueous solution in microchannel. *Chemical Engineering and Processing-Process Intensification*, **173**, 108831. 5

Zhao, B., Alizadeh Pahlavan, A., Cueto-Felgueroso, L. & Juanes, R. (2018). Forced wetting transition and bubble pinch-off in a capillary tube. *Physical review letters*, **120**, 084501. 23, 38, 39, 41, 42, 45, 46, 111, 112, 116, 122

Zúñiga, R. & Aguilera, J. (2008). Aerated food gels: fabrication and potential applications. *Trends in food science & technology*, **19**, 176–187. 36